Ultrasonic characterization of soft tissue-to-bone interphase : modeling, numerical study and experimental validation

Ali Aghaei

UNIVERSITÉ PARIS–EST CRÉTEIL

École doctorale SIE: Sciences, Ingénierie et Environnement

Laboratoire Modélisation et Simulation Multi Échelle, UMR 8208 CNRS

Thesis submitted for the grade of Doctor of Philosophy

Major: Biomechanics

Ultrasonic characterization of soft tissue-to-bone interphase: modeling, numerical study and experimental validation

by

Ali AGHAEI

The members of the thesis committee:

Mme. Cécile Baron Chargée de Recherche CNRS (Aix-Marseille Université)	Phd referee
M. Jean-François Ganghoffer Professeur des Universités (Université de Lorraine)	Phd referee
M. Ridha Hambli Professeur des Universités (Université d'Orléans)	Phd president
M. Salah Naili Professeur des Universités (Université Paris-Est Créteil)	PhD advisor
M. Nicolas Bochud Maitre de conférences (Université Paris-Est Créteil)	PhD co-advisor
M. Giuseppe Rosi Maitre de conférences (Université Paris-Est Créteil)	PhD co-advisor

How Sweet is mortal Sovranty!"–think some;
Others–"How blest the Paradise to come!"
Ah, take the Cash in hand and waive the Rest;
Oh, the brave Music of a distant Drum!

Edward FitzGerald,
The Rubáiyát of Omar Khayyám

Acknowledgments

First, I would like to express my sincere gratitude to my PhD supervisor, Prof. Salah Naili, for giving me the opportunity to undertake this PhD thesis. I really appreciated his continuous support, precious advice and encouragement. Once I started my master, his valuable and constructive suggestions guided me over these past few years. He provided me with the resources to work in the best possible conditions and also gave me the opportunity to teach, which made me more confident at both professional and personal levels.

Apart from my supervisor, I won't forget to express my gratitude to my PhD co-supervisors, Nicolas Bochud and Giuseppe Rosi, whose consistent support, patient guidance, enthusiastic encouragement have been invaluable throughout these years. They have played a major role in polishing my research work and writing skills by sacrificing their time so generously.

Besides my supervisors, I would like to thank the other members of the thesis committee, who have done me the honor of evaluating my work: Mme. Cécile Baron and M. Jean-François Ganghoffer as referees, and M. Ridha Hambli as examiner.

I wish to thank all my colleagues and the members of the MSME laboratory for creating a positive environment to work in and for always being nice with me. Some of them became, above all, friends during this long journey that made my study and life in the France a wonderful time. Thanks to Fakhraddin, who provided stimulating discussions as well as happy distractions to rest my mind outside of my research. Thanks to Max for the fruitful discussions regarding the processing of the ultrasound signals. Thanks to Sophie for organizing many memorable evenings in and out of the laboratory. Thanks to the Persian language team, Sophie and Manon, for their enthusiasm and motivation in learning Farsi and also to the badminton team, Anne-Sophie, Sophie, Yoann, Nicolas and Giuseppe, for the intensive evening sessions.

I would also like to thank Hung-Son and Yasmin for their valuable help and support, as well as Isabelle for her sympathy and joyfulness. I thank all those who I didn't get the opportunity to do a research work with, but still work to organize the teaching courses, Alexandre, Vittorio, Gilles and also Thibault, Guillaume, Vu-Hieu, Matthieu, with whom I had the occasion to talk with.

My sincere thanks also goes to Dr. Davide Ruffoni and Quentin Grossman at the Mechanics of Biological and Bioinspired Materials laboratory of the University of Liège for their wonderful collaboration during these years. I truly appreciated their knowledge on additive manufacturing and their help to fabricate multi-material samples.

Finally, my deep and sincere gratitude to my family for their continuous love, help and support. I am grateful to my parents for encouraging me to explore new directions in life and seek my own destiny and also for unfailing emotional support from distance in the past few years. Not forgetting my sister for always being supportive as a friend. I am grateful to my aunt, her husband and my cousin, who welcame me warmly and always supported and helped me. This journey would not have been possible if not for them. Thanks to my grandmother and my little aunt who offered their encouragement through video calls. This journey would not have been possible without the support of my family and my friends, and I dedicate this milestone to them.

Contents

Introduction

Context and motivation

The musculoskeletal system is not only composed of soft and hard tissues, such as muscles, ligaments, tendons, cartilages, and bones, but also of specialized functional interphases[1] joining those tissues. Among these, the interphase connecting soft tissues –tendon or ligament– to bone, called *enthesis*, fulfills the challenging task of integrating two highly dissimilar tissues over a submillimeter-wide region. From an engineering viewpoint, when two materials having such a dissimilar mechanical nature meet, they typically display highly non-uniform deformations upon loading, eventually leading to stress concentration at the interphase, which in turn increases the failure probability. Surprisingly, the healthy enthesis shows a remarkable ability in minimizing stress concentration and associated failure modes, thereby allowing it to withstand forces greater than the body weight during millions of loading cycles.

Despite its outstanding endurance, the enthesis of elderly people and sporty individuals is prone to failure due to pathology, disuse, or repeated overloading, with relevant examples being the rupture of the rotator cuff tendons, the anterior cruciate ligaments, or the Achilles tendons [1]. Such musculoskeletal injuries involving soft tissue rupture typically require surgical reattachment back to bone. Unfortunately, current reattachment procedures still exhibit high failure rates that may vary from 20% to 97% depending on the extent of the injury and the age of the patients [2]. This is mainly because the enthesis, in contrast to soft tissues and bone, rarely regenerates during healing and remodeling phases, and therefore does not recover its pristine anchoring properties [3]. This clinical burden is, in part, due to the lack of understanding of the structure-function relationship of the healthy attachment, as well as of the damage mechanisms that may occur across this interphase. A prerequisite to improve clinical outcomes therefore relies on a detailed knowledge of the mechanics of this interfacial region [4]. Nonetheless, although the mechanical behavior of soft tissues and bone has been thoroughly explored, much less is known about the mechanics of the enthesis, mainly because of its complex and heterogeneous nature confined over a very small region.

From an anatomic viewpoint, entheses are typically categorized as fibrous or fibro-

[1] In contrast to an interface (that has null thickness), the term "interphase" used over the course of this manuscript designates a transition region of finite dimension between two materials.

cartilaginous [5]. Fibrous (or indirect) insertions are usually found at the shafts of long bones, where the collagen fibers of soft tissues extended straight into the bone, such as the insertion of the deltoid tendon into the humerus or the tibial insertion of the medial collateral ligament. Fibrocartilaginous (or direct) insertions are more common and found at joint surfaces, such as the bony attachments of the rotator cuff tendon, the anterior cruciate ligament and the Achilles tendons. At the tissue scale, fibrocartilaginous entheses generally consist of four contiguous regions with different compositions, functions, and biomechanical properties (see Fig. 1): the tendon or ligament, a non-mineralized fibrocartilaginous region, a mineralized fibrocartilaginous region, and bone.

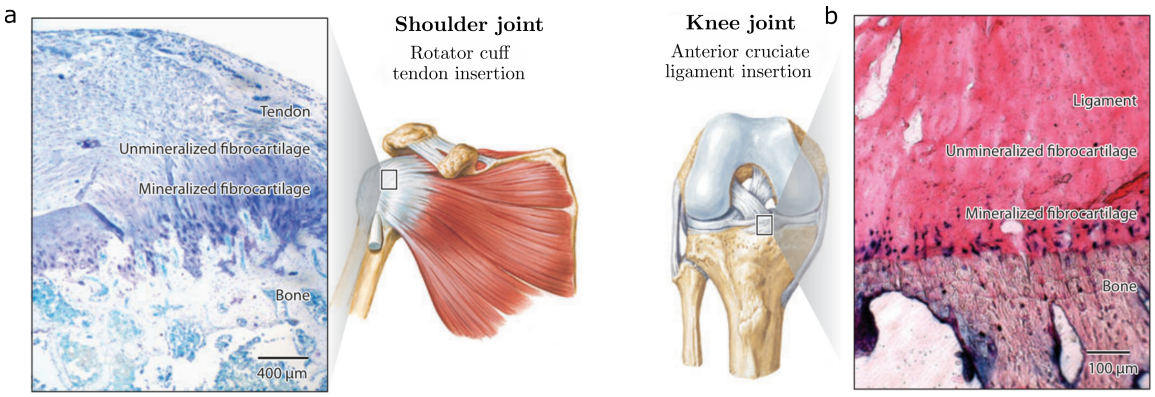

Figure 1 – Illustrations of the four regions constituting fibrocartilaginous entheses for (a) the rotator cuff tendon and (b) the anterior cruciate ligament: tendon or ligament, unmineralized fibrocartilage, mineralized fibrocartilage, and bone (images modified with permission from the Annual Review of Biomedical Engineering, Volume 15 © 2013 by Annual Reviews [6]).

Experimental studies based on different imaging capabilities have been conducted at different length scales to evidence the space-dependent features of these transition regions. For instance, their composition can be analyzed histologically through specific staining procedures of the different collagen types [7]. At the microscale, classical confocal microscopy or polarized light microscopy can be applied to observe the organization, orientation, and morphology of the collagen fibers [8]. Moreover, there is also a variety of techniques for determining the degree of tissue mineralization at the nanoscale, such as the Fourier-transform infrared spectroscopy, the Raman spectroscopy, or the transmission electron microscopy [9–11]. Thereby, it has been shown that tendon and ligament consist of well-aligned type I collagen fibers with small amount of non-collagenous proteins and dispersed fibroblasts. In contrast, the fibrocartilaginous region is mainly characterized by intermingled type II collagen fibers, whose diameter is small compared to that of the soft tissue fibers, and areas of chondrocytes with cartilaginous matrix. This region gets progressively reinforced by mineral crystals before reaching bone, which mostly contains type I collagen. Overall, these investigations all have highlighted the presence of gradual changes of the microstructural features (*e.g.*, mineral and protein gradients, collagen fibers organization, collagen types) across the interphase. Besides, the interdigitation at the interphase between tendon and bone, which is a mesoscopic feature described as a wavelike structure, was shown to allow a gain in toughness, as well as a better distribution of the mechanical stresses across the interphase [12]. Altogether, these mechanisms are

hypothesized to contribute to the mechanical effectiveness of the enthesis, but the direct link between the elementary ingredients at lower length scales (*e.g.*, collagen, mineral, proteins), their spatial arrangement, and the mechanical performance of the enthesis at the tissue scale is still elusive.

From a mechanical modeling viewpoint, two main families of models have been proposed so far. The first family focused on elementary anchoring mechanisms at the microscopic scale, whereas the second family was more related to orthopedic applications at the organ scale. The fundamental idea of the first family consisted in modeling a collagen fibers as a composite made of randomly distributed units of collagen and minerals. By applying stochastic finite-element simulations, the mechanical properties of partially mineralized collagen fibers could be recovered, which subsequently allowed deriving tissue scale properties by taking the orientation of collagen fibers into account [13]. In a posterior study by the same group, this approach was refined by considering different sequences of intra- and extra-fibrillar mineralization pathways at the sub-microstructural level [14]. All these models predicted a sudden stiffening of the tissue scale properties at a position called the percolation threshold, which is believed to occur after minerals have accumulated throughout the entire collagen fiber. The latter study also evidenced the existence of a region that is more compliant than both the tendon and the bone, thus reducing the stress concentration across the interphase. This compliant region was interpreted as an energy absorbing component, which allows the presence of localized deformations and thereby increases the resilience of the interphase [15, 16]. At the organ scale, studies rather focused on understanding damage and failure mechanisms [17–20] or reattachment strategies [21, 22] at the soft tissue-to-bone complex. In these models, however, the interphase itself was generally greatly simplified or even replaced by a sharp interface. Therefore, there is still a need in developing computational multiscale models that bridge the gap between these two families of models [23]. Such models could for instance be valuable for triggering the development of novel bioinspired reattachment strategies [24], which would reflect to some extent the microscopic features of healthy entheses.

Therefore, improving our understanding of the mechanisms responsible for the mechanical effectiveness of these interfacial regions remains essential not only for clinical purposes targeting relevant orthopedic issues but also for the development of biomimetic strategies in engineering that aim at joining dissimilar materials together. In this way, there is an unmet need in understanding the mechanics of this interfacial region by clarifying the impact of the structural and compositional features at lower length scales on the mechanical properties of this complex interphase at the tissue scale. The retrieved effective properties could for instance be employed for developing computational models at the organ scale targeting relevant orthopedic questions and for fabricating bioinspired functionally graded soft-to-hard composites. Meanwhile, the development of characterization methods for assessing the mechanics of such manufactured materials could represent an appealing outcome. In this context, quantitative ultrasound is thought as a particularly relevant nondestructive means to probe such materials, because it relies on the use of mechanical waves and thus possesses intrinsic sensitivity to their mechanical properties.

Objectives

This doctoral thesis aims at mechanically characterizing biological multi-tissue interphases, like the soft tissue-to-bone insertion. Without loss of generality, this thesis

focuses on fibrocartilaginous entheses, with particular emphasis on the tendon-to-bone attachment. To tackle this goal, three specific objectives are proposed (see Fig. 2).

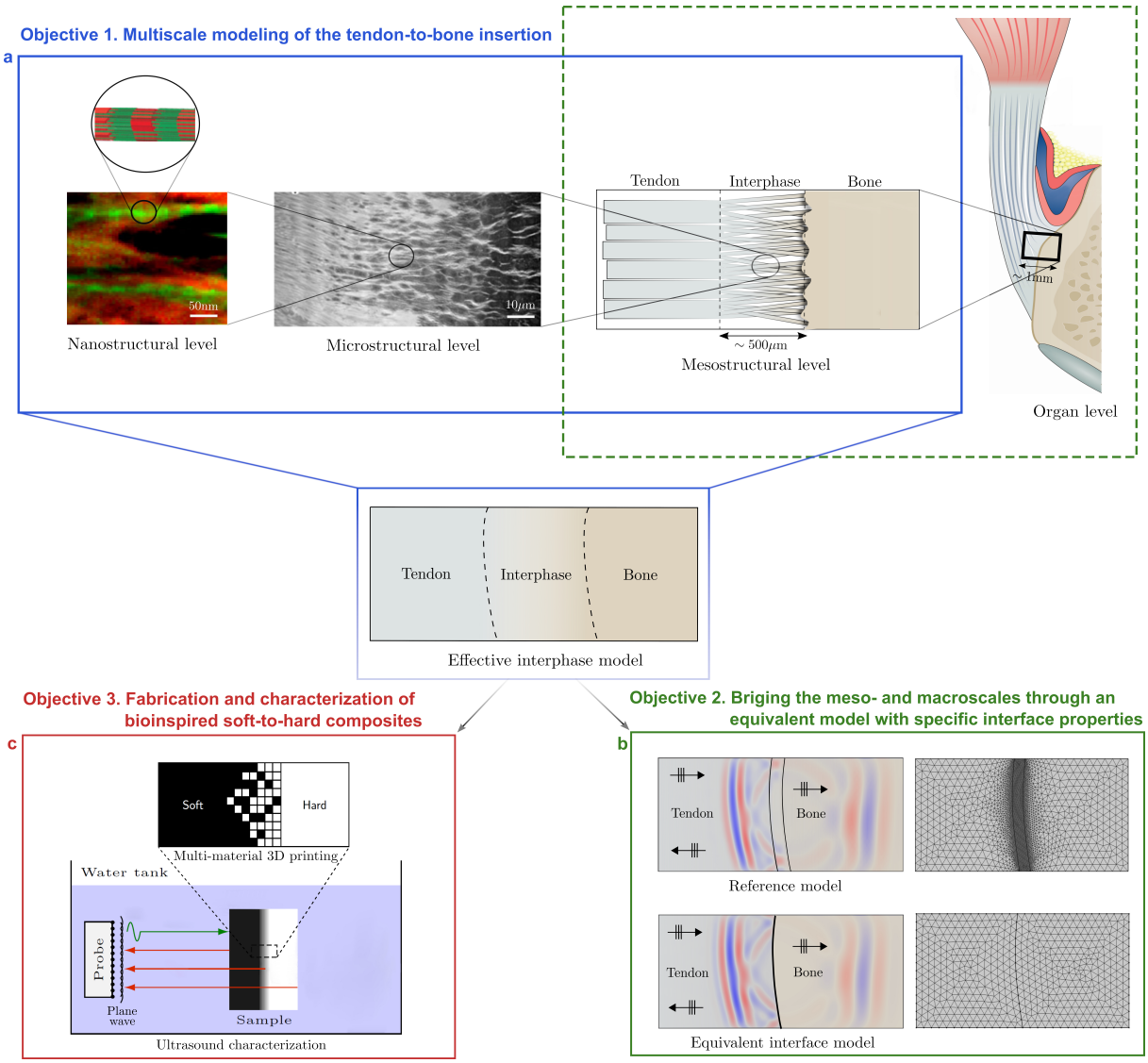

Figure 2 – Schematic representation of the three objectives addressed in this dissertation, along with the proposed methods: (a) Development of a multiscale model to predict the mesoscopic mechanical behavior of the tendon-to-bone interphase based on the knowledge of the elementary constituents at lower length scales. The modeling results (so-called effective interphase model depicted in the central insert) will serve us as a baseline to define the two subsequent objectives; (b) Development of an equivalent model with specific interface properties as an enriched computational strategy to bridge the gap between the meso- and macroscales. The performance of this model will be evaluated in the context of quantitative ultrasound; (c) Design and fabrication of bioinspired multi-material samples using additive manufacturing. The characterization of these samples will be carried out using ultrasound measurements and mechanical modeling of the wave-interphase interactions (images adapted with permission from Refs. [11, 25–27]).

The **first objective** aims at establishing a quantitative relationship between the

structure-composition of the enthesis and its mechanics at the tissue scale (see Fig. 2a). This will be achieved by developing a multiscale model that, based on the knowledge of the compositional features of the tendon-to-bone interphase at lower length scales (*i.e.*, elementary constituents and finely tuned gradients), will allow predicting its overall mechanical behavior at the mesoscopic scale. Such model will further serve us as a baseline to address the two subsequent objectives. Indeed, in view of its future implementation in numerical codes performed at the macroscale, the **second objective** aims at bridging the modeling gap between the tissue scale and the organ scale (see Fig. 2b). This will be carried out by developing an equivalent model with specific interface properties, which retains information of the microstructural features of the interphase. The performance of this enriched model will be evaluated in the context of elastic wave propagation. Based on the results of the multiscale modeling, **the third objective** aims at replicating some mesoscopic features adopted by this biological interphase towards the development of biomimetic strategies in engineering (see Fig. 2c). This will be achieved by designing and fabricating multi-material additively manufactured samples that possess an interphase with bioinspired properties. These samples will be subsequently characterized using ultrasound measurements and mechanical modeling.

The **originality** of the proposed multiscale and multimodal approach is manifold. First, although many different experimental techniques and multiscale models have been proposed to assess the mechanical performance of either the tendon or bone, the **mechanics of this highly specialized interphase** remains a largely unexplored topic, mainly because of its complex and heterogeneous nature confined over a very small region. Second, most studies in biomechanics that aimed to link material structure and composition to function have been mainly conducted in the quasi-static regime, while the **dynamic regime** (*e.g.*, using mechanical waves) has been somewhat less investigated. Third, although several studies have been devoted to the **development of man-made materials** inspired by biological tissues, the fabrication and characterization of multi-material systems possessing bioinspired interphases have not received much attention so far. Fourth, it should be noted that, for addressing the three objectives mentioned above, we are not only taking advantage of the knowledge of the healthy enthesis, but also studying **the impact of damage mechanisms** on its overall mechanical response.

Outline

To address the proposed objectives, this manuscript is organized in four chapters, which are strongly interconnected. Based on earlier literature works, **Chapter 1** provides an overview on the relationships between the structure and the composition of the transitional tissues at the tendon-to-bone attachment, as well as on the mechanisms governing their damage and regeneration. Briefly, in healthy attachments, aligned, soft fibrous tendons attach to stiff bone *via* a very small intermediate fibrocartilaginous region, where the collagen fibers orientation is more disperse than in the tendon. This transitional region also shows an increase in mineral distribution. The heterogeneous and hierarchical structure of the enthesis, which exhibits gradients in structural, compositional, and biomechanical properties, is essential to ensure a smooth transfer of mechanical stresses across the two surroundings tissues. In case of injury as a result of physical overloading, systemic diseases or tissue degeneration, these gradients will not regenerate during

healing and remodeling phases, thereby explaining the relatively high rupture recurrence rates of surgical procedures. Based on these considerations, this chapter also provides an overview of the modeling strategies that have been developed at different length scales. Finally, regarding the clinical vulnerability of the enthesis following an injury, a review of the current interface tissue engineering approaches that attempt to supply biological substitutes of this interphase.

Based on the information about the structural and compositional features at lower length scales gathered in the former chapter, **Chaper 2** focuses on the impact of these features on the overall mechanical response of the enthesis at the macroscale. Towards this goal, a key point of this thesis is to the develop a modeling strategy that accounts for the multiscale and multi-tissue nature of the enthesis. The proposed multiscale model is based on micromechanics homogenization methods that are commonly employed for the assessment of hierarchical composite materials. This approach will allow (1) predicting the effective anisotropic stiffness tensor of the tendon-to-bone insertion by modeling its elastic response at different scales spanning from the nano- to the mesostructural levels, and (2) studying the impact of key parameters (*e.g.*, size of the compliant region and location of the percolation threshold) by tailoring the input parameters (*i.e.*, mechanical properties of the elementary constituents, gradient in mineral content, collagen fibers organization).

To overcome current limitations of computational models that aim at studying the biomechanical behavior of the tendon-to-bone complex at the organ scale, **Chaper 3** focuses on the modeling of dynamic phenomena in heterogeneous media that allows replacing the finite heterogeneous interphase by an equivalent model with specific interface conditions. The focus will be on a wave propagation problem across two dissimilar homogeneous and solid half-spaces (*i.e.*, tendon and bone) separated by a finite interphase layer, whose heterogeneous properties are inspired by the results from the multiscale modeling (recall Chaper 2). The performance of this model will be evaluated in the context of quantitative ultrasound, by comparing the calculated power reflection coefficient to that obtained using different baselines.

Inspired by the results obtained from the multiscale modeling, **Chaper 4** focuses on the design, fabrication and characterization of bioinspired multi-material samples achieved using additive manufacturing. Towards this goal, macroscopically homogeneous and heterogeneous samples will be fabricated using polyjet 3D printing technology. The characterization of these samples will be achieved by measuring longitudinal bulk waves. From the measurements performed on the homogeneous samples, we will first identify relationships between the mechanical properties and the material composition by solving a model-based inverse problem. In a second part, these relationships will be used to feed a wave propagation model that accounts for the structural and material complexity of the functionally graded samples. This approach will allow extracting quantitative information from the measured signals, by systematically comparing the measured and modeled characteristics. Such results could pave the way for characterizing and optimizing multi-material systems that display complex bioinspired features to improve the mechanical efficiency of man-made structures by taking advantage of the intriguing strategies adopted by nature.

Bibliography

[1] M Benjamin, H Toumi, JR Ralphs, G Bydder, TM Best, and S Milz. Where tendons and ligaments meet bone: attachment sites ('entheses') in relation to exercise and/or mechanical load. *J Anat*, 208(4):471–490, 2006.

[2] LM Galatz, CM Ball, SA Teefey, WD Middleton, and K Yamaguchi. The outcome and repair integrity of completely arthroscopically repaired large and massive rotator cuff tears. *J Bone Joint Surg*, 86(2):219–224, 2004.

[3] S Thomopoulos, GR Williams, and LJ Soslowsky. Tendon to bone healing: differences in biomechanical, structural, and compositional properties due to a range of activity levels. *J Biomech Eng*, 125(1):106–113, 2003.

[4] KL Moffat, WS Sun, PE Pena, NO Chahine, SB Doty, GA Ateshian, CT Hung, and HH Lu. Characterization of the structure–function relationship at the ligament-to-bone interface. *Proc Natl Acad Sci USA*, 105(23):7947–7952, 2008.

[5] M Benjamin, T Kumai, S Milz, BM Boszczyk, AA Boszczyk, and JR Ralphs. The skeletal attachment of tendons–tendon 'entheses'. *Comp Biochem Physiol A Mol Integr Physiol*, 133(4):931–945, 2002.

[6] HH Lu and S Thomopoulos. Functional attachment of soft tissues to bone: development, healing, and tissue engineering. *Annu Rev Biomed Eng*, 15:201–226, 2013.

[7] AD Waggett, JR Ralphs, APL Kwan, D Woodnutt, and M Benjamin. Characterization of collagens and proteoglycans at the insertion of the human Achilles tendon. *Matrix Biol*, 16(8):457–470, 1998.

[8] S Thomopoulos, JP Marquez, B Weinberger, V Birman, and GM Genin. Collagen fiber orientation at the tendon to bone insertion and its influence on stress concentrations. *J Biomech*, 39(10):1842–1851, 2006.

[9] JP Spalazzi, AL Boskey, N Pleshko, and HH Lu. Quantitative mapping of matrix content and distribution across the ligament-to-bone insertion. *PLoS One*, 8(9):e74349, 2013.

[10] B Wopenka, A Kent, JD Pasteris, Y Yoon, and S Thomopoulos. The tendon-to-bone transition of the rotator cuff: a preliminary raman spectroscopic study documenting the gradual mineralization across the insertion in rat tissue samples. *Appl Spectrosc*, 62(12):1285–1294, 2008.

[11] B Alexander, TL Daulton, GM Genin, J Lipner, JD Pasteris, B Wopenka, and S Thomopoulos. The nanometre-scale physiology of bone: steric modelling and scanning transmission electron microscopy of collagen–mineral structure. *J R Soc Interface*, 9(73):1774–1786, 2012.

[12] Y Hu, V Birman, A Deymier-Black, AG Schwartz, S Thomopoulos, and GM Genin. Stochastic interdigitation as a toughening mechanism at the interface between tendon and bone. *Biophys J*, 108(2):431–437, 2015.

[13] GM Genin, A Kent, V Birman, B Wopenka, JD Pasteris, PJ Marquez, and S Thomopoulos. Functional grading of mineral and collagen in the attachment of tendon to bone. *Biophys J*, 97(4):976–985, 2009.

[14] Y Liu, S Thomopoulos, C Chen, V Birman, MJ Buehler, and GM Genin. Modelling the mechanics of partially mineralized collagen fibrils, fibres and tissue. *J R Soc Interface*, 11(92):20130835, 2014.

[15] L Rossetti, LA Kuntz, E Kunold, J Schock, KW Müller, H Grabmayr, J Stolberg-Stolberg, F Pfeiffer, SA Sieber, R Burgkart, and AR Bausch. The microstructure and micromechanics of the tendon–bone insertion. *Nat Mater*, 16(6):664, 2017.

[16] J Sartori, S Köhring, S Bruns, J Moosmann, and JU Hammel. Gaining insight into the deformation of Achilles tendon entheses in mice. *bioRxiv*, 2021.

[17] A Inoue, E Chosa, K Goto, and N Tajima. Nonlinear stress analysis of the supraspinatus tendon using three-dimensional finite element analysis. *Knee Surg Sports Traumatol Arthrosc*, 21(5):1151–1157, 2013.

[18] I Wakabayashi, E Itoi, H Sano, Y Shibuya, R Sashi, H Minagawa, and M. Kobayashi. Mechanical environment of the supraspinatus tendon: a two-dimensional finite element model analysis. *J Shoulder Elbow Surg*, 12(6):612–617, 2003.

[19] H Sano, I Wakabayashi, and E Itoi. Stress distribution in the supraspinatus tendon with partial-thickness tears: an analysis using two-dimensional finite element model. *J Shoulder Elbow Surg*, 15(1):100–105, 2006.

[20] C Quental, J Folgado, J Monteiro, and M Sarmento. Full-thickness tears of the supraspinatus tendon: A three-dimensional finite element analysis. *J Biomech*, 49(16):3962–3970, 2016.

[21] H Sano, M Tokunaga, M Noguchi, T Inawashiro, T Irie, H Abe, and AT Yokobori Jr. Tight medial knot tying may increase retearing risk after transosseous equivalent repair of rotator cuff tendon. *Biomed Mater Eng*, 28(3):267–277, 2017.

[22] T Funakoshi, N Suenaga, H Sano, N Oizumi, and A Minami. In vitro and finite element analysis of a novel rotator cuff fixation technique. *J Shoulder Elbow Surg*, 17(6):986–992, 2008.

[23] A Tits and D Ruffoni. Joining soft tissues to bone: insights from modeling and simulations. *Bone Rep*, page 100742, 2020.

[24] EI Avgoulas, MPF Sutcliffe, SW Linderman, V Birman, S Thomopoulos, and GM Genin. Adhesive-based tendon-to-bone repair: failure modelling and materials selection. *J R Soc Interface*, 16(153):20180838, 2019.

[25] H Tempfer, C Lehner, M Grütz, R Gehwolf, and A Traweger. *Biological augmentation for tendon repair: lessons to be learned from development, disease, and tendon stem cell research*. Springer, 2020.

[26] AG Schwartz, JD Pasteris, GM Genin, TL Daulton, and S Thomopoulos. Mineral distributions at the developing tendon enthesis. *PloS One*, 7(11):e48630, 2012.

[27] E Gracey, A Burssens, I Cambré, G Schett, R Lories, IB McInnes, H Asahara, and D Elewaut. Tendon and ligament mechanical loading in the pathogenesis of inflammatory arthritis. *Nat Rev Rheumatol*, 16(4):193–207, 2020.

Chapter 1. Soft tissue-to-bone attachments

Contents

1.1 Introduction

The aim of this chapter is to provide the reader with an overview on the structure, function and biomechanical properties of soft tissue-to-bone insertions. In the first section, we briefly describe of the relationship between the structure and function of soft tissue and bone, and subsequently focus on the integration between them. The second section is dedicated to the description of the pathologies and injuries that may affect the enthesis, along with its mechanical response after healing. Based on the structure-function relationship of the enthesis, the third section reviews the analytical and computational models that have been proposed to study fundamental anchoring mechanisms at the microscale. Current organ scale models aiming at understanding the impact of damage and at targeting reattachment procedures are also reviewed in this section. A fourth section exposes the current approaches developed in the field of interface tissue engineering to supply biological enthesis-like substitutes. Based on all these recent findings, a final section recapitulates the underlying motivations for this thesis, as well as current routes that are worth being explored.

1.2 Structure–function relationships of collagen-based tissues

The support and movement of the musculoskeletal system not only depends on the coordinated action of multiple types of collagen-based tissues such as tendon, ligament, and bone, but also on the connective tissues that join them. Thereby this section is dedicated to the description of the structure-function relationships of these collagen-based tissues.

1.2.1 Tendon and ligament

Tendon and ligament are fibrous connective tissues, which are respectively responsible for the attachment of muscle-to-bone and bone-to-bone, in order to ensure the transmission of forces or to provide stability to the joints. Tendon and ligament have a rather similar collagen-based hierarchical structure and show a low cellular heterogeneity from the molecular- to the tissue-levels. At the molecular scale, the constitutional building block of the tendon is tropocollagen. Five of these builiding blocks are further grouped together to constitute a microfibril and then aggregate to form fibrils at the nanoscale, which are themselves grouped into fibers at the microscale. The fibers are denoted as primary bundles that are assembled in the next higher hierarchical structure, the fascicle (secondary bundle) at the mesoscale. Finally, fascicles are bundled together by a connective tissue sheath called the endotenon, which is itself surrounded by another connective tissue layer, the epitenon, to finally build up the whole tendon at the tissue level (see Fig. 1.1) [1]. At each level, collagen is interspersed with a varying amount of non-collagenous matrix rich in water and proteoglycans, which altogether contribute to the mechanical properties of the tendon [2].

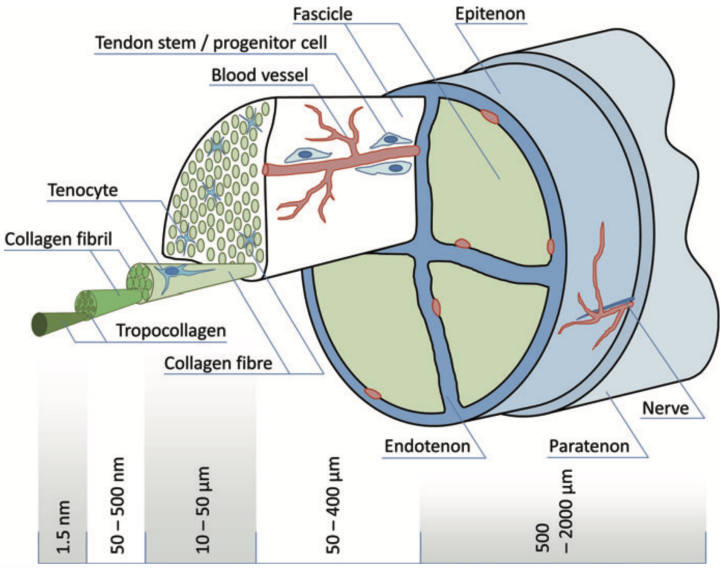

Figure 1.1 – Hierarchical organization of the tendon: collagen molecules are bundled into progressively larger subunits from fibrils to fascicles, interspersed with a varying amount of non-collagenous matrix (image reproduced with permission from Ref. [1]).

1.2.2 Bone

Bone is the main constituent of the skeletal system and has a very complex hierarchical structure (see Fig. 1.2), which is optimized to achieve remarkable mechanical performances [3]. At the nanoscale, the main elementary constituents are collagen, mineral, non-collagenous organic proteins and water, which are grouped together to form collagen fibrils with embedded minerals at the sub-nanoscale. Further, the fibrils are assembled into fibers that are arranged in geometrical patterns forming lamellae at the sub-microscale, which are subsequently grouped together to form osteons, Haversian systems at the microscale. Two types of bone tissue can be distinguished at the macroscale. Cortical bone, also known as compact bone, is a dense and low porosity solid medium, which forms the outer wall of the bones and is mainly responsible for the supportive and protective function of the skeleton. In contrast, trabecular bone, also known as cancellous bone, is a highly porous network that is located in the inner parts of bones, which provides strength to the skeleton and allows transferring mechanical loads.

Although collagen is the main building block of tendon and bone, their mechanical response is significantly different and depends upon their anatomical locations. To serve as an example, Figure 1.3 shows the difference in the stress-strain curves between mouse tail tendon and parallel fibered bone. The light gray area shows the elastic region of the stress–strain curve, which corresponds to the stored elastic strain energy density of tissue during a loading cycle [5]. The dark gray area corresponds to the energy density in the post-yield deformation, where damage and plastic deformation occur in the tissue. As can be seen, bone has a higher stiffness and strength compared to tendon, which prevent excessive deformation upon loading. These characteristics are mainly achieved thanks to the presence of mineral particles into the collagen-based structure at lower length scales [6]. Nevertheless, smaller area under the stress–strain curve of bone indicates a

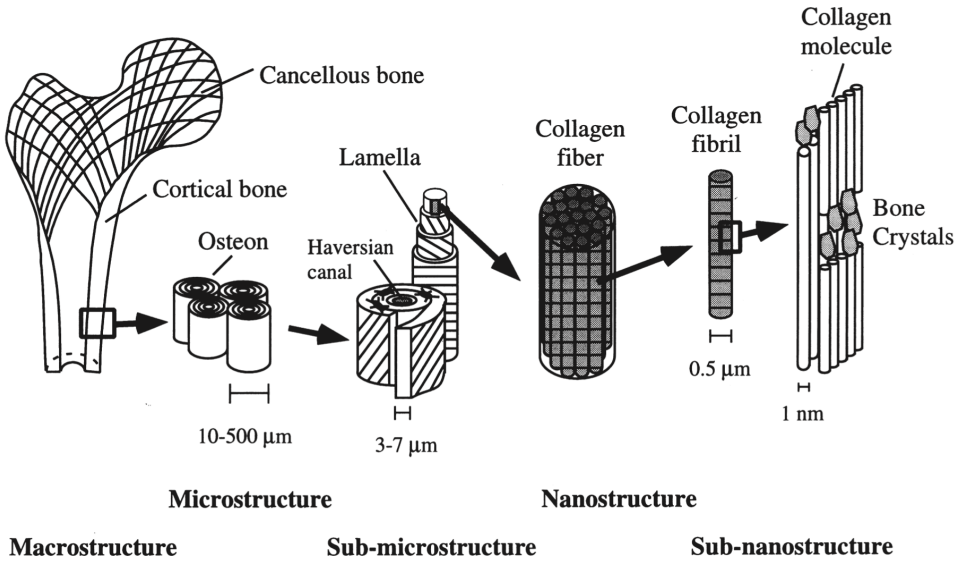

Figure 1.2 – Hierarchical organization of bone, from the mineral crystals and collagen molecules at the sub-nanoscale to the whole organ at the macroscale (image reproduced with permission from Ref. [4]).

lower toughness and small deformation rates compared to tendon, thereby allowing the tendon to withstand tension during a loading cycle and providing rigidity combined with flexibility to transmit the mechanical forces of muscle to bone.

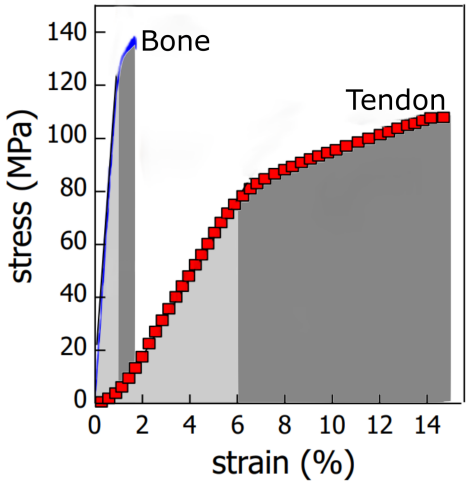

Figure 1.3 – Example of stress–strain curves for mouse tail tendon (in red) [7] and parallel fibered bone (in blue) [8]. Both tissues were loaded in tension in the direction of the collagen fibrils. The elastic region is highlighted by the light gray area, while the plastic region is shaded in dark gray (image adapted with permission from Ref. [5]).

At the tissue level, the Young's modulus of tendon is about 0.4 GPa in the direction of muscle force during physiologic loading conditions [9, 10], and around 20 GPa for cortical bone with respect to the main bone axis (osteon direction) [11, 12]. In this way, the

interphase joining tendon and bone plays a crucial role by achieving a trade-off between strength and toughness to effectively transfer stresses across these two tissues with a mismatch in mechanical properties (see Tab. 2.1) [13].

Hierarchical level	Collagen-based tissue	Young's modulus, E (GPa)	References
Nano	Molecule	$1.2 - 9.6$	[14]
Sub-micro	Non-mineralized fibril	$0.43 - 2.9$	[15–17]
	Mineralized fibril	$2.4 - 21$	[6, 17]
Micro	Non-mineralized fiber	$0.03 - 1.1$	[14]
	Mineralized fiber	$8.5 - 16.7$	[18, 19]
Macro	Non-mineralized tendon	$0.04 - 1.2$	[9, 10]
	Cortical Bone	$18 - 22$	[11, 12]

Table 1.1 – Mechanical properties range of collagen-based tissues at multiple hierarchical levels.

1.2.3 Soft tissue-to-bone enthesis

Entheses are multi-tissue interphases, whose composition, and therefore structure, is continuously varying over a very small transition region from tendon to bone in response to the mechanical environment (see Fig. 1.4a). In comparison to the vast body of literature on soft tissues and bone, much less is known about this biological interphase. According to the musculoskeletal site of insertion, entheses can be classified as fibrous or fibrocartilaginous [20]. At fibrous (or indirect) insertions, tendon or ligament attaches to the bone through mineralized collagen fibers that directly extend into the bone at an acute angle, as for example the insertion of the deltoid tendon into the humerus or the tibial insertion of the medial collateral ligament. Fibrocartilaginous (or direct) insertions attach tendon or ligament to bone through a transitional layer of fibrocartilage. The focus here is on fibrocartilaginous insertions, since they present a higher clinical relevance, for instance regarding injuries at the rotator cuff tendon, the anterior cruciate ligament and the Achilles tendons. Fibrocartilaginous insertions are generally divided into four distinct regions with different compositions, functions, and biomechanical properties (see Fig. 1.4b): (1) the tendon or ligament, which consists of aligned type I collagen fibers with a small amount of non-collagenous proteins (NCPs), including proteoglycans and the remaining volume filled with water. The cell types commonly found in this region are fibroblasts like stromal cells, commonly referred to as tenocytes [21]; (2) a non-mineralized fibrocartilaginous region, which is an avascular zone consisting of unmineralized types I, II and III collagen fibers and proteoglycan aggrecan [22]; (3) a mineralized fibrocartilaginous region, which is mostly characterized by partially mineralized type II collagen fibers, the proteoglycan aggrecan being produced by fibrocartilage cells or fibrochondrocytes between bundles of collagen fibers, which are suspected to be involved in the transmission of mechanical loads [23]; and (4) the bone, which is a composite material that mainly consists of highly mineralized type I collagen. Although these different tissue regions are compositionally distinct, they are structurally continuous. Moreover, fibrocartilaginous entheses are believed to dissipate different types of mechanical stresses across the two surrounding tissues depending on their anatomical locations (see Fig. 1.4c) [23, 24]. Besides the tensile force generated as a result of stretching, entheses also are subject to local compressive stresses, especially at the junction with bone at an oblique angle. It is also

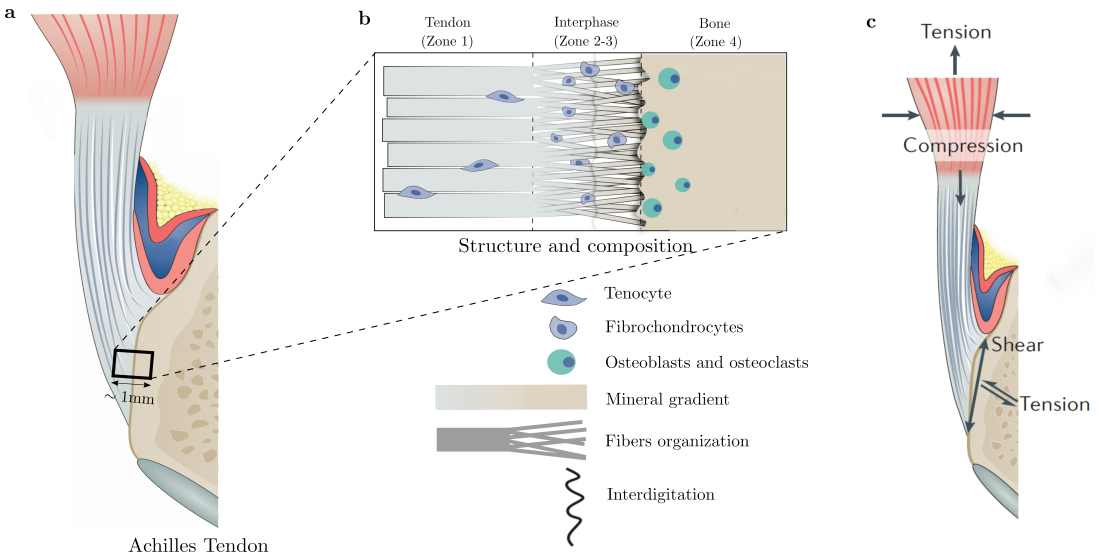

Figure 1.4 – (a) Organ level illustration of the tendon-to-bone attachment at the insertion site corresponding to the Achilles tendon; (b) Schematic of the attachment at the microstructural level, highlighting the gradients in composition and structure across the tendon-to-bone interphase; (c) Mechanical mechanical forces that can be exerted on Achilles tendons, where tensile force is generated as a result of tissue stretching along its longitudinal direction (fiber direction), compressive force is exerted on tendon in a direction that is to a certain extent perpendicular to its longitudinal axis, and shear force can occur at the insertion site. Note that additional mechanical forces can be expected under varying loading conditions at different anatomical locations (image adapted with permission from Refs. [26, 27]).

acknowledged that internal shear forces take place between the deep part of the enthesis and the bone during movement of the articulation [25]. In the following subsections, we briefly review the main compositional and structural features at different hierarchical levels that contribute to the mechanical effectiveness of the enthesis.

A. Fiber architecture and organization

Regardless of the considered medium –soft tissue, enthesis or bone–, all these regions substantially have a similar hierarchical collagen-based structure starting with collagen molecules at the nanoscale up to a pattern of collagen fibers surrounded by an extracellular matrix at higher scales [28]. Non-mineralized collagen fibers are usually strong in tension, but rather weak in compression [29]. However, when pervaded by mineral crystals, their constitutive behavior results more brittle and stiffer (see next subsection for further details on the mineralization). The spatial arrangement of collagen fibers largely depends on the the anatomical location of the enthesis. Experimental approaches addressed to explore the orientation of collagen fibers distribution indicated that, moving from the soft tissue to bone, the insertion site shows a decrease in the organization of collagen fibers [30–32].

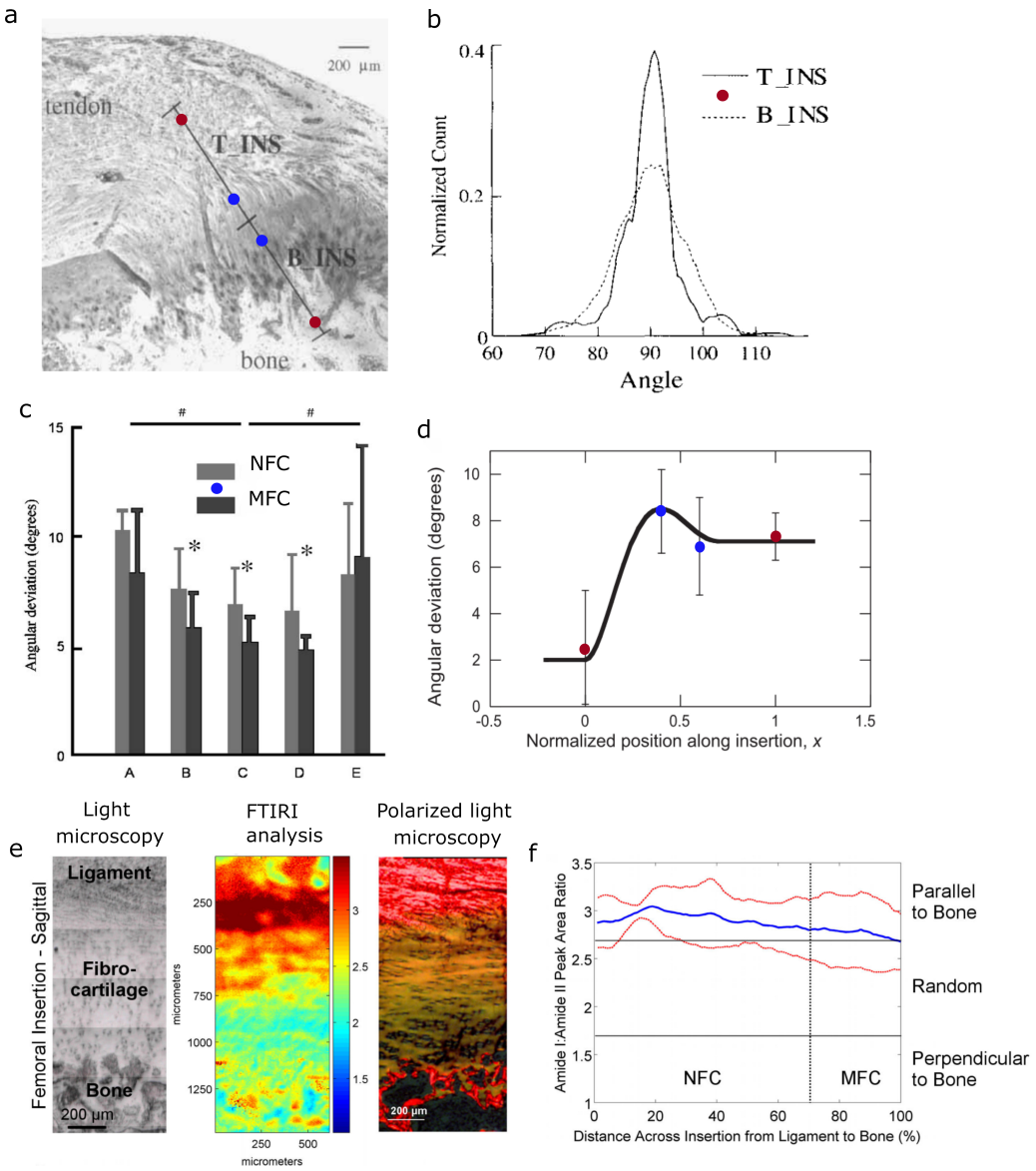

Figure 1.5 – Collagen fibers organization at the soft tissue-to-bone attachment: (a) Histological image of the tendon-to-bone attachment of the rat supraspinatus. Polarized light microscopy was used to quantitatively identify the collagen fibers orientation at two locations, near the tendon end of the insertion site (T-INS) and near the bony end of the insertion site (B-INS); (b) Statistical analysis showing that the angular distribution of collagen fibers was wider in the bony insertion than in the tendon insertion, where 90°-orientation indicates the main tendon axis; (c) Angular deviation of the collagen fibers measured with polarized light microscopy at different locations of the fibrocartilaginous regions (A–E); (d) Angular deviation of the collagen fibers along the normalized position from tendon ($x = 0$) to bone ($x = 1$), which was approximated by interpolating data from two different experimental studies. Red points were taken from the distributions (T-INS and B-INS) in Fig. 1.4b, whereas blue points were directly obtained from measurements performed in the fibrocartilaginous regions in Fig. 1.4c. (e) Light microscopy images of the anterior cruciate ligament-to-bone attachement at bovine tibiofemoral joints. Fourier transform infrared spectroscopic imaging (FTIRI) showing collagen orientation as determined by the amide I:II ratio evolving from parallel (red) to randomly oriented (blue); (f) Line profile analysis generated from the spectral data indicating the average collagen fibers orientation becomes more random while progressing towards bone; blue and red lines represent mean values and standard deviation, respectively (images adapted with permission from Refs. [30, 33, 34]).

For instance, polarized light microscopy was used to quantify the collagen fibers orientation at the rotator cuff enthesis of rats, and the results indicated that, in the tendon region, collagen fibers are rather parallely aligned, whereas their orientation becomes more and more disorganized as they approach the bone (see Fig. 1.5a–c) [30, 33]. Similar results were found using Fourier transform infrared spectroscopy at another anatomical location, *i.e.*, the knee joint, where the ligament attaches to bone [31, 34]. Collagen fibrils were shown to be initially parallely-oriented in the ligament region, while progressing across the interphase, a more random orientation towards the mineralized fibrocartilaginous region was observed (see Fig. 1.5d–e).

In another related study based on confocal microscopy, it was shown that both the geometry and composition of the tendon fibers changed before anchoring to bone. Thicker tendon fibers, containing mostly type I splayed and unravel into thinner interphase fibers, containing mostly type II collagen (see Fig. 1.6a). In a recent study, collagen fibers were tracked in 3D at the tendon enthesis in mice using micro-computed tomography [32]. Going from the tendon to bone, the number of fibers is nearly constant but the fibers cross-sectional area decreases and these start twisting towards the insertion site (see Fig. 1.6b). The highest fiber curvatures were found in the non-mineralized fibrocartilaginous region. Overall, these branching and twisting mechanisms are supposed to contribute to a homogeneous distribution of stress among the fibers and to increase the shear stiffness of the tendon, thus preventing fibers from sliding relative to one another.

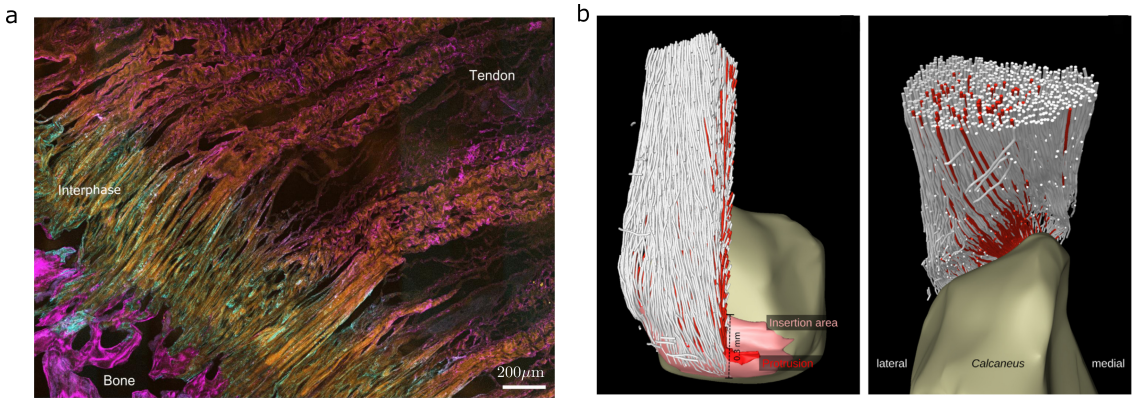

Figure 1.6 – Additional characteristics of the collagen fibers organization at the tendon-to-bone attachement: (a) Confocal reflection microscopy image at the pig's Achilles tendon revealing the geometrical and compositional transitions of fibers, where thicker tendon fibers, containing mostly type I collagen (magenta), splayed and unravel into thinner interphase fibers, containing mostly type II collagen (cyan), before attaching to bone (image adapted from Ref. [35]); (b) 3D fibers tracking at the Achilles tendon in mice using micro-computed tomography evidencing the twisting of fibers from tendon to bone (image adapted with permission from Ref. [32]).

B. Mineral grading

The interaction of collagen with mineral crystals plays a specific role in the mechanical responses of partially mineralized tissues. Although there are some exceptions, like the mineralized turkey leg tendon [36], the major difference between tendon and bone

concerns mineralization. Mineralized tissues are usually providing higher stiffness and more strength compared to non-mineralized tissue during mechanical loading [6, 37]. Regarding bone, during the mineralization process, mineral crystals are nucleated and grow within the hierarchal collagen structure [38]. Several experimental studies examined the local distribution of minerals across soft tissue-to-bone insertions and underlined the spatial increase in mineral content from soft tissue to bone at different anatomical locations [31, 34, 40]. Raman spectroscopy was used to quantify the distribution of minerals at the rotator cuff enthesis of rats, and the results indicated that the mineralization gradient from tendon to bone can be reasonably well fitted by a linear approximation (see Fig. 1.7a–b) [40].

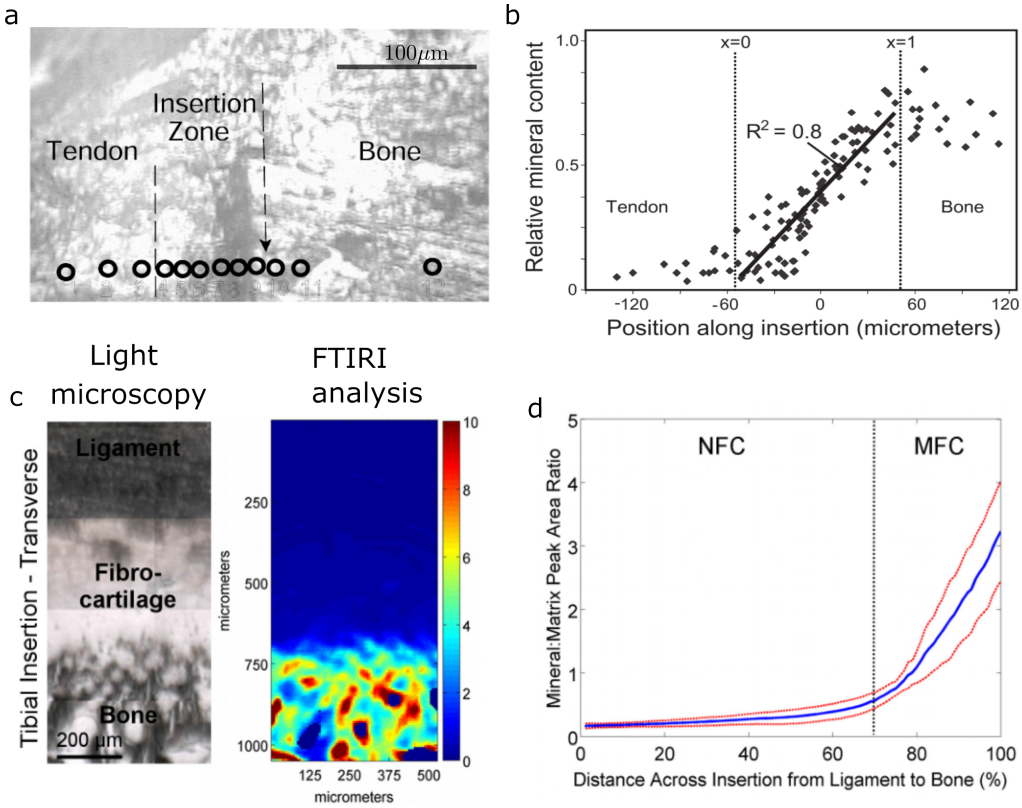

Figure 1.7 – Mineral distribution at soft tissue-to-bone attachments: (a) Light microscopy images of the tendon–bone insertion in the shoulders of rat used to track the position of the Raman spectroscopic measurements (*i.e.*, circles); (b) Relative mineral content obtained from Raman spectroscopy measurements across the insertion zone showing an approximately linear increase from tendon ($x = 0$) to bone ($x = 1$); (c) Light microscopy images at the attachment of the anterior cruciate ligament to bone at bovine tibiofemoral joints. FTIRI shows an increase in mineral content from ligament to bone (blue and red colors indicate low and high mineral content, respectively); (d) Line profiles analysis generated from the spectral data depicting an exponential increase in mineral content across the fibrocartilaginous region, where blue and red lines represent mean values and standard deviation, respectively (images adapted with permission from Refs. [34, 39]).

Considering a different anatomical location where the anterior cruciate ligament attaches to bone, *i.e.*, the knee joint, results based on FTIRI revealed an exponential increase in mineral content when going from the ligament to bone (see Fig. 1.7c–d) [34].

C. Interdigitation mechanism

Other factors that are believed to play an important role in the mechanical performance of soft tissue-to-bone attachements are the interdigitation mechanism and interfacial roughness present at the transition between the mineralized fibrocartilage and bone [41]. The same is also expected for the interface between the non-mineralized and mineralized fibrocartilaginous regions. [42]. The interdigitation of the anteromedial bundles at the attachment of the anterior cruciate ligament to bone has been shown to be essential for increasing the resistance to multidirectional loading (see Fig. 1.8a) [43]. Such adaptation to the complex loading environment has also been observed for meniscal attachments of the knee joint (see Fig. 1.8b) [44]. Altogether, the interdigitation morphology and the splaying of interface fibers increase the area of attachment over which forces could be dispatched and thus result in an increase of toughness [45]. A numerical study has further confirmed that the interdigitation between the non-mineralized and mineralized fibrocartilaginous regions of the tendon-to-bone attachment at a mouse rotator cuff acts as a toughening mechanism (see Fig. 1.8c) [42].

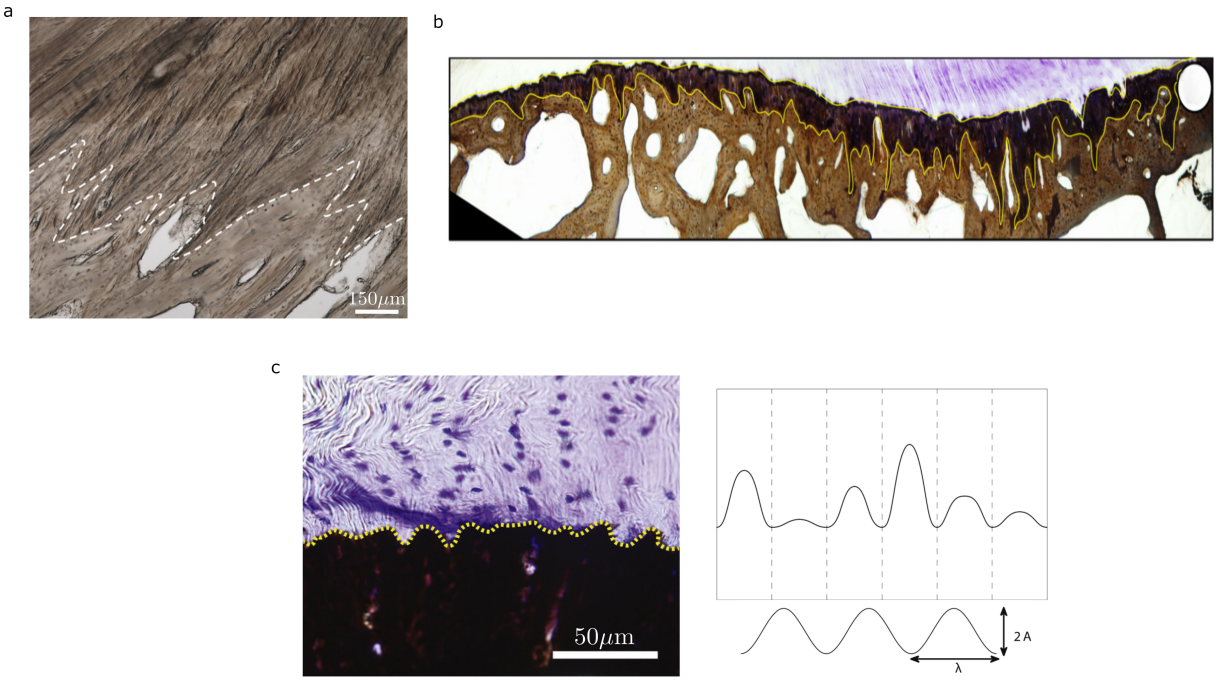

Figure 1.8 – Interdigitation morphology at the soft tissue-to-bone attachment: (a) Sagittal view of the anteromedial bundles of the human anterior cruciate ligament showing a significant degree of interdigitation between the mineralized fibrocartilage and bone (image adapted from Ref. [43]); (b) Interdigitations morphology of the human meniscal attachments, first between non-mineralized fibrocartilage (stained in blue) and mineralized fibrocartilage (stained in black), and second with high levels of heterogeneity between mineralized fibrocartilage and bone (stained in brown) (image adapted from Ref. [44]); (c) Light microscopy image of the interfacial roughness between the non-mineralized fibrocartilage (stained in blue) and the mineralized fibrocartilage (stained in black) at the tendon-to-bone attachment of mouse. This roughness was modeled by a sinusoid with varying wavelength λ and amplitude A (image adapted with permission from Ref. [42]).

1.3 Injury, healing and regeneration

The injury of soft tissue-to-bone insertion sites is among the most common musculoskeletal disorders, with more than 17 million injuries occurring each year, whose related costs amount to tens of billions of dollars a year in the United States alone [46]. In contrast to bone, which has the ability to self-repair during healing, the interphase between tendon and bone is not likely to regenerate, even in the long term.

1.3.1 Characteristics and locations of injuries

Generally, enthesis injuries can be categorized as acute or chronic [13]. Although several factors can be common to all injuries, acute injuries are typically related to extrinsic factors like environment, physical loading or training. Chronic injuries, however, also contain intrinsic factors such as tissue degeneration, aging and systemic diseases. Regardless of their origin (*i.e.*, extrinsic or intrinsic factors), injuries affecting the enthesis generally manifest through fissures or tears at the insertion site. Benjamin et al. [47] evidenced the presence of micro-holes, typically $100 - 400$ μm wide, near the cortical shell, in a region encompassing both the mineralized fibrocartilage and bone. Moreover, Rufai et al. [48] depicted distinct features at the Achille tendon enthesis, in particular so-called longitudinal fissures and transverse tears. Longitudinal fissures ($\sim$ 1 cm) extended from the neighbouring tendon into the fibrocartilaginous region, whereas transverse tears ($\sim$ $200 - 600$ μm) occurred at the tendon-bone junction.

Clinically, enthesis-related pathologies include rotator cuff disease, Achilles tendinosis and sports injuries impacting for instance golfer's elbow and jumper's knee. The rotator cuff disease is the most common pathology, which results particularly challenging because it is associated with changes that may impact cells, vascularity, extracellular matrix components and many other related factors [49]. Achilles tendinosis generally consists in a degeneration of the tendon that inserts into the calcaneus. Tennis elbow occurs at the humerus and is characterized by the formation of a disorganized collagen matrix at the interphase [20], whereas jumper's knee typically affects the tendon-bone junction of the lower portion of the patella or quadriceps tendons [20, 50]. Another group of pathologies affecting the entheses are called enthesopathies [51]. These can be initiated by repeated mechanical overloading, which results in microdamage and/or diseases such as arthritis [52].

Entheses injury commonly take place both at intra-articular entheses like the rotator cuff, the anterior cruciate ligament and at extra-articular entheses such as the Achilles tendon, the medial collateral ligament [49]. Although these sites all consist of four well-identified regions, their geometry, structure, composition and disease susceptibility may slightly differ from each other [23, 43, 48, 53], which in turn may lead to different failure modes [54]. Regardless of the injury, pathology, or the affected musculoskeletal site, if surgical repair is required, the tendon/ligament typically needs to be reattached back to bone, which represents a major challenge due to the mismatch in mechanical properties between tendon and bone.

1.3.2 Mechanical response of the regenerated tissue during healing

The healing process following injuries usually consists of a number of overlapping stages (*e.g.*, inflammatory, fibroblastic, remodeling) (see Fig. 1.9a-b) [13]. During these, complex interactions between a range of tissue growth factors and cells take place, whereby the attachment site becomes more disorganized by developing scar-like tissue with inferior mechanical properties than in the healthy conditions [45]. With time, healing is characterized by a progressive re-establishment of the collagen link between the tendon and bone, but there is still a lack of continuity between the collagen fibers [24]. Moreover, there is no evidence of mineral gradient across the interphase after healing (see Fig. 1.9c). Altogether, these observations suggest that the enthesis does not recover its pristine mechanical properties after the healing phase, which in turn lead to a high re-tear incidence [55].

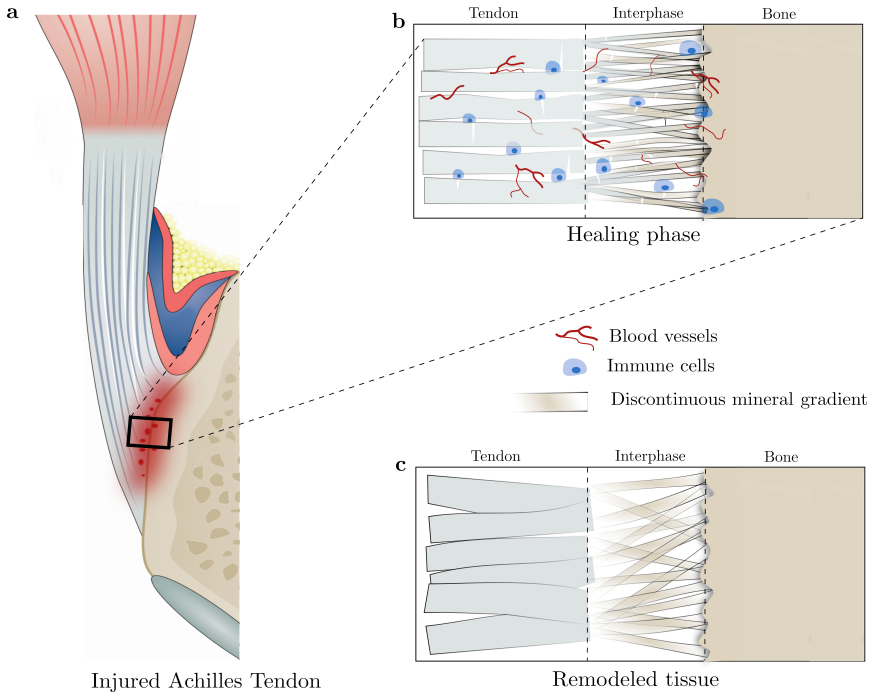

Figure 1.9 – Schematics of an injured tendon-to-bone attachement: (a) Insertion site corresponding to the Achilles tendon; (b) Healing phase after microdamage, highlighting the role played by blood vessels and immune cells in repairing the injured tissue; (c) Remodeled tendon-to-bone attachment, displaying highly disoriented collagen fibers with no evidence of continuous mineral gradient content across the interphase.

1.4 Mechanical modeling

Based on the reported experimental evidences at lower length scales (*e.g.*, organization of the collagen fibers, mineral gradient) and at the tissue scale (interdigitation and interfacial roughness), as well as on the mechanisms responsible for the different types of injuries, different analytical and computational models have been proposed to investigate the mechanical behavior of the enthesis.

1.4.1 Modeling of fundamental anchoring mechanisms

Several models have been proposed to investigate the fundamental anchoring mechanisms of the enthesis responsible for an effective load transfer between the tendon and bone. Among these, a few models were proposed to understand how the compositional features at lower length scales affect the overall mechanical behavior of the enthesis at the tissue scale [39, 56]. Biomechanical models were initially proposed by considering a gradient in mineral concentration and fibers orientation at the microscale. In a pioneering study [39], the stiffness of partially mineralized fibers was calculated by randomly distributing mineralized and unmineralized collagen among a cylindrical collagen structure using Monte Carlo simulations (see Fig. 1.10a). Combining these results with profiles of the mineral content and fibers organization across the interphase (see Fig. 1.10b), which were extrapolated from measurements (recall Figs. 1.5d and 1.7b), allowed estimating the mechanical properties of the partially mineralized tissue at the mesoscale (see Fig. 1.10c).

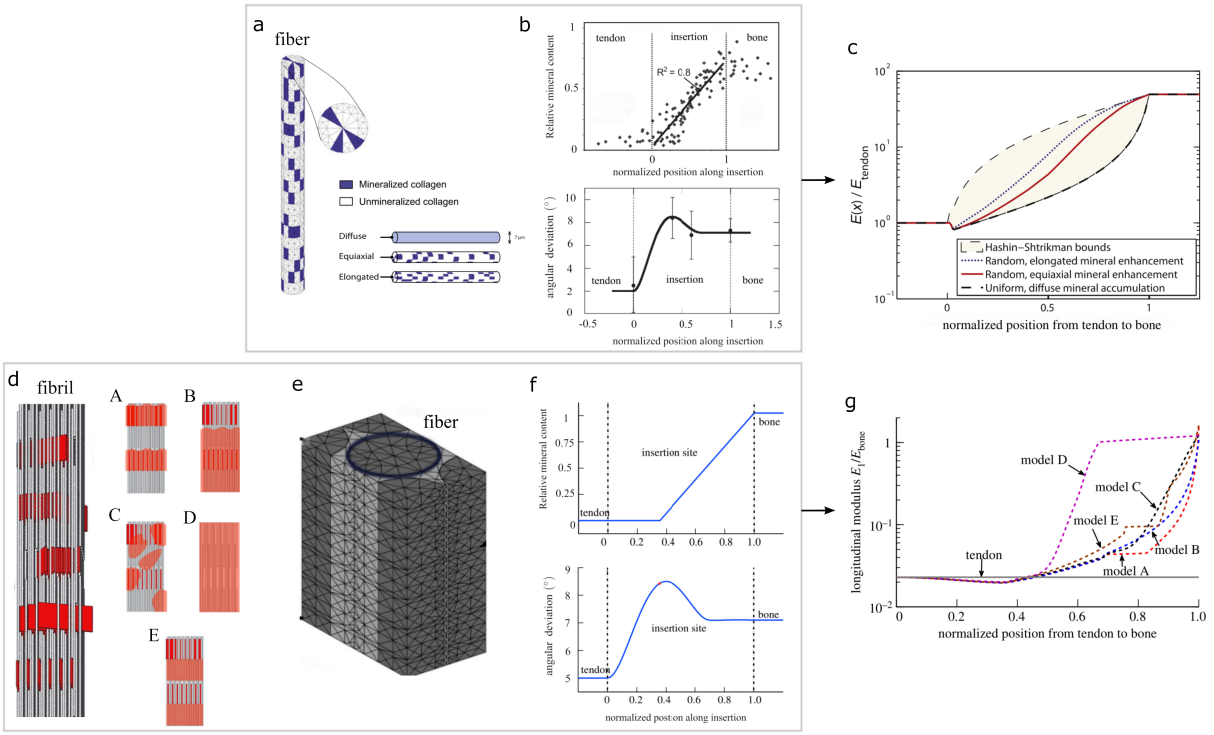

Figure 1.10 – Stochastic finite-element models of tendon-to-bone insertion: (a) Microscale modeling of partially mineralized fibers with randomly distributed clusters of mineralized and unmineralized collagen among a cylindrical collagen structure using Monte Carlo simulations; (b) Distributions of mineral content and mean collagen fibers orientation across the interphase derived from experimental measurements; (c) Macroscale estimation of the Young's modulus across the interphase. A small compliant region with stiffness lower than either tendon or bone can be observed; (d) Sub-microscale models of the partially mineralized collagen fibrils by accounting for different scenarios for the interaction between minerals and collagen; (e) Partially mineralized fibers model, whereby the random accumulations of extrafibrillar bioapatite are modeled using the same approach as in Ref. [39]; (f) Distributions of mineral content and mean collagen fibers orientation across the interphase derived from experimental measurements; (d) Macroscale estimation of the longitudinal Young's modulus (along the main fiber axis) for the different mineralization pathways. Note that, for these models, the compliant region is now larger, deeper, and shifted towards the nonmineralized fibrocartilaginous region (*i.e.*, $x = 0.35$) (images adapted with permission from Refs. [39, 56]).

Later, the same group introduced a progressive stiffening model for collagen fibrils by accounting for different scenarios for the mineralization process to estimate the mechanical properties of the partially mineralized tissue at the macroscale (see Fig. 1.10d–f) [56]. The results indicated how combinations of specific sequences of mineralization and collagen fibers organization at lower scales can provide a significant stiffening of the tissue (see Fig. 1.10g). Apart from these models based on stochastic finite-element simulations, a few attempts based on micromechanical approaches also have been implemented. In this vein, the effective stiffness of a composite containing multiple classes of aligned ellipsoidal inclusions with a relatively high volume fraction was estimated using a homogenization method [57]. The potential application is related to the graded tissue interphase at the soft tissue-to-bone attachment. However, this modeling accounted for a limited number of length scales, only spanning from the sub-microscale to the microscale.

1.4.2 Organ scale modeling towards orthopedic applications

Musculoskeletal injuries are very common and, in case of rupture, the reattachment of soft tissue to bone is necessary. Unfortunately, such surgical intervention exhibits a high rate of failure due the lack of integrative solutions for restoring the pristine properties of the enthesis. This clinical burden has, triggered the development of computational models at the organ scale targeting relevant orthopedic challenges. Current organ scale models were developed with the aim of understanding the damage and failure mechanisms, as well as to improve the outcome of therapeutic procedures [58–64]. Towards these goals, a two-dimensional finite element model of the supraspinatus tendon-to-bone attachment with geometrical information based on magnetic resonance images was developed (see Fig. 1.11a) [60].

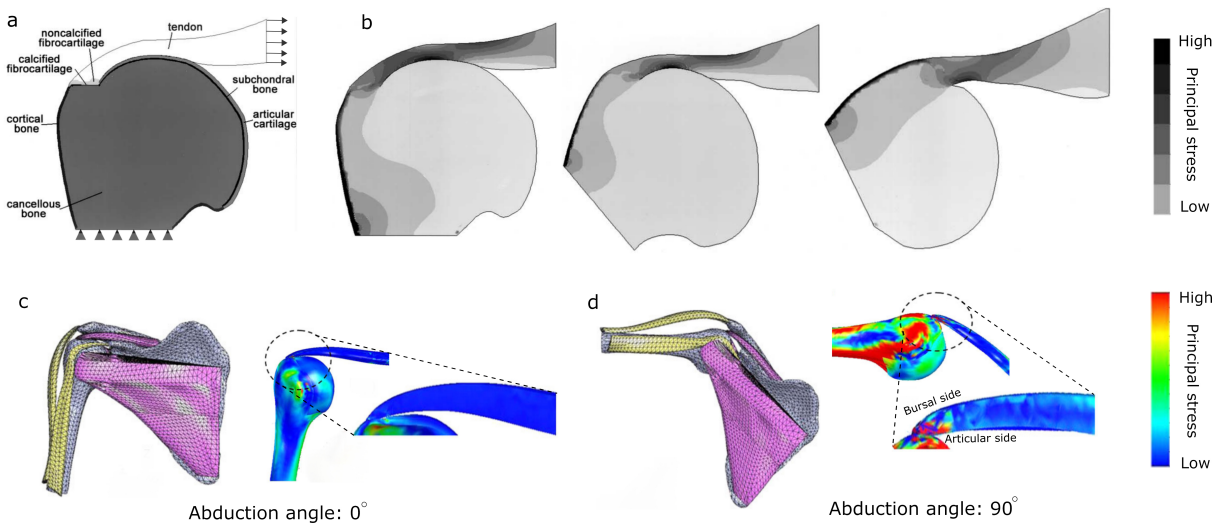

Figure 1.11 – (a) Finite element model of the supraspinatus tendon-to-bone attachment using a geometrical configuration based on magnetic resonance imaging; (b) Stress distribution at different angles of abduction indicating that the stress peak shifted towards the insertion when increasing the angle of abduction; (c–d) Finite element model of the shoulder joint at angles of abduction equal to 0° and 90°, respectively, using data obtained from computed tomography scans. Results indicated that the stress concentration increases at the insertion for increasing abduction angles (images adapted with permission from Refs. [58, 60]).

The material properties of the fibrocartilaginous regions were taken as average values between those of the tendon and bone and stress concentrations were estimated at different angles of abduction. At 0° of abduction, the principal stress peak was located at the contact region between tendon and bone. As the arm was abducted, the contact area between the supraspinatus tendon and the humeral head decreased and the stress peak shifted towards the insertion (see Fig. 1.11b). Similarly, this behavior was confirmed by a refined three-dimensional finite element model of the shoulder joint, which included rotator cuff tendons obtained from computed tomography scans (see Fig. 1.11c, left) [58]. This model also showed an increase of peak stresses on the supraspinatus tendon with the increase of the abduction angle (see Fig. 1.11d). Moreover, a difference in the stress distribution between the bursal side (*i.e.*, superficial layer) and the articular side (*i.e.*, deep layer) of the supraspinatus tendon during abduction was observed, which could cause delamination and the appearance of partial thickness tears [65].

Apart from studying the healthy soft tissue-to-bone attachement, a few models addressed the impact of damage mechanisms on the overall mechanical response of the enthesis at the organ scale [61, 63]. The potential for propagation of full-thickness tears of different sizes was studied using a three-dimensional finite element model with a refined geometry of the supraspinatus tendon-to-bone attachment including tendon, a thin layer of fibrocartilaginous region, cartilage and bone (see Fig. 1.12a) [63].

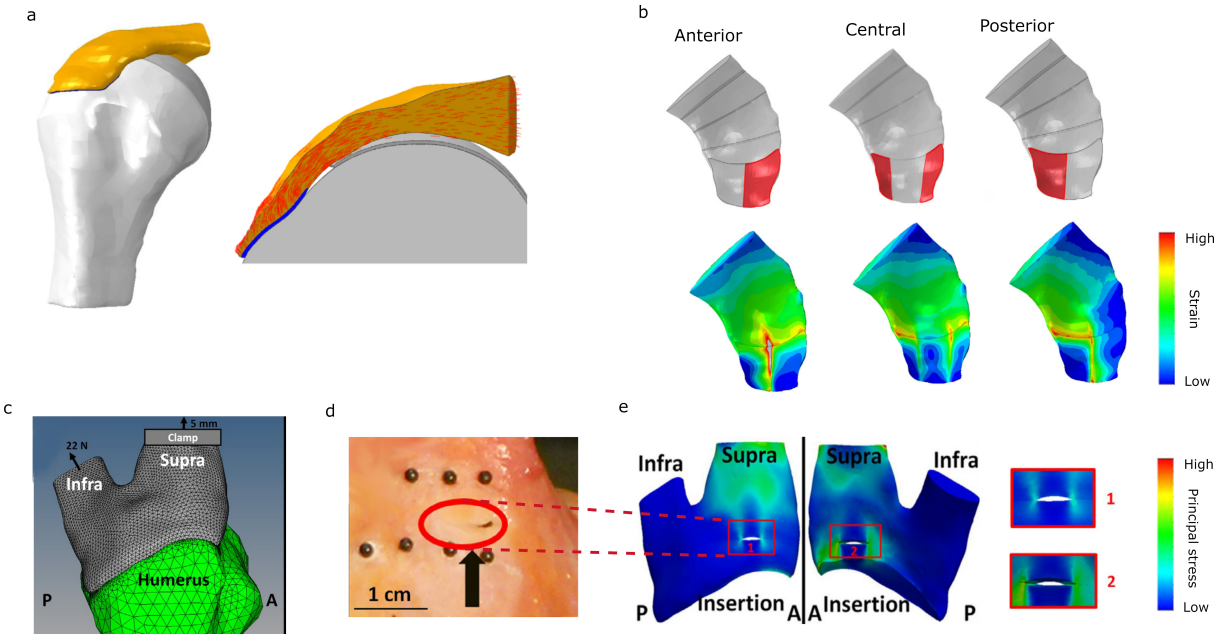

Figure 1.12 – (a) Three-dimensional finite element model of the supraspinatus tendon-to-bone attachment, where bone, cartilage, fibrocartilaginous regions, and tendon are shown in white, grey, blue, and orange, respectively; (b) Simulation of full-thickness tears in the posterior, central, and anterior regions, whereby the maximum principal strain field was computed for a 200 N load; high strains were typically located close to the tears (images adapted from Ref. [63]); (c) Finite element model of supraspinatus (Supra) and infraspinatus (Intra) tendons-to-bone attachment; the supraspinatus tendon is displaced 5 mm to induce tear propagation and a physiological 22 N load is applied on the infraspinatus tendon; (d) Tear position was selected based on experiments; (e) Stress concentration was located at the edges of the tear and near the insertion (images adapted with permission from Ref. [66]).

The tendon was modeled as a transversely isotropic hyperelastic material, whereas the cartilage and fibrocartilage were modeled as hyperelastic Neo–Hookean materials. For the latter, only the material properties of the non-mineralized fibrocartilaginous were considered [61]. Tears were introduced at the interphase between tendon and bone at different positions by decreasing their area (see Fig. 1.12b). The propagation of tears was examined by monitoring the distribution of principal strains. Regardless of its nature, the existence of a tear not only exacerbated the strain peaks in the tendon, but also shifted some of the load to the proximity of the tear. In the same spirit, a three-dimensional finite element model of supraspinatus and infraspinatus tendons-to-bone attachment was developed using subject-specific geometry and anisotropic material properties (see Fig. 1.12c) [66]. The objective was to predict full-thickness tears propagation for various combinations of tear size and location near the insertion site. The result indicated that larger tears with higher strains are most at risk for propagation, since they require lower loads to propagate.

Furthermore, some computational models also have been developed to study the impact of surgical reattachment mechanisms of soft tissue-to-bone for clinical purposes [59, 62, 67]. The objective was to evaluate the differences in stress distribution with respect to the different fixation techniques at the attachment site and how to minimize it.

1.4.3 Mesoscopic modeling of soft tissue-to-bone attachments

Mesoscopic computational models were also developed to provide a picture of the stress and strain transfer from the tendon to bone. These models intend to establish a link between the two previous families of models by taking into account certain characteristics of the interphase, such as the shape of the attachment area [45], the local tissue anisotropy [30] or the gradient in elastic properties across the interphase [68]. Using an idealized plane stress finite-element model of the tendon-to-bone attachment, along with an optimization algorithm, it was demonstrated that an optimized shape of the outward splay can minimize the principal stress associated with uniform axial loading of the tendon, resulting in a better resistance to mechanical loads (see Fig. 1.13a–b) [45]. In the same vein, the effect of collagen fibers orientation on the stress concentration at the tendon-to-bone insertion was studied using an idealized two-dimensional plane stress finite element model with a highly simplified geometry (see Fig. 1.13c). The results highlighted that the spatial distribution of the collagen fibers had a large impact on the overall stress and strain transfer at the insertion (see Fig. 1.13d–e) [30]. The effects of different stiffness gradients on the stress field were investigated by studying a tissue scale mathematical model of a rotator cuff insertion (see Fig. 1.13f). The model was associated with an axisymmetric linear elasticity problem involving three concentric cylinders, consisting in an isotropic bone core surrounded by an orthotropic cylindrical tendon plus an interphase including different transitions of mechanical properties between them. The results showed that stress concentrations at the interphase can be reduced by using a biomimetic grading of material properties between tendon and bone that was obtained through a numerical optimization of the mathematical model (see Fig. 1.13g) [68]. Interestingly, a decrease in elastic modulus to values lower than tendon and bone was identified at the interphase (see Fig. 1.13h), thereby confirming earlier experimental evidences and modeling results of the fundamental anchoring mechanisms (recall Fig. 1.10g).

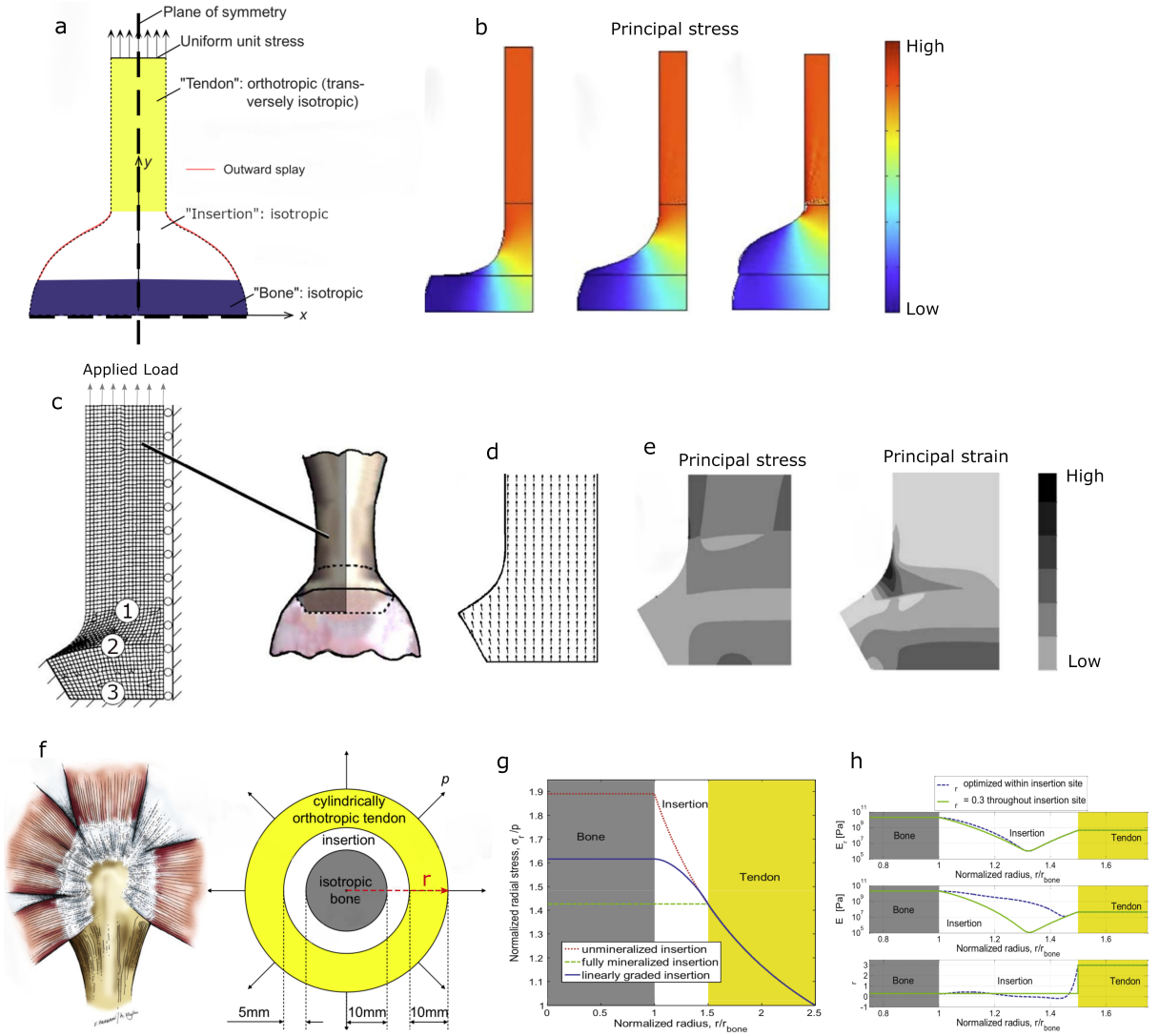

Figure 1.13 – Mesoscopic computational models of the tendon-to-bone insertion: (a) Idealized finite element model of the tendon-to-bone attachment in the shoulder; (b) Examples of selected geometries with optimized shape of the outward splay to minimize principal stress (images adapted from Ref. [45]); (c) Idealized finite element model of the tendon to bone attachment in the shoulder comprising : (1) tendon, (2) the tidemark between the non-mineralized and mineralized fibrocartilaginous regions, and (3) the bone; (d) Example of distribution of mean collagen fibers orientation based on experimental measurements; (e) Stress and strain fields evaluation, whereby peak values take place at the tendon and the outward splay of the insertion (images adapted from Ref. [30]); (f) Side view of the rotator cuff anatomy where tendons and their insertions are shown in white, muscles in red, and bones in yellow. The proposed mathematical model consider an axisymmetric geometry for the tendons and their bony insertions; (g) Variation of normalized radial stress, where material properties of bone and tendon were fixed and different transitions of mechanical properties were considered for the transition region between them; (h) Distribution of radial elastic modulus, tangential elastic modulus and Poisson ratio following numerical optimization of the mathematical model: a compliant region with a radial modulus lower than that of tendon and bone was found at the insertion site (images adapted with permission from Ref. [68]).

1.5 Current interface tissue engineering approaches

Regarding the clinical vulnerability of the tendon-to-bone attachment following an injury, there is strong interest in regenerating such transition region with the goal of achieving seamless integration of engineered musculoskeletal tissues. Within this context, the past years have seen the emergence of interface tissue engineering procedures to develop biological substitutes of these connective tissues. These procedures typically rely on the study of four key parameters to replace or repair tissue function [69]: (1) scaffold and biomaterials, (2) cells, (3) growth factors and (4) mechanical stimuli. While an important number of studies have been dedicated to the regeneration of tendons or ligaments, the regeneration of functional enthesis-like tissues has not been explored in the same depth. Enthesis tissue engineering is challenging due to the complex structural and cellular compositions of the native enthesis, which are particularly difficult to replicate.

Most biomimetic approaches developed so far are based on cells and growth factors embedded in a scaffold [70], which require a well-defined pattern of biochemical, structural and mechanical gradients to obtain a smooth transition from tendon to bone displaying the functionality of the native tissue [71, 72]. However, current enthesis-engineered procedures do not often offer efficient solutions from a mechanical viewpoint [73]. For instance, Kim et al. [74] elaborated a multilayer tendon-to-bone scaffold by combining different biomaterials that provided a gradual transition of the physical, chemical, and mechanical environment (see Fig. 1.14a). A mechanical evaluation after compressive strength of each layer showed an increase of the elastic modulus, along with a decrease of the elongation, when going from the tendon to bone (see Fig. 1.14b). However, the reported properties were particularly low compared to their native counterparts at the microscale (see Tab. 2.1).

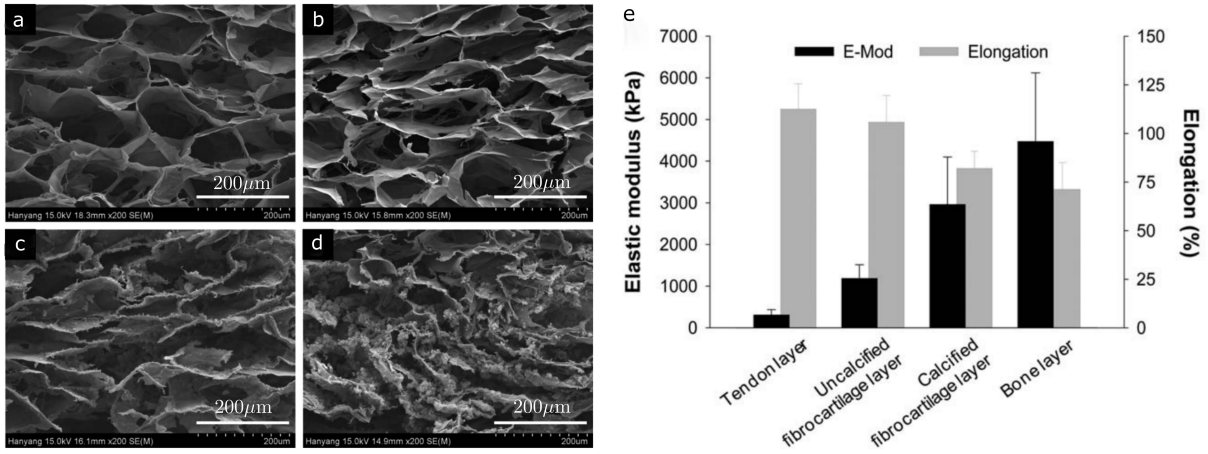

Figure 1.14 – Scanning electron micrographs of (a) the tendon layer, (b) the uncalcified fibrocartilage layer, (c) the calcified fibrocartilage layer, and (d) the bone layer; (e) mechanical properties of the different layers measured by a universal tensile machine (image adapted with permission from Ref. [74]).

A similar trend was reported in the work by Zhu et al. [75], which aimed to fabricate a hierarchically structured scaffold for tendon-to-bone repair. The proposed scaffold was composed of three regions with distinct functions (see Fig. 1.15a–c): (i) an array of

channels to guide the in-growth of cells and aligned deposition of collagen fibers, as well as the integration of the scaffold within the tendon side, (ii) a region with a gradient in mineral content to ease the stress transfer between tendon and bone, and (iii) a mineralized inverse opal region to promote the integration of the scaffold within the underlying bone.

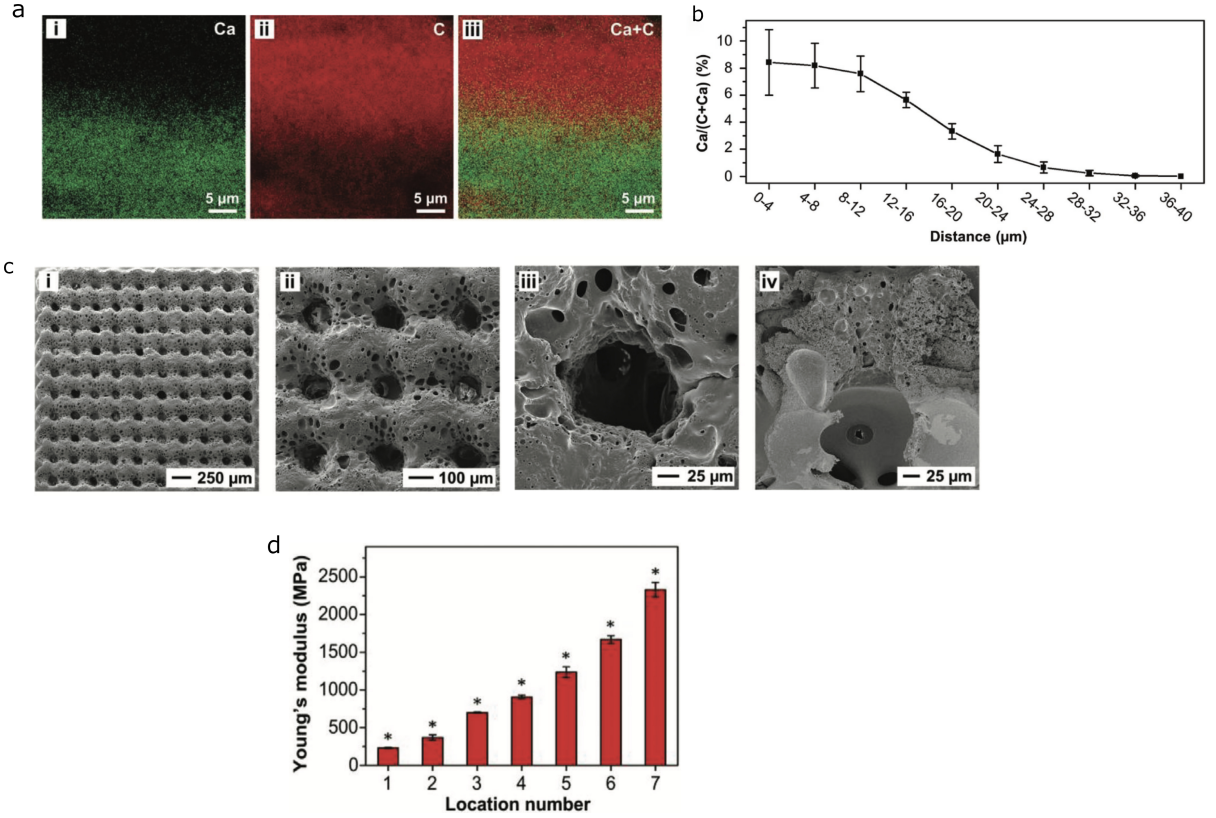

Figure 1.15 – Scaffold with graded mineral content: (a) Energy-dispersive X-ray spectroscopy mapping of the mineral content obtained from the cross-section of the scaffold with graded distributions of (i) calcium, (ii) carbon, and (iii) calcium + carbon; (b) quantification of the calcium content along the vertical direction where the longitudinal axis indicates the distance from the location with the highest mineral content; (c) Scanning electron microscopy images of the hierarchical structure of the scaffold; (d) Young's modulus obtained at seven locations along the mineral gradient from the unmineralized to the mineralized regions (image adapted with permission from Ref. [75]).

The mechanical properties of the scaffold were evaluated using atomic force miscroscopy, and the authors reported a gradual increase for the elastic modulus from the soft to the hard side (see Fig. 1.15d). However, the value for the hard side was much lower than that typically reported for cortical bone at the sub-micoscale (see Tab. 2.1).

Recently, Xie et al. [76] developed a woven scaffold that displayed a continuous mineral gradient according to the characteristics of the native tendon-to-bone. Four types of nanofiber yarns with different volume fractions of mineral were prepared by electrospinning and they were then weaved into a multiphasic mineral gradient woven scaffold (see Fig. 1.16a).

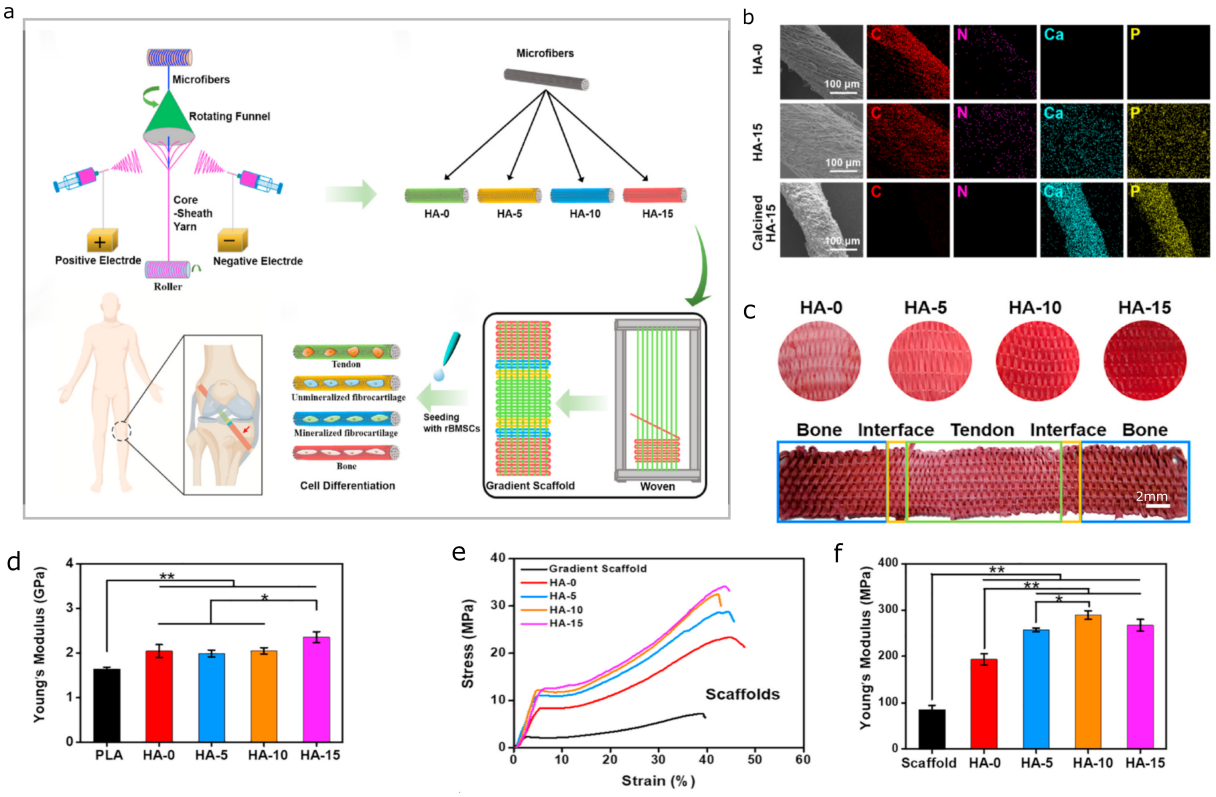

Figure 1.16 – Woven scaffold with continuous mineral gradients: (a) Schematic illustration of the preparation of the mineral gradient scaffold where the nanofiber yarns with a core-sheath structure and different contents of mineral were prepared using a custom-made electrospinning apparatus. The non-mineralized nanofiber yarn (*i.e.*, HA-0) considered as a warp and three partially mineralized nanofiber yarns (*i.e.*, HA-5, HA-10 and HA-15) as weft; (b) Scanning electron microscopy and energy-dispersive X-ray spectroscopy mapping images of microfiber bundles containing nanofiber yarns with volume fractions of mineral equal to 0%, 5% and 15%; (c) Macroscopic picture of the mineral gradient scaffold; (d) Young's modulus of microfiber bundles with different volume fractions of mineral; (e) Macroscale tensile stress-strain curves and (f) Macroscale Young's modulus of the mineral gradient scaffold at warp direction, as well as its four incorporated segments at weft direction (image adapted with permission from Ref. [76]). All mechanical properties derived by uniaxial tensile tests.

The scaffold was structurally anisotropic and shows a mineral gradient from the soft to hard region (see Fig. 1.16b–c). Its mechanical properties were specifically related to the arrangement of the yarns, whereby an increase in mechanical properties from the soft to the hard region was observed. Nevertheless, such replacement still fails to meet the mechanical requirements of the native interphase. Indeed, it has a sufficient mechanical strength to achieve the mechanical response of the tendon and uncalcified fibrocartilage regions but the mechanical response of the calcified fibrocartilage and bone were again underestimated (see Fig. 1.16e–f). The decrease of the mechanical properties of scaffold at the macroscopic level is basically due to the loose arrangement of the partially mineralized fiber yarns as they considered as warps.

Overall, to the best of our knowledge, current enthesis-engineered replacements still

fail in replicating the mismatch in mechanical properties across the interphase of their native counterparts. They may be suitable as a patch for the injured tendon-to-bone interphase for healing, repair or regeneration but are not ready yet to fully replace this transitional interphase in the long-term [71, 72, 77]. In the same vein, those replacements typically lack some features that contribute to the overall mechanical anisotropy of the native tissue. Altogether, these moderate results could be, in part, explained by the fact that most of the research focused on the biological aspects of the tissue culture (*e.g.*, cells, growth factors) at the cost of the design and mechanical characterization of the substitutes.

1.6 Synthesis

According to this review of the state-of-the-art, the variations in structural and compositional features across the soft tissue-to-bone interphase, in particular the organization of the collagen fibers, mineral grading, and interdigitation, are believed to represent the fundamental anchoring mechanisms that confer its exclusive mechanical performance to the attachement site. Meanwhile, soft tissue-to-bone attachments are frequent sites of injuries because of physical overloading, systemic diseases or tissue degeneration in the elderly. During healing and remodeling phases, gradations in structure, composition, and mechanical properties of these critical junctions are not regenerated, resulting in high rupture recurrence rates of surgical procedures. Understanding the mechanics of the enthesis is therefore essential for many different purposes including diagnosis, repair, and regeneration, as well as to develop biomimetic strategies to join highly dissimilar materials. While most experimental studies have focused on the multimodal imaging of the enthesis, thereby delivering valuable insights on its structure and composition at lower length scales, there is still a need to relate these multiscale features to the mechanics of this interfacial region. To date, several experimental approaches have been applied to estimate the mechanical properties of either tendon or bone. However, experimental measurements of the enthesis remain challenging due to difficulty in preparing and testing samples at lower scales, which display an insertion site containing both non-mineralized and mineralized tissues.

To circumvent this issue, computational and analytical models, such as multiscale modeling could help predicting the effective stiffness properties of the enthesis. Earlier modeling approaches that included elementary anchoring mechanisms of the enthesis provided a general understanding of how compositional features at the lower length scales affect the overall mechanical properties of the insertion site at the tissue scale. Furthermore, macroscopic computational models also gave a picture of the stress and strain transfer from tendon to bone. However, all these models usually neglected specific features, such as the anisotropic and viscoelastic nature of the insertion [78–80], the gradient in protein content, the different collagen types across the interphase [33, 81], and interdigitation mechanisms [27, 42]. Moreover, current computational models that aim to study the biomechanical behavior of the soft tissue-to-bone complex at the organ scale generally significantly simplified the mechanical behavior of the interphase. In particular, the finite size of the interphase, which is small compared to that of the surrounding tissues, may cause computational burden. To bridge the gap between the organ scale (targeting relevant orthopedic questions) and mesoscopic scale (suited to investigate basic anchoring

strategies), the heterogeneous interphase could be substituted by an equivalent interface with specific properties, which retains information of the microstructural features of the original interphase layer [82–84]. The effective properties of the tendon-to-bone attachement are not only valuable for modeling purposes, but also for designing and optimizing bioinspired multi-material soft-to-hard composites achieved using additive manufacturing [85]. However, to fully exploit the potential of these emerging composites, there is an unmet need in developing methods for characterizing the quality of the printing process and the mechanics of the manufactured samples. Among these, quantitative ultrasound is thought as a particularly relevant nondestructive means to probe the quality of such materials, because it relies on the use of mechanical waves and thus possesses intrinsic sensitivity to their mechanical properties. Overall, the original combination of multiscale modeling, quantitative ultrasound and additive manufacturing could open new ways for the development of characterization and repair strategies in biomechanics and tissue engineering.

Bibliography

[1] H Tempfer, C Lehner, M Grütz, R Gehwolf, and A Traweger. *Biological augmentation for tendon repair: lessons to be learned from development, disease, and tendon stem cell research*. Springer, 2020.

[2] CT Thorpe, HL Birch, PD Clegg, and HRC Screen. The role of the non-collagenous matrix in tendon function. *Int J Clin Exp Pathol*, 94(4):248–259, 2013.

[3] S Weiner and HD Wagner. The material bone: structure-mechanical function relations. *Annu Rev Mater Sci*, 28(1):271–298, 1998.

[4] J-Y Rho, L Kuhn-Spearing, and P Zioupos. Mechanical properties and the hierarchical structure of bone. *Med Eng Phys*, 20(2):92–102, 1998.

[5] P Fratzl. Collagen: structure and mechanics, an introduction. In *Collagen*, pages 1–13. Springer, 2008.

[6] M Fielder and AK Nair. Effects of hydration and mineralization on the deformation mechanisms of collagen fibrils in bone at the nanoscale. *Biomech Model Mechanobiol*, 18(1):57–68, 2019.

[7] K Misof, WJ Landis, K Klaushofer, P Fratzl, et al. Collagen from the osteogenesis imperfecta mouse model (oim) shows reduced resistance against tensile stress. *J Clin Invest*, 100(1):40–45, 1997.

[8] H S Gupta, J Seto, W Wagermaier, P Zaslansky, P Boesecke, and P Fratzl. Cooperative deformation of mineral and collagen in bone at the nanoscale. *Proc Natl Acad Sci USA*, 103(47):17741–17746, 2006.

[9] Constantinos N Maganaris and John P Paul. In vivo human tendon mechanical properties. *J Physiol*, 521(1):307–313, 1999.

[10] GA Johnson, DM Tramaglini, RE Levine, K Ohno, N-Y Choi, and S L-Y. Woo. Tensile and viscoelastic properties of human patellar tendon. *J Orthop Res*, 12(6):796–803, 1994.

[11] JY Rho, RB Ashman, and CH Turner. Young's modulus of trabecular and cortical bone material: ultrasonic and microtensile measurements. *J Biomech*, 26(2):111–119, 1993.

[12] S Bernard, J Schneider, P Varga, P Laugier, K Raum, and Q Grimal. Elasticity–density and viscoelasticity–density relationships at the tibia mid-diaphysis assessed from resonant ultrasound spectroscopy measurements. *Biomech Model Mechan*, 15(1):97–109, 2016.

[13] A Schwartz and S Thomopoulos. The role of mechanobiology in the attachment of tendon to bone. In *Structural Interfaces and Attachments in Biology*, pages 229–257. Springer, 2013.

[14] VR Sherman, W Yang, and MA Meyers. The materials science of collagen. *J Mech Behav Biomed Mater*, 52:22–50, 2015.

[15] A Gautieri, S Vesentini, A Redaelli, and MJ Buehler. Viscoelastic properties of model segments of collagen molecules. *Matrix Biol*, 31(2):141–149, 2012.

[16] A Gautieri, S Vesentini, A Redaelli, and MJ Buehler. Hierarchical structure and nanomechanics of collagen microfibrils from the atomistic scale up. *Nano Lett*, 11(2):757–766, 2011.

[17] M Fielder and AK Nair. A computational study of mechanical properties of collagen-based bio-composites. *Int Biomech*, 7(1):76–87, 2020.

[18] EM Spiesz, P Roschger, and PK Zysset. Influence of mineralization and microporosity on tissue elasticity: experimental and numerical investigation on mineralized turkey leg tendons. *Calcif Tissue Int*, 90(4):319–329, 2012.

[19] S Lees and EA Page. A study of some properties of mineralized turkey leg tendon. *Connect Tissue Res*, 28(4):263–287, 1992.

[20] M Benjamin, T Kumai, S Milz, BM Boszczyk, AA Boszczyk, and JR Ralphs. The skeletal attachment of tendons–tendon 'entheses'. *Comp Biochem Physiol A Mol Integr Physiol*, 133(4):931–945, 2002.

[21] J Buschmann and GM Bürgisser. *Biomechanics of tendons and ligaments: tissue reconstruction and regeneration*. Woodhead Publishing, 2017.

[22] J Apostolakos, TJS Durant, CR Dwyer, RP Russell, JH Weinreb, F Alaee, K Beitzel, MB McCarthy, MP Cote, and AD Mazzocca. The enthesis: a review of the tendon-to-bone insertion. *Muscles Ligaments Tendons J*, 4(3):333, 2014.

[23] M Benjamin and JR Ralphs. Fibrocartilage in tendons and ligaments—an adaptation to compressive load. *J Anat*, 193(4):481–494, 1998.

[24] HH Lu and S Thomopoulos. Functional attachment of soft tissues to bone: development, healing, and tissue engineering. *Annu Rev Biomed Eng*, 15:201–226, 2013.

[25] S Roffino, C Camy, A Foucault-Bertaud, E Lamy, M Pithioux, and A Chopard. Negative impact of disuse and unloading on tendon enthesis structure and function. *Life Sci Space Res*, 2021.

[26] E Gracey, A Burssens, I Cambré, G Schett, R Lories, I B McInnes, H Asahara, and D Elewaut. Tendon and ligament mechanical loading in the pathogenesis of inflammatory arthritis. *Nat Rev Rheumatol*, 16(4):193–207, 2020.

[27] L Rossetti, LA Kuntz, E Kunold, J Schock, KW Müller, H Grabmayr, J Stolberg-Stolberg, F Pfeiffer, SA Sieber, R Burgkart, and AR Bausch. The microstructure and micromechanics of the tendon–bone insertion. *Nat Mater*, 16(6):664, 2017.

[28] GS Jung and MJ Buehler. Multiscale modeling of muscular-skeletal systems. *Annu Rev Biomed Eng*, 19:435–457, 2017.

[29] P Fratzl and R Weinkamer. Nature's hierarchical materials. *Prog Mater Sci*, 52(8):1263–1334, 2007.

[30] S Thomopoulos, JP Marquez, B Weinberger, V Birman, and GM Genin. Collagen fiber orientation at the tendon to bone insertion and its influence on stress concentrations. *J Biomech*, 39(10):1842–1851, 2006.

[31] D Qu, SD Subramony, AL Boskey, N Pleshko, SB Doty, and HH Lu. Compositional mapping of the mature anterior cruciate ligament-to-bone insertion. *J Orthop Res*, 35(11):2513–2523, 2017.

[32] J Sartori and H Stark. Tracking tendon fibers to their insertion–a 3d analysis of the achilles tendon enthesis in mice. *Acta Biomater*, 120:146–155, 2021.

[33] S Thomopoulos, GR Williams, JA Gimbel, M Favata, and LJ Soslowsky. Variation of biomechanical, structural, and compositional properties along the tendon to bone insertion site. *J Orthop Res*, 21(3):413–419, 2003.

[34] JP Spalazzi, AL Boskey, N Pleshko, and HH Lu. Quantitative mapping of matrix content and distribution across the ligament-to-bone insertion. *PLoS One*, 8(9):e74349, 2013.

[35] L Kuntz. *The enthesis: nature's solution to a hard-soft interface*. PhD thesis, Technische Universität München, 2018.

[36] S Tiburtius, S Schrof, F Molnár, P Varga, F Peyrin, Q Grimal, K Raum, and A Gerisch. On the elastic properties of mineralized turkey leg tendon tissue: multiscale model and experiment. *Biomech Model Mechanobiol*, 13(5):1003–1023, 2014.

[37] AK Nair, A Gautieri, and MJ Buehler. Role of intrafibrillar collagen mineralization in defining the compressive properties of nascent bone. *Biomacromolecules*, 15(7):2494–2500, 2014.

[38] P Fratzl, HS Gupta, EP Paschalis, and P Roschger. Structure and mechanical quality of the collagen–mineral nano-composite in bone. *J Mater Chem*, 14(14):2115–2123, 2004.

[39] GM Genin, A Kent, V Birman, B Wopenka, JD Pasteris, PJ Marquez, and S Thomopoulos. Functional grading of mineral and collagen in the attachment of tendon to bone. *Biophys J*, 97(4):976–985, 2009.

[40] B Wopenka, A Kent, JD Pasteris, Y Yoon, and S Thomopoulos. The tendon-to-bone transition of the rotator cuff: a preliminary raman spectroscopic study documenting the gradual mineralization across the insertion in rat tissue samples. *Appl Spectrosc*, 62(12):1285–1294, 2008.

[41] J Gao and K Messner. Quantitative comparison of soft tissue-bone interface at chondral ligament insertions in the rabbit knee joint. *J Anat*, 188 (Pt 2):367–73, 1996.

[42] Y Hu, V Birman, A Deymier-Black, AG Schwartz, S Thomopoulos, and GM Genin. Stochastic interdigitation as a toughening mechanism at the interface between tendon and bone. *Biophys J*, 108(2):431–437, 2015.

[43] L Zhao, A Thambyah, and ND Broom. A multi-scale structural study of the porcine anterior cruciate ligament tibial enthesis. *J Anat*, 224(6):624–633, 2014.

[44] AC Abraham and TLH Donahue. From meniscus to bone: a quantitative evaluation of structure and function of the human meniscal attachments. *Acta Biomater*, 9(5):6322–6329, 2013.

[45] Y Liu, V Birman, C Chen, S Thomopoulos, and GM Genin. Mechanisms of bimaterial attachment at the interface of tendon to bone. *J Eng Mater Technol*, 133(1):011006, 2011.

[46] DL Butler, N Juncosa-Melvin, GP Boivin, MT Galloway, JT Shearn, C Gooch, and H Awad. Functional tissue engineering for tendon repair: A multidisciplinary strategy using mesenchymal stem cells, bioscaffolds, and mechanical stimulation. *J Orthop Res*, 26(1):1–9, 2008.

[47] M Benjamin, H Toumi, D Suzuki, S Redman, P Emery, and D McGonagle. Microdamage and altered vascularity at the enthesis–bone interface provides an anatomic explanation for bone involvement in the hla–b27–associated spondylarthritides and allied disorders. *Arthritis Rheum*, 56(1):224–233, 2007.

[48] A Rufai, JR Ralphs, and M Benjamin. Structure and histopathology of the insertional region of the human achilles tendon. *J Orthop Res*, 13(4):585–593, 1995.

[49] KA Derwin, LM Galatz, A Ratcliffe, and S Thomopoulos. Enthesis repair: Challenges and opportunities for effective tendon-to-bone healing. *J Bone Joint Surg Am*, 100(16):e109–e109, 2018.

[50] JZ Paxton, K Baar, and LM Grover. Current progress in enthesis repair: strategies for interfacial tissue engineering. *Orthopedic Muscul Sys S*, 1, 2012.

[51] M Benjamin, H Toumi, JR Ralphs, G Bydder, TM Best, and S Milz. Where tendons and ligaments meet bone: attachment sites ('entheses') in relation to exercise and/or mechanical load. *J Anat*, 208(4):471–490, 2006.

[52] G Schett, RJ Lories, M-A D'Agostino, D Elewaut, B Kirkham, ER Soriano, and D McGonagle. Enthesitis: from pathophysiology to treatment. *Nat Rev Rheumatol*, 13(12):731, 2017.

[53] KN Hauch, ML Oyen, GM Odegard, and TL Haut Donahue. Nanoindentation of the insertional zones of human meniscal attachments into underlying bone. *J Mech Behav Biomed Mater*, 2(4):339–347, 2009.

[54] J Gao, T Räsänen, J Persliden, and K Messner. The morphology of ligament insertions after failure at low strain velocity: an evaluation of ligament entheses in the rabbit knee. *J Anat*, 189(Pt 1):127, 1996.

[55] S Thomopoulos, GR Williams, and LJ Soslowsky. Tendon to bone healing: differences in biomechanical, structural, and compositional properties due to a range of activity levels. *J Biomech Eng*, 125(1):106–113, 2003.

[56] Y Liu, S Thomopoulos, C Chen, V Birman, MJ Buehler, and GM Genin. Modelling the mechanics of partially mineralized collagen fibrils, fibres and tissue. *J R Soc Interface*, 11(92):20130835, 2014.

[57] F Saadat, V Birman, S Thomopoulos, and GM Genin. Effective elastic properties of a composite containing multiple types of anisotropic ellipsoidal inclusions, with application to the attachment of tendon to bone. *J Mech Phys Solids*, 82:367–377, 2015.

[58] A Inoue, E Chosa, K Goto, and N Tajima. Nonlinear stress analysis of the supraspinatus tendon using three-dimensional finite element analysis. *Knee Surg Sports Traumatol Arthrosc*, 21(5):1151–1157, 2013.

[59] T Funakoshi, N Suenaga, H Sano, N Oizumi, and A Minami. In vitro and finite element analysis of a novel rotator cuff fixation technique. *J Shoulder Elbow Surg*, 17(6):986–992, 2008.

[60] I Wakabayashi, E Itoi, H Sano, Y Shibuya, R Sashi, H Minagawa, and M Kobayashi. Mechanical environment of the supraspinatus tendon: a two-dimensional finite element model analysis. *J Shoulder Elbow Surg*, 12(6):612–617, 2003.

[61] H Sano, I Wakabayashi, and E Itoi. Stress distribution in the supraspinatus tendon with partial-thickness tears: an analysis using two-dimensional finite element model. *J Shoulder Elbow Surg*, 15(1):100–105, 2006.

[62] M Mantovani, A Pellegrini, P Garofalo, and P Baudi. A 3D finite element model for geometrical and mechanical comparison of different supraspinatus repair techniques. *J Shoulder Elbow Surg*, 25(4):557–563, 2016.

[63] C Quental, J Folgado, J Monteiro, and M Sarmento. Full-thickness tears of the supraspinatus tendon: A three-dimensional finite element analysis. *J Biomech*, 49(16):3962–3970, 2016.

[64] E Pena, B Calvo, M A. Martinez, and M Doblare. A three-dimensional finite element analysis of the combined behavior of ligaments and menisci in the healthy human knee joint. *J Biomech*, 39(9):1686–1701, 2006.

[65] H-C Gwak, C-W Kim, J-H Kim, H-J Choo, S-Y Sagong, and J Shin. Delaminated rotator cuff tear: extension of delamination and cuff integrity after arthroscopic rotator cuff repair. *J Shoulder Elbow Surg*, 24(5):719–726, 2015.

[66] RM Miller, J Thunes, V Musahl, S Maiti, and RE Debski. Effects of tear size and location on predictions of supraspinatus tear propagation. *J Biomech*, 68:51–57, 2018.

[67] H Sano, M Tokunaga, M Noguchi, T Inawashiro, T Irie, H Abe, and AT Yokobori Jr. Tight medial knot tying may increase retearing risk after transosseous equivalent repair of rotator cuff tendon. *Biomed Mater Eng*, 28(3):267–277, 2017.

[68] YX Liu, S Thomopoulos, V Birman, J-S Li, and GM Genin. Bi-material attachment through a compliant interfacial system at the tendon-to-bone insertion site. *Mech Mater*, 44:83–92, 2012.

[69] SF Tellado, ER Balmayor, and M Van Griensven. Strategies to engineer tendon/ligament-to-bone interface: Biomaterials, cells and growth factors. *Adv Drug Deliv Rev*, 94:126–140, 2015.

[70] I Calejo, R Costa-Almeida, RL Reis, and ME Gomes. Enthesis tissue engineering: Biological requirements meet at the interface. *Tissue Eng Part B Rev*, 25(4):330–356, 2019.

[71] T Lei, T Zhang, W Ju, X Chen, BC Heng, W Shen, and Z Yin. Biomimetic strategies for tendon/ligament-to-bone interface regeneration. *Bioact Mater*, 6(8):2491–2510, 2021.

[72] C Zhu, J Qiu, S Thomopoulos, and Y Xia. Augmenting tendon-to-bone repair with functionally graded scaffolds. *Adv Healthc Mater*, page 2002269, 2021.

[73] AJ Boys, MC McCorry, S Rodeo, LJ Bonassar, and LA Estroff. Next generation tissue engineering of orthopedic soft tissue-to-bone interfaces. *MRS Commun*, 7(3):289–308, 2017.

[74] BS Kim, EJ Kim, JS Choi, JH Jeong, CH Jo, and YW Cho. Human collagen-based multilayer scaffolds for tendon-to-bone interface tissue engineering. *J Biomed Mater Res A*, 11(102):4044–4054, 2014.

[75] C Zhu, S Pongkitwitoon, J Qiu, S Thomopoulos, and Y Xia. Design and fabrication of a hierarchically structured scaffold for tendon-to-bone repair. *Adv Mater*, 30(16):1707306, 2018.

[76] X Xie, J Cai, Y Yao, Y Chen, J Wu, X Mo, et al. A woven scaffold with continuous mineral gradients for tendon-to-bone tissue engineering. *Compos B Eng*, 212:108679, 2021.

[77] B Shiroud Heidari, R Ruan, EM De-Juan-Pardo, M Zheng, and B Doyle. Biofabrication and signaling strategies for tendon/ligament interfacial tissue engineering. *ACS Biomater Sci Eng*, 7(2):383–399, 2021.

[78] A Tits, E Plougonven, S Blouin, MA Hartmann, J-F Kaux, P Drion, J Fernandez, GH van Lenthe, and D Ruffoni. Local anisotropy in mineralized fibrocartilage and subchondral bone beneath the tendon-bone interface. *Sci Rep*, 11(1):1–17, 2021.

[79] S Kuznetsov, M Pankow, K Peters, and H-YS Huang. Strain state dependent anisotropic viscoelasticity of tendon-to-bone insertion. *Math Biosci*, 308:1–7, 2019.

[80] M Milazzo, A David, GS Jung, S Danti, and MJ Buehler. Molecular origin of viscoelasticity in mineralized collagen fibrils. *Biomater Sci*, 9(9):3390–3400, 2021.

[81] AD Waggett, JR Ralphs, APL Kwan, D Woodnutt, and M Benjamin. Characterization of collagens and proteoglycans at the insertion of the human Achilles tendon. *Matrix Biol*, 16(8):457–470, 1998.

[82] M Brun, S Guenneau, AB Movchan, and D Bigoni. Dynamics of structural interfaces: filtering and focussing effects for elastic waves. *J Mech Phys Solids*, 58(9):1212–1224, 2010.

[83] M Touboul, B Lombard, and C Bellis. Time-domain simulation of wave propagation across resonant meta-interfaces. *J Comput Phys*, 414:109474, 2020.

[84] M Touboul, K Pham, A Maurel, J-J Marigo, B Lombard, and C Bellis. Effective resonant model and simulations in the time-domain of wave scattering from a periodic row of highly-contrasted inclusions. *J Elast*, 142(1):53–82, 2020.

[85] MJ Mirzaali, AH de la Nava, D Gunashekar, M Nouri-Goushki, RPE Veeger, Q Grossman, L Angeloni, MK Ghatkesar, LE Fratila-Apachitei, D Ruffoni, EL Doubrovski, and AA Zadpoor. Mechanics of bioinspired functionally graded soft-hard composites made by multi-material 3D printing. *Compos Struct*, page 111867, 2020.

Chapter 2. Assessing the effective elastic properties of the tendon-to-bone insertion: a multiscale modeling approach

The work presented in this chapter is issued from the following publication:
A Aghaei, N Bochud, G Rosi, and S Naili, Assessing the effective elastic properties of the tendon-to-bone insertion: a multiscale modeling approach, *Biomech Model Mechanobiol*, 20(2): 433 – 448, 2021.

Contents

Abstract

The interphase joining tendon to bone plays the crucial role of integrating soft to hard tissues, by effectively transferring stresses across two tissues displaying a mismatch in mechanical properties of nearly two orders of magnitude. The outstanding mechanical properties of this interphase are attributed to its complex hierarchical structure, especially by means of competing gradients in mineral content and collagen fibers organization at different length scales. The goal of this study is to develop a multiscale model to describe how the tendon-to-bone insertion derives its overall mechanical behavior. To this end, the effective anisotropic stiffness tensor of the interphase is predicted by modeling its elastic response at different scales, spanning from the nanostructural to the mesostructural levels, using continuum micromechanics methods. The results obtained at a lower scale serve as inputs for the modeling at a higher scale. The obtained predictions are in good agreement with stochastic finite element simulations and experimental trends reported in literature. Such model has implication for the design of bioinspired bi-materials that display the functionally graded properties of the tendon-to-bone insertion.

Keyword: Tendon-to-bone insertion, Homogenization, Continuum micromechanics, Biological interphase, Functionally graded material, Partially mineralized tissue.

2.1 Introduction

The interaction between soft and hard tissues is essential to ensure good mobility to the musculoskeletal system. Specifically, the integration between tendon (or ligament) and bone occurs through a particular tissue interphase called *enthesis*, which derives from the ancient Greek word referring to the insertion. According to their musculoskeletal site of insertion, entheses can be characterized as fibrous or fibrocartilaginous [1]. Fibrous (or indirect) insertions are usually found where tendons and ligaments attach to the shaft of long bones, such as the insertion of the deltoid tendon into the humerus or the tibial insertion of the medial collateral ligament. Fibrocartilaginous (or direct) insertions are more common and present at the bony attachments of the rotator cuff, the anterior cruciate ligament and the Achilles tendons. Fibrocartilaginous insertions are generally divided into four distinct regions with different compositions, functions, and biomechanical properties: (1) the tendon, which consists of aligned type I collagen fibers with a small amount of non-collagenous proteins (NCPs), including proteoglycans and the remaining volume filled with water [2]; (2) a non-mineralized fibrocartilaginous region, which is an avascular zone consisting of unmineralized types I, II and III collagen fibers and proteoglycan aggrecan [3]; (3) a mineralized fibrocartilaginous region, which is mostly characterized by partially mineralized type II collagen fibers, the proteoglycan aggrecan being produced by fibrocartilage cells or fibrochondrocytes between bundles of collagen fibers [4]; and (4) the bone, which is a composite material that mainly consists of highly mineralized type I collagen [5].

Although these different tissue regions are compositionally distinct, they are structurally continuous. Moreover, it is acknowledged that the mechanical environment of the enthesis is complex and heterogeneous, as it is subject to tensile, compressive and shear forces [6], in order to ensure an effective transfer of the mechanical stresses across the

two surroundings tissues, which show a mismatch in mechanical properties of nearly two orders of magnitude. Three main features contribute to the mechanical effectiveness of the enthesis: (1) its geometry is characterized by a shallow attachment angle and an optimized shape of the outward splay, which improves its resistance to mechanical loads [7]; (2) the interdigitation of the bone within the tendon, described as a wave-like structure, allows a gain in toughness, as well as a better distribution of stresses on the fraction of tissue implied in this mechanism [8]; and (3) a compositional and structural gradient, through a gradual increase in mineral content together with a corresponding reorganization of the collagen fibers from the tendon to the bone [9]. The combination of these multiscale factors is hypothesized to lead to an intermediate zone more compliant than either tendon or bone, thus ensuring an effective distribution of mechanical stresses, which allows reducing the risk of rupture [10, 11].

Musculoskeletal injuries involving tendon rupture typically require surgical reattachment back to bone. Such operations exhibit a high rate of failure because the enthesis rarely regenerates and does not recover its mechanical properties. This clinical burden is mainly due to the lack of understanding of the healthy attachment, as well as of the damaging process that may occur at this interphase [12]. To date, studies on the tendon-to-bone insertion have mainly focused on the rehabilitation methods to be implemented after a tendon operation, as well as on the histology of the enthesis [13]. The targeted parameters generally included compositional and structural features at lower length scales (*e.g.*, collagen types, organization and morphology of collagen fibers, degree of mineralization), but seldom the mechanical properties at the tissue scale. Indeed, the direct mechanical measurement of the tendon-to-bone insertion has been shown to be very complicated, particularly because of its heterogeneity and small dimensions (typically a few μm to some mm according to the insertion site) [10, 14]. The excellent mechanical properties of the enthesis are attributed to its complex hierarchical structure. Nonetheless, understanding how this hierarchy and the resulting mechanical properties at the different scales affect its overall mechanical behavior and allow such an effective stress transfer across this interphase represents a considerable challenge. To address this issue, tools such as multiscale modeling could help predicting the effective stiffness properties of the enthesis at the tissue level, as well as studying the individual impact of lower-scale features on its overall mechanical behavior at higher scales.

Regardless of the considered medium –tendon, enthesis or bone–, all these regions substantially have a similar hierarchical collagen-based structure starting with collagen molecules at the nanoscale up to a pattern of collagen fibers surrounded by an extracellular matrix at higher scales [15]. Several analytical and computational models have been proposed to infer the mechanical properties of bone at different scales, in particular using homogenization methods [16–19]. In the same way, a few studies have been conducted on the hierarchical modeling of (mineralized) tendon [20, 21]. However, little information concerning the multiscale modeling of the tendon-to-bone insertion is available in the literature. Biomechanical models were initially proposed by considering the collagen-mineral interactions and the collagen fiber architecture at the microscale. In a pioneering study, Genin *et al.* [22] estimated the stiffness of partially mineralized fibers by randomly distributing minerals among unmineralized cylindrical collagen fibrils using Monte Carlo simulations, which subsequently allowed determining the isotropic mechanical properties of the partially mineralized tissue at the macroscale. Later, the same group introduced a progressive stiffening model for collagen, by accounting for different sequences of mineral

accumulation across spatial hierarchy levels spanning from the fibril to the tissue level, to estimate the mechanical properties of partially mineralized collagen tissue [23]. In a subsequent study, they presented an estimate for composites containing multiple classes of aligned ellipsoidal inclusions with a relatively high volume fraction, which demonstrated its potential application to the graded tissue interphase at the tendon-to-bone attachment [24]. More recently, the micromechanical behavior of tendon-to-bone structures was studied and compared with a composite beam-bending model [25]. The beam was modeled as a three-phase composite in series, in which the modulus of the transitional graded interphase was defined as a linear extrapolation between those of the mineralized and unmineralized regions. All these models provided a general understanding on the mechanical properties of the insertion site (*i.e.*, average Young modulus) at different structural levels. However, to the best of our knowledge, these models only partially accounted for the anisotropic nature of the interphase at the different scales, and the transition between different hierarchies from the nanoscale to the mesoscale was not achieved. Moreover, the impact of the individual nanoscale properties on the effective stiffness tensor at the mesoscale was not addressed so far.

To face these current limitations, this study aims at developing a hierarchical model to predict the effective anisotropic stiffness tensor of the tendon-to-bone insertion by modeling its elastic response at different scales spanning from the nano- to the mesostructural levels. To this end, a continuum micromechanics approach was proposed by distinguishing six homogenization steps at four different scales. First, we derived the effective stiffness properties of the enthesis at the mesoscale by accounting for gradients in mineral content and collagen fibers organization across the interphase at lower scales. Second, we carried out a parametric study to evaluate the impact of the mechanical properties of each nanoscale component on the overall mechanical behavior of the insertion site. Third, based on the knowledge of the mechanical properties of the two surroundings tissues at the mesoscale, an optimization procedure was solved to identify the nanoscale properties that yield the best agreement between the model predictions and ultrasonic data reported in the literature. Numerical results show that the effective mechanical properties predicted by our multiscale model are in good agreement with earlier modeling approaches and experimentally observed trends. Moreover, our model is straighforward and could be readily extended to account for damage characteristics of the interphase as a footprint of clinical burden.

The paper is structured as follows: Sec. 2.2 recalls the fundamentals of micromechanics-based models and introduces the proposed multiscale modeling of the enthesis. The model parameters, *i.e.*, the mechanical properties, volume fractions and gradients of the tendon-to-bone insertion's components, are then described in Sec. 2.3. Finally, the numerical results are presented in Sec. 2.4 and discussed in the light of the literature in Sec. 2.5.

2.2 Methods

In this section, a multiscale model of the tendon-to-bone insertion based on a hierarchical modeling approach that consists of successive homogenization steps from the nanostructural to the mesostructural levels is proposed. This multiscale model relies on several hypotheses: (1) whereas mineral grading can occur at any length scale, it was incorporated here at the nanoscale [26]; (2) the gradient in collagen fibers organization

occured at the microscale [22]; (3) type I collagen was assumed to be the main organic component across the interphase; and (4) the mechanical properties of the elementary nanoscale components (collagen, hydroxyapatite (HA), water and NCPs), which were used as input data in our model, were all assumed to have a linear elastic and isotropic behavior.

2.2.1 Fundamentals of micromechanics-based models

Continuum micromechanics allows estimating the effective stiffness properties of heterogeneous materials [27], which can generally be derived by solving the matrix-inclusion problem according to Eshelby [28]. A basic concept of continuum micromechanics consists in selecting a representative volume element (RVE) in the structure. Based on the separation-of-scales requirement, the characteristic length ℓ of this RVE must be considerably larger than the dimension of the heterogeneities d within the RVE and implicitly smaller than the characteristic length of the structure $\mathcal{L}$, so that $d \ll \ell \ll \mathcal{L}$. Useful information concerns volume fractions and elastic properties of phases, the existence of one connected matrix phase in which one or several inclusion phases with different shapes are embedded or the disordered arrangement of all phases. Hence, the homogenized stiffness tensor of such RVE, $\mathbb{C}_{\text{hom}}$, can be stated as in [29]

$$\mathbb{C}_{\text{hom}} = \sum_{r=1}^{n} f_r \mathbb{c}_r : \left[\mathbb{I} + \mathbb{P}_r^0 : (\mathbb{c}_r - \mathbb{C}^0)\right]^{-1} : \left\{\sum_{s=1}^{n} f_s \left[\mathbb{I} + \mathbb{P}_s^0 : (\mathbb{c}_s - \mathbb{C}^0)\right]^{-1}\right\}^{-1} \tag{2.1}$$

where : denotes the double contracted product of two tensors, n is the number of phases in the RVEs, f_r denotes the volume fraction of the phase r, $\mathbb{I}$ is the fourth-order identity tensor, $\mathbb{c}_r$ is the stiffness tensor of phase r, $\mathbb{C}^0$ is the stiffness tensor of the matrix phase, and $\mathbb{P}^0$ is the so-called Hill tensor of phase r embedded in the matrix phase, whose form depends on the shape of the inclusion and on the stiffness tensor of the surrounding matrix $\mathbb{C}^0$. The Hill tensor can be related to the Eshelby tensor as $\mathbb{P}^0 = \mathbb{S}^0_{\text{Esh}} : (\mathbb{C}^0)^{-1}$. The components of the Hill tensors for the different inclusion shapes considered in this study are provided in A.1.

Several approaches for determining $\mathbb{C}^0$ have been proposed in the literature. Among these, two methods are particularly relevant to our context. First, the Mori-Tanaka scheme can be applied when the inclusion phase consists of small particles surrounded by a continuous homogeneous matrix [30]. In such a case, the matrix phase can be directly identified as the actual matrix phase (*i.e*, $\mathbb{C}^0 = \mathbb{C}_{\text{matrix}}$). Second, when no matrix phase can be clearly identified, it is convenient to apply the self-consistent scheme [31]. The underlying hypothesis of this second method consists in estimating the homogenized properties of the effective medium by locating each inhomogeneity in the homogeneous effective medium (*i.e*, $\mathbb{C}^0 = \mathbb{C}_{\text{hom}}$).

2.2.2 Multiscale modeling of the tendon-to-bone insertion

According to earlier studies applied to partially mineralized tissues, such as bone [17, 32, 33] and mineralized tendon [20], we hierarchically modeled here the mechanical behavior of the tendon-to-bone insertion by considering four relevant hierarchical levels compound of six homogenization steps (see Fig. 3.1), and by assuming gradients in

mineral content and collagen fibers organization across the interphase between the two surroundings tissues [22, 23]. Across the enthesis, mineral crystals replace the water by filling the gap zones between collagen thereafter spreading through the fibrils surface [34]. Extrapolating this consideration to our modeling approach, the fibril array was considered as a hydrated collagen fibril at the nanoscale (i) without mineral particles in the tendon region, (ii) with a functional grading of mineral across the insertion, and (iii) as a partially mineralized collagen fibril in the bone region. The gradient of mineralization was introduced in the model by means of a normalized mineral volume fraction, $\phi(x)$, defined as the ratio of the overall mineral volume fraction $f_{\text{mineral}}(x)$ at a normalized position along the insertion, x, to the overall volume fraction of mineral at the bone level, $f^{\text{bone}}_{\text{mineral}}$, so that $\phi(x) = f_{\text{mineral}}(x)/f^{\text{bone}}_{\text{mineral}}$. The normalized position x across the interphase was thus $x = 0$ at the end of the tendon (*i.e.*, $\phi(x) = 0$) and $x = 1$ at the beginning of the bone (*i.e.*, $\phi(x) = 1$), so that $\phi(x) \approx x$. Moreover, the gradient in collagen fibers organization was accounted for by considering the angular deviation of the collagen fibers distribution at a normalized position x along the insertion [22]. At each scale, the homogenized stiffness tensor of the enthesis, $\mathbb{C}_{\text{hom}}(x)$, was therefore related to a precise description of the geometric and mechanical properties of each of the subscales at any normalized position x across the interphase.

A. Nanostructural level

At the nanostructural level, collagen molecules are attached to each other by crosslinks, which transfer the stresses from one collagen molecule to another [35]. Water initially fills the spaces between collagen molecules. During the mineralization process, mineral crystals are nucleated in the gap zones, thus progressively replacing the water. They then further grow into the overlap zones during development and may be distributed throughout the collagen molecules to form a partially mineralized collagen fibril [36]. To mimic this physiological process, three homogenization steps were used to model the enthesis at the nanostructural level: (1) combining collagen together with water and NCPs, (2) combining HA crystals with water and NCPs, and (3) combining the collagen composite from step 1 with the HA foam from step 2 to form a partially mineralized collagen fibril.

Step 1: wet collagen composite

The wet collagen composite was modeled as a contiguous cross-linked collagen molecules matrix with holes hosting water and NCPs, where the holes were considered as cylindrical inclusions [33, 37]. Based on the assumption that a continuum approach can be applied at the nanostructural level, the Mori-Tanaka scheme was used to estimate the effective stiffness tensor of the composite, $\mathbb{C}_{\text{wc}}$, at this scale as

$$\begin{aligned}\mathbb{C}_{\text{wc}} = (1-f_{\text{wp}})\mathbb{c}_{\text{col}} + f_{\text{wp}}\mathbb{c}_{\text{wp}} : \left[\mathbb{I} + \mathbb{P}^{\text{col}}_{\text{wp}}(\mathbb{c}_{\text{wp}} - \mathbb{c}_{\text{col}})\right]^{-1} \\ : \left\{(1-f_{\text{wp}})\mathbb{I} + f_{\text{wp}}\left[\mathbb{I} + \mathbb{P}^{\text{col}}_{\text{wp}} : (\mathbb{c}_{\text{wp}} - \mathbb{c}_{\text{col}})\right]^{-1}\right\}^{-1},\end{aligned} \tag{2.2}$$

where subscripts "wc", "col" and "wp" are referred to the wet collagen composite, collagen, and water-protein mixture, respectively.

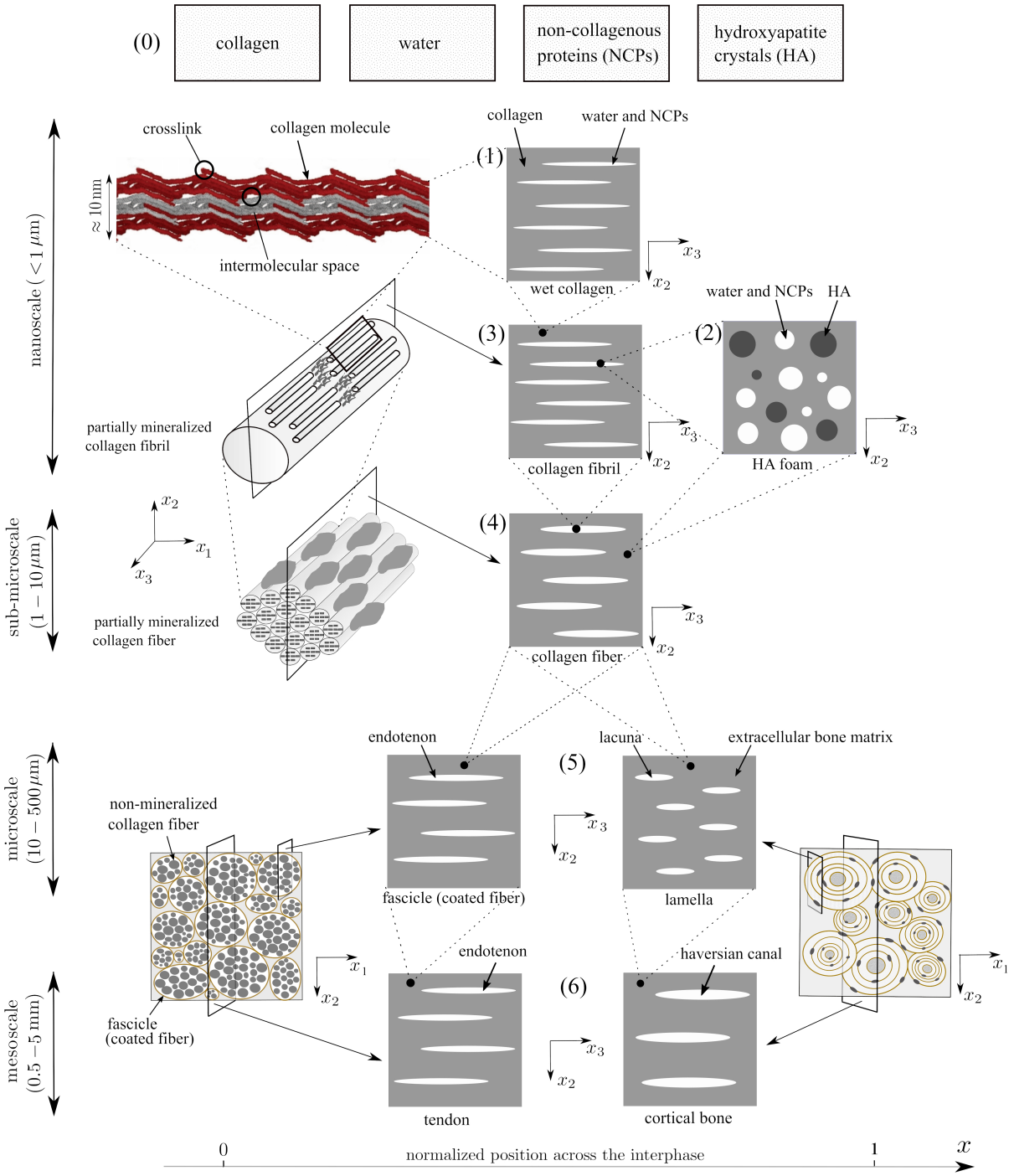

Figure 2.1 – Successive steps of our multiscale modeling approach: (0) elementary nanoscale components; (1) wet collagen composite formed by a collagen molecules matrix containing water and NCPs-filled pores (image adapted from [35]); (2) HA foam formed by HA crystals containing water and NCPs-filled pores; (3) partially mineralized collagen fibril made up from wet collagen and intrafibrillar HA foam; (4) partially mineralized collagen fiber formed by partially mineralized collagen fibrils and extrafibrillar HA foam; (5) lamella and unit fascicle built up from a partially mineralized collagen fiber matrix holding lacunae cavities and *endotenon*, respectively; and (6) cortical bone and tendon formed by a continuous bone matrix (extravascular bone) and a bundle of parallel fascicles matrix containing haversian canals and *endotenon*, respectively.

Step 2: hydroxyapatite foam

At the scale of a few hundred nanometers, HA crystals were assumed to be interpenetrated by intercrystalline space filled with water and NCPs [19]. Since no well-defined matrix phase can be identified at this scale, it results convenient to apply the self-consistent scheme to estimate the effective stiffness tensor of the HA foam, $\mathbb{C}_{\mathrm{Hw}}(x)$, which depends upon the mineral gradient across the insertion. Both the mineral phase and the water-protein mixture were here assumed to be spherical in shape with a linear elastic and isotropic behavior. Hence,

$$\begin{aligned}\mathbb{C}_{\mathrm{Hw}}(x) = &\sum_{r=1}^{2} f_r(x)\mathbb{c}_r : \left[\mathbb{I} + \mathbb{P}_r^0 : (\mathbb{c}_r - \mathbb{C}_{\mathrm{Hw}}(x))\right]^{-1} \\ &: \left\{\sum_{s=1}^{2} f_s(x)\left[\mathbb{I} + \mathbb{P}_s^0 : (\mathbb{c}_s - \mathbb{C}_{\mathrm{Hw}}(x))\right]^{-1}\right\}^{-1},\end{aligned} \tag{2.3}$$

with $r, s \in [\mathrm{HA}, \mathrm{wp}]$. The subscript "Hw" denotes the HA foam. The detailed calculation of the stiffness coefficients is provided in B.1.

Step 3: partially mineralized collagen fibril

The collagen fibril structure was modeled as a composite consisting of a wet collagen composite matrix reinforced with aligned needle-shaped interfibrillar minerals, which were assumed to be distributed along the main axis of the collagen fibril [38]. Again, the classical Mori-Tanaka method was applied to determine the effective stiffness tensor of a partially mineralized collagen fibril, $\mathbb{C}_{\mathrm{fib}}(x)$, as

$$\begin{aligned}\mathbb{C}_{\mathrm{fib}}(x) = &(1 - f_{\mathrm{Hw}})\mathbb{c}_{\mathrm{wc}} + f_{\mathrm{Hw}}\mathbb{c}_{\mathrm{Hw}}(x) : \left[\mathbb{I} + \mathbb{P}_{\mathrm{Hw}}^{\mathrm{wc}} : (\mathbb{c}_{\mathrm{Hw}}(x) - \mathbb{c}_{\mathrm{wc}})\right]^{-1} \\ &: \left\{(1 - f_{\mathrm{Hw}})\mathbb{I} + f_{\mathrm{Hw}}\left[\mathbb{I} + \mathbb{P}_{\mathrm{Hw}}^{\mathrm{wc}} : (\mathbb{c}_{\mathrm{Hw}}(x) - \mathbb{c}_{\mathrm{wc}})\right]^{-1}\right\}^{-1},\end{aligned} \tag{2.4}$$

where $\mathbb{c}_{\mathrm{wc}}$ and $\mathbb{c}_{\mathrm{Hw}}(x)$ are the effective stiffness tensors resulting from the application of steps 1 and 2, respectively.

B. Sub-microstructural level – partially mineralized collagen fiber

At the scale of several micrometers (step 4), randomly dispersed extrafibrillar minerals with different sizes and shapes strongly adhere to the outer parts of the collagen fibrils [34]. During the mineralization, these extrafibrillar minerals are located around the fibril surface and then start growing along the main fibril axis, therefore forming a sort of reinforcing structure around the fibril. Consequently, a partially mineralized collagen fiber can be modeled as an extrafibrillar HA foam matrix pervaded by a cylindrical collagen fibril inclusion. In this way, the effective stiffness tensor of the partially mineralized collagen fiber, $\mathbb{C}_{\mathrm{fbr}}(x)$, can be estimated using the Mori-Tanaka scheme as

$$\begin{aligned}\mathbb{C}_{\mathrm{fbr}}(x) = &(1 - f_{\mathrm{fib}})\mathbb{c}_{\mathrm{Hw}}(x) + f_{\mathrm{fib}}\mathbb{c}_{\mathrm{fib}}(x) : \left[\mathbb{I} + \mathbb{P}_{\mathrm{fib}}^{\mathrm{Hw}}(x) : (\mathbb{c}_{\mathrm{fib}}(x) - \mathbb{c}_{\mathrm{Hw}}(x))\right]^{-1} \\ &: \left\{(1 - f_{\mathrm{fib}})\mathbb{I} + f_{\mathrm{fib}}\left[\mathbb{I} + \mathbb{P}_{\mathrm{fib}}^{\mathrm{Hw}}(x) : (\mathbb{c}_{\mathrm{fib}}(x) - \mathbb{c}_{\mathrm{Hw}}(x))\right]^{-1}\right\}^{-1},\end{aligned} \tag{2.5}$$

where $\mathbb{c}_{\mathrm{Hw}}(x)$ and $\mathbb{c}_{\mathrm{fib}}(x)$ are the effective stiffness tensors resulting from the application of steps 2 and 3, respectively.

Moving from the tendon to bone, apart from the gradual increase in mineral content (already accounted for in step 2), the insertion site also shows a gradual decrease in the organization of collagen fibers. At the tendon level, collagen fibers are aligned and parallelly-oriented along the x_3-axis. These then start bending and intercrossing along the insertion, and become less organized near the bone [9]. Consequently, the effective stiffness tensor of an individual partially mineralized collagen fiber, $\mathbb{C}_{\text{fbr}}(x)$, can be related to the microstructural level (*i.e.*, fiber bundle or pattern) by averaging over the fibers orientation at each position x of the insertion. Hence,

$$\bar{\mathbb{C}}_{\text{fbr}}(x) = \int_S \left(\mathbb{R}(\boldsymbol{n})\mathbb{C}_{\text{fbr}}(x)\mathbb{R}^{\text{T}}(\boldsymbol{n})\right) p(\boldsymbol{n}, s(x)) dS \tag{2.6}$$

where the superscript T denotes the transpose operator; $p(\boldsymbol{n}, s(x))$ is an axisymmetric and spherical probability density function for finding a fiber whose axis is parallel to the unit vector $\boldsymbol{n}$, with $s(x)$ the angular deviation at a position x with respect to the mean fiber direction x_3; $\mathbb{R}(\boldsymbol{n})$ rotates a tensor from this coordinate system into the global coordinate system; and $\boldsymbol{n}$ includes all directions over the unit sphere S [22]. Note that the resulting stiffness tensor of a partially mineralized fibers pattern, $\bar{\mathbb{C}}_{\text{fbr}}(x)$, retains the symmetry class of that of an individual collagen fiber, but results more compliant along the x_3-direction.

C. Microstructural level – partially mineralized fibers pattern

At the microstructural level (step 5), the structure and composition of tendon and bone are no longer identical, and therefore lead to a different approach for modeling a partially mineralized fibers pattern. At the tendon level, a bundle of aligned collagen fibers forms a unit fascicle, which represents the basic unit of a tendon. A thin connective tissue called *endotenon* surrounds each collagen fiber and binds the fibers together [39]. Since the self-consistent and Mori-Tanaka methods are limited to an inclusion associated with a low volume fraction, the interactions between neighboring fibers cannot be neglected anymore [24]. To circumvent this issue, the so-called "inverse Mori-Tanaka" scheme was applied here simply by inverting the matrix and inclusion phases [17]. In this regard, by considering the connected bundle of collagen fibers as a matrix and *endotenon* as a cylindrical inclusion, the effective stiffness tensor of a unit fascicle can be estimated. At the bone level, a lamella containing cavities filled with osteocytes called *lacunae* is enclosed by the continuous bone matrix holding a bundle of preferentially oriented collagen fibers. In addition, the main axis of *lacunae* was assumed to be oriented along the longitudinal direction of a lamella [40]. Therefore, similarly to the tendon region, the effective stiffness tensor of a lamella can be estimated by considering the *lacuna* as a cylindrical inclusion coated with a continuous bone matrix. Hence, the effective stiffness tensor of a partially mineralized fibers pattern at the microstructural level, $\mathbb{C}_{\text{mic}}(x)$, was estimated by considering $\mathbb{C}^0 \equiv \mathbb{C}_{\text{end}} \equiv \mathbb{C}_{\text{lac}} \equiv \mathbb{C}_{\text{wp}}$, so that

$$\begin{aligned}\mathbb{C}_{\text{mic}}(x) = f_{\text{fbr}}(x)\bar{\mathbb{c}}_{\text{fbr}}(x) + (1 - f_{\text{fbr}}(x))\mathbb{c}_{\text{wp}} : \left[\mathbb{I} + \bar{\mathbb{P}}^{\text{fbr}}_{\text{wp}}(x) : (\mathbb{c}_{\text{wp}} - \bar{\mathbb{c}}_{\text{fbr}}(x))\right]^{-1} \\ : \left\{ f_{\text{fbr}}(x)\mathbb{I} + (1 - f_{\text{fbr}}(x)) \left[\mathbb{I} + \bar{\mathbb{P}}^{\text{fbr}}_{\text{wp}}(x) : (\mathbb{c}_{\text{wp}} - \bar{\mathbb{c}}_{\text{fbr}}(x))\right]^{-1} \right\}^{-1}.\end{aligned} \tag{2.7}$$

In this way, the main difference between tendon and bone at this scale was accounted for by considering a linearly varying volume fraction across the interphase (*i.e.*, $1 - f_{\text{fbr}}(x)$

with $x \in \{0, 1\}$) for their corresponding inclusion (*endotenon* for $x = 0$ or *lacuna* for $x = 1$).

D. Mesostructural level – partially mineralized tissue

Similarly to the microstructural level, a different modeling approach was used for the tendon and bone to account for their differences in structure and composition at the mesostructural level (step 6). On the one hand, a bundle of parallel fascicles with an interfascicular matrix (*endotenon*) forms the tendon [41]. Considering a bundle of parallel fascicles as a matrix and *endotenon* as a cylindrical inclusion, the effective stiffness tensor of tendon can be estimated. On the other hand, cortical bone hosts cylindrical pores called haversian canals, which contain the bone's nerve and blood supplies being embedded into the osteonal lamella matrix (extravascular bone) [37]. The effective stiffness tensor of cortical bone can thus be estimated by considering haversian canals as a cylindrical inclusion coated with a continuous bone matrix.

As in step 5, the effective stiffness tensors of a partially mineralized tissue, $\mathbb{C}_{\text{meso}}(x)$, can be estimated by considering $\mathbb{C}^0 \equiv \mathbb{C}_{\text{end}} \equiv \mathbb{C}_{\text{hav}} \equiv \mathbb{C}_{\text{wp}}$,

$$\begin{aligned}\mathbb{C}_{\text{meso}}(x) = f_{\text{mic}}(x)\mathbb{c}_{\text{mic}}(x) + (1 - f_{\text{mic}}(x))\mathbb{c}_{\text{wp}} : \left[\mathbb{I} + \mathbb{P}^{\text{mic}}_{\text{wp}}(x) : (\mathbb{c}_{\text{wp}} - \mathbb{c}_{\text{mic}}(x))\right]^{-1} \\ : \left\{ f_{\text{mic}}(x)\mathbb{I} + (1 - f_{\text{mic}}(x)) \left[\mathbb{I} + \mathbb{P}^{\text{mic}}_{\text{wp}}(x) : (\mathbb{c}_{\text{wp}} - \mathbb{c}_{\text{mic}}(x))\right]^{-1} \right\}^{-1}.\end{aligned} \tag{2.8}$$

Again, the variation across the interphase was here driven by the a linearly varying volume fraction, $1 - f_{\text{mic}}(x)$, for their corresponding inclusion only.

2.3 Model parameters

Like for any other hierarchical material, the knowledge of the mechanical properties and volume fractions of the tendon-to-bone insertion's elementary components, along with the competing gradients in collagen fibers organization and mineral content, are required to assess its overall mechanical behavior. A broad range of values for the mechanical properties (*e.g.*, Young's modulus E and Poisson's ratio ν) of the nanoscale components has been reported in the literature, based on experimental testing facilities or molecular dynamics (MD) simulations.

Earlier theoretical studies provided values of around 2 GPa for the Young's modulus of collagen, but recent MD simulations reported higher values for the Young's modulus of a single collagen molecule, ranging from 7 to 19 GPa [33]. The Poisson's ratio of collagen has typically been chosen equal to 0.28 to deliver a Poisson's ratio of around 0.35 for the collagen-water composite (recall step 1) [17, 18]. Furthermore, HA minerals were typically assumed to have a linear elastic and isotropic behavior, with a Young's modulus ranging from 63 to 165 GPa, and a Poisson's ratio of around 0.23 [33]. To date, little is known about the mechanical properties of NCPs. Nevertheless, water-NCPs composite has generally been assumed to have isotropic properties with a Young's modulus ranging from 1.3 MPa to 0.7 GPa, and a Poisson's ratio ranging from 0.4999 to 0.45, thus encompassing typical values for water (*i.e.*, a nearly incompressible material with a bulk modulus of 2.2 GPa) and soft polymers [17]. The mechanical properties range of each nanoscale component used as input values in our multiscale model is summarized in Tab. 2.1.

Material	Young's modulus, E (GPa)	Poisson's ratio, ν (–)
Collagen molecules	$1.2 - 9.6$	$0.23 - 0.33$
HA minerals	$63 - 165$	$0.18 - 0.28$
Water-NCPs composite	$0.0013 - 0.7$	$0.4999 - 0.45$

Table 2.1 – Mechanical properties range of the nanoscale components used for modeling the mesoscale effective stiffness tensor of the tendon-to-bone insertion in this study.

A volume fraction of mineral $f_{\mathrm{HA}}(x)$ varying linearly from 0 to 65% was considered (see Fig. 2.2a), based on the experimentally observed mineral concentration gradient at the tendon-to-bone insertion [26]. Moreover, the collagen fibers distribution $s(x)$ was chosen according to experimental data [42], which reported that the angular deviation values for the tendon-to-bone insertion reached a peak in the non-mineralized fibrocartilaginous region and varied little beyond it (see Fig. 2.2b)

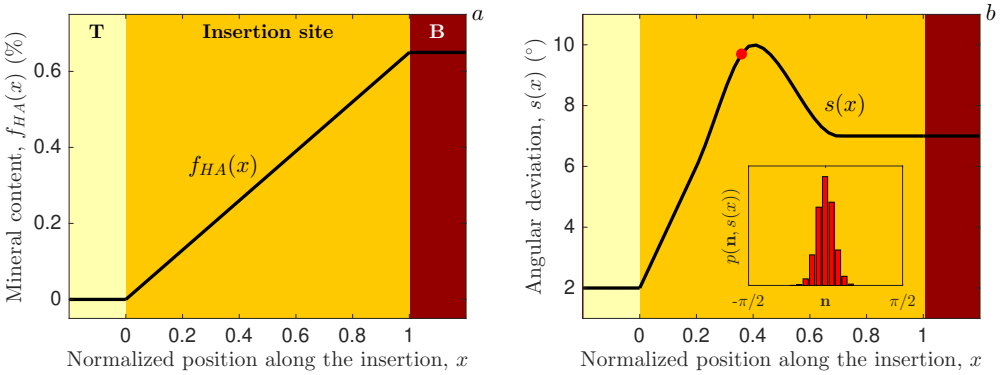

Figure 2.2 – Spatially varying properties of the interphase from the tendon (T) to bone (B) based on competing gradients in (a) mineral content and (b) collagen fibers organization. The insert displays the distribution of collagen fibers near the region of largest fibers disorganization (red dot). These trends are based upon data reported in Refs. [22, 24].

The volume fractions of each phase, along with the different homogenization methods applied at each step, are summarized in Tab. 2.2. At the nanostructural level, the volume fraction for the water-protein mixture, f_{wp}, has been taken according to [17]. At the nanostructural and sub-microstructural levels, we used the values for a mineralization inside and outside the fibrilsas a function of the total mineral content, *i.e.*, f_{Hw} and $1 - f_{\mathrm{fib}}$, following the work of Nikolov and Raabe [17]. In this way, these concurrent variations lead to an overall volume fraction of mineral varying from 0 to 52% between tendon and bone at the mesoscale, which is in good agreement with values reported in the literature [16, 17]. Furthermore, to account for the difference in structure and composition of the tendon and bone at the micro- and mesostructural levels, volume fractions that vary linearly with respect to the normalized position x across the interphase, *i.e.*, $1 - f_{\mathrm{fbr}}(x)$ and $1 - f_{\mathrm{mic}}(x)$, have been considered for their respective inclusions at each of these two levels [16, 20].

Hierarchical levels	Steps	Homogenization schemes	Phases		Volume fractions (%)	Relations
Nano	1	Mori-Tanaka	Inclusion Matrix	Water-NCPs Collagen	$f_{\text{wp}} = 35$	Eq. (2.2)
	2	Self-consistent	Phase 1 Phase 2	Water-NCPs HA	$f_{\text{HA}}(x) = 65x$	Eq. (2.3)
	3	Mori-Tanaka	Inclusion Matrix	Intra-HA foam Wet collagen	$f_{\text{Hw}} = 43$	Eq. (2.4)
Sub-micro	4	Mori-Tanaka	Inclusion Matrix	Collagen fibril Extra-HA foam	$f_{\text{fib}} = 73$	Eq. (2.5)
Micro	5	Inverse Mori-Tanaka	Inclusion Matrix	Endotenon – Lacunae Collagen fiber	$f_{\text{fbr}}(x) = 8x + 90$	Eqs. (2.6–2.7)
Meso	6	Inverse Mori-Tanaka	Inclusion Matrix	Endotenon – Haversian Fascicle – Lamella	$f_{\text{mic}}(x) = 8x + 90$	Eq. (2.8)

Table 2.2 – Volume fractions of each phase along with the different homogenization schemes applied at each step of the multiscale modeling.

2.4 Numerical results

The effective stiffness properties of the tendon-to-bone insertion from the nanostructural to the mesostructural levels were estimated using the six homogenization steps described in Fig. 3.1. Three analyses were conducted to rate the performance of the proposed multiscale model. First, several characteristics of the effective stiffness coefficients obtained at the mesostructural level (step 6) were assessed. Second, a parametric study was performed to evaluate the impact of the input parameters on the resulting effective stiffness tensor. Third, an optimization procedure was proposed to identify the model parameters that yielded the best agreement between modeled and measured effective stiffness tensors.

2.4.1 Effective stiffness tensor at the mesostructural level, $\mathbb{C}_{\text{meso}}(x)$

Figure 2.3 depicts the effective stiffness coefficients of the tendon-to-bone insertion obtained at the mesostructural level, together with the Voigt-Reuss bounds calculated according to [43], using the average mechanical properties from Tab. 2.1. Note that Voigt notation is adopted to define the coefficients of the fourth-order stiffness tensor and that the x_3-axis denotes the longitudinal axis, which is aligned with the mean direction of the collagen fibers distribution (recall step 4 of Fig. 3.1).

First, it is worth pointing out that our model led to a transversely isotropic elastic behavior for the insertion site at the mesoscale, where the stiffness coefficients along the fibers (*i.e.*, $C_{33}(x)$ and $C_{44}(x)$) were consistently larger than those normal to the fibers (*i.e.*, $C_{11}(x)$ and $C_{66}(x)$), thus retaining the symmetry class of the two surroundings tissues. Recalling that the main constituent properties at the nanoscale were all considered as linear elastic and isotropic, the anisotropy at the different scales was initially triggered by the consideration of geometric features (*i.e.*, the shape of the inclusion) in step 1. Second, the derived effective stiffness tensors at the extremities of the insertion, *i.e.*, $\mathbb{C}_{\text{meso}}(x = 0)$ and $\mathbb{C}_{\text{meso}}(x = 1)$ from Eq. (2.8), were in good agreement with experimental values reported in the literature for the Achilles tendon [44, 45] and cortical bone,

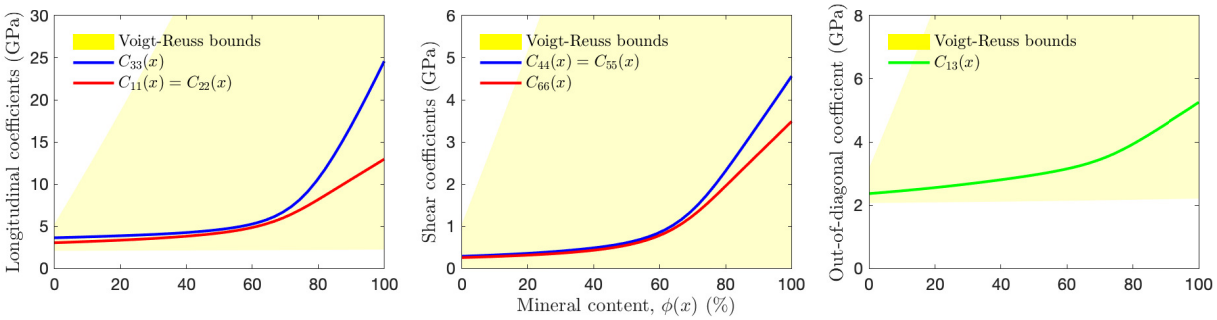

Figure 2.3 – Effective stiffness coefficients (in Voigt notation) of the tendon-to-bone insertion obtained at the mesostructural level (continuous lines), along with the Voigt-Reuss bounds (yellow area), using the average mechanical properties from Tab. 2.1.

measured at the tibia mid-diaphysis [46] and femoral diaphysis [47]. Third, the derived stiffness profile across the interphase was nonlinear, displaying a smooth stiffness increase in the non-mineralized fibrocartilaginous region ($\phi(x) < 50\%$) followed by a sudden rise in stiffness in the mineralized fibrocartilaginous region ($\phi(x) > 50\%$). The fact that an increase in mineral accumulation within collagen fibers can provide significant stiffening of the enthesis, but only for concentration of minerals above a certain percolation threshold (*i.e.*, $\phi(x) \approx 60\%$), corroborates earlier results and confirms that our model can account for effects of nonuniform mineral accumulation [22]. Finally, it should be noted that the obtained stiffness coefficients all fall within the lower and upper limits defined by the Voigt-Reuss bounds.

2.4.2 Parametric study

The predicted output values of our multiscale model strongly depend on the mechanical properties of the nanoscale components, which showed a rather high dispersion among different studies (recall Tab. 2.1). We thus performed a parametric study to assess the impact of these input parameters on the values of the resulting effective stiffness tensor at the mesostructural level. The obtained bounds for each of the five independent stiffness coefficients are depicted in Fig. 2.4. As can be observed, the mechanical properties of the water-NCPs composite inclusion were mostly responsible for relative variations of the shear coefficients (*i.e.*, $C_{44}(x)$ and $C_{66}(x)$) in the low-mineralized region, whereas they barely affected the longitudinal coefficients. The mechanical properties of the collagen molecules matrix significantly affected all stiffness coefficients over the entire tendon-to-bone transition. As expected, the mechanical properties of HA minerals were only responsible for variations of the stiffness coefficients in the highly mineralized region.

2.4.3 Identification procedure

To further investigate the sensitivity of the effective stiffness tensor across the interphase, which, in turn, reflects the ability of our model to predict experimentally observed data, we proposed an optimization procedure to identify the model parameters $\boldsymbol{\theta}$ (*i.e.*, the six nanoscale properties from Tab. 2.1) that yielded the best agreement between modeled and measured effective stiffness tensors at the mesostructural scale, denoted by

$\mathbb{C}_{\text{meso}}(\boldsymbol{\theta}; x)$ and $\mathbb{C}^{\text{exp}}(x)$, respectively. Since experimental data for the interphase at the tissue scale are not available in the literature, the optimization was conducted on data from the two surrounding tissues only, *i.e.*, $\mathbb{C}^{\text{exp}}(x = 0)$ and $\mathbb{C}^{\text{exp}}(x = 1)$, which are summarized in Tab. 2.3.

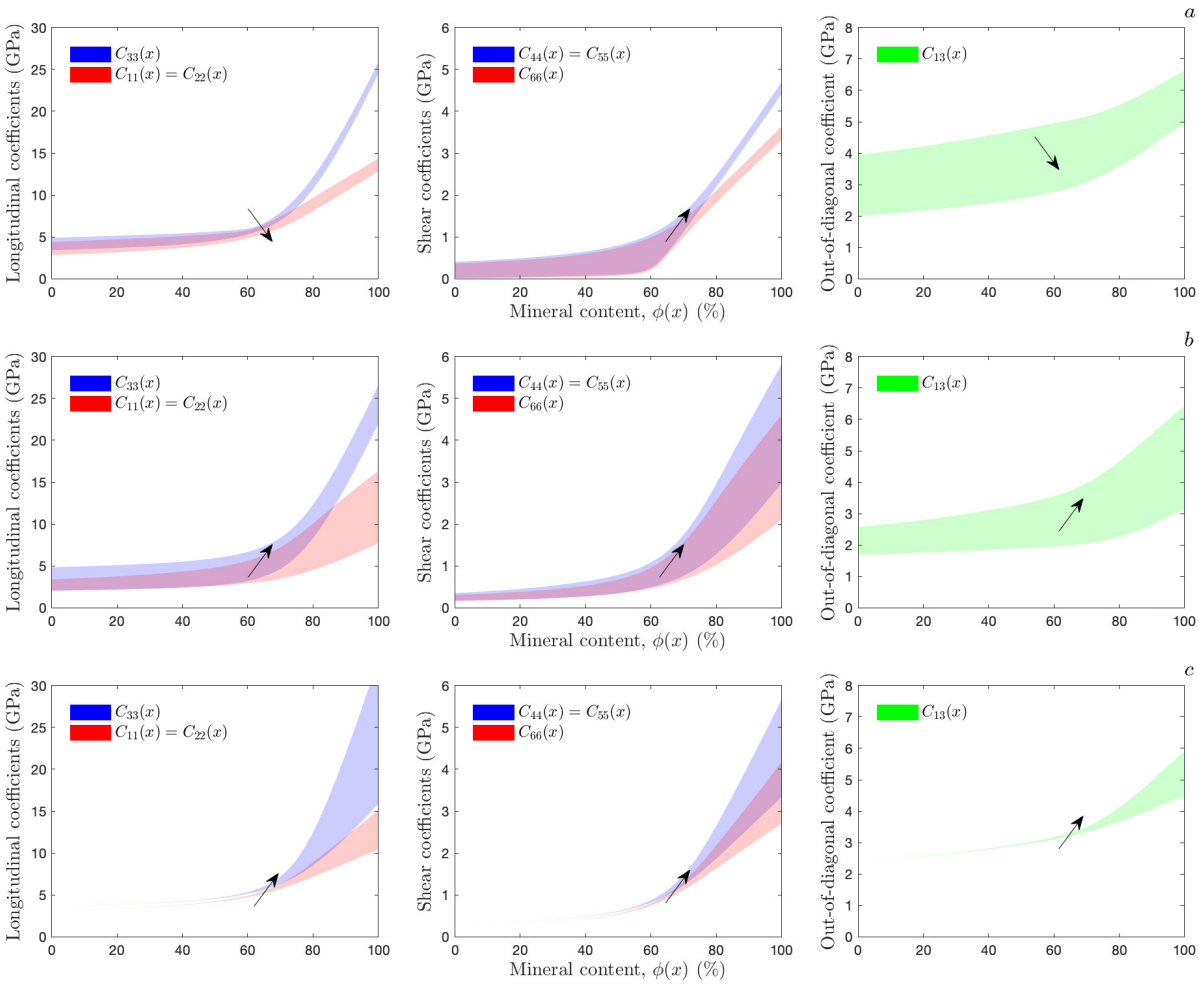

Figure 2.4 – Stiffness coefficients bounds of the tendon-to-bone insertion at the mesostructural level for a variation of the mechanical properties of the nanoscale components: (a) water-NCPs composite; (b) collagen molecules; and (c) HA minerals. Black arrows indicate the resulting trends in stiffness with respect to increasing nanoscale properties.

Material	Position	Stiffness tensor $\mathbb{C}^{\text{exp}}(x)$					Reference
		C_{11}^{exp}	C_{33}^{exp}	C_{13}^{exp}	C_{55}^{exp}	C_{66}^{exp}	
Tendon	$x = 0$	3.08	4.51	3.10	0.04	0.02	[44]
Cortical bone	$x = 1$	14.79	26.64	6.31	5.52	3.65	[46]

Table 2.3 – Reference stiffness coefficients (in GPa) for tendon and bone at the mesostructural scale.

Formally, the optimal model parameters $\hat{\boldsymbol{\theta}}$ result from the minimization of an objective

function $F(\boldsymbol{\theta})$ in a least-squares sense as,

$$\hat{\boldsymbol{\theta}} \;=\; \arg\min_{\boldsymbol{\theta}\in\Theta} F(\boldsymbol{\theta}) \quad \text{with} \quad F(\boldsymbol{\theta}) \;=\; \frac{1}{N}\sum_{n=1}^{N}\left(\frac{C_n^{\exp}-C_n(\boldsymbol{\theta})}{C_n^{\exp}}\right)^2, \tag{2.9}$$

where $\boldsymbol{C}^{\exp}$ and $\boldsymbol{C}(\boldsymbol{\theta})$ are vectors that contain the measured and modeled stiffness coefficients, respectively, N is the number of stiffness coefficients, and Θ denotes the bounds of the model parameters $\boldsymbol{\theta}$, which were taken according to Tab. 2.1. Genetic algorithms were applied to solve Eq. (4.22) owing to their ability in finding a near global solution for non-convex multidimensional objective functions, without the need of an accurate initial guess for the model parameters [48]. For this set of experimental data, the identification procedure delivered the following estimates for the model parameters, $\hat{\boldsymbol{\theta}} = [0.0153\ 0.4991\ 7.9\ 0.29\ 125.5\ 0.23]$, which pairwise correspond to the Young's moduli (GPa) and Poisson's ratios of the water-NCPs composite, collagen molecules and HA minerals, respectively. Figure 2.5 depicts the optimal matching between the modeled and measured effective stiffness tensors at the mesostructural scale. An excellent agreement can be observed between the modeled and measured longitudinal stiffness coefficients, with relative errors that are less than 5%. However, the agreement for the shear and out-of-diagonal stiffness coefficients was moderate for the tendon region, thus indicating that our model lacks some mechanical features that may account for a stronger anisotropy in the transverse direction.

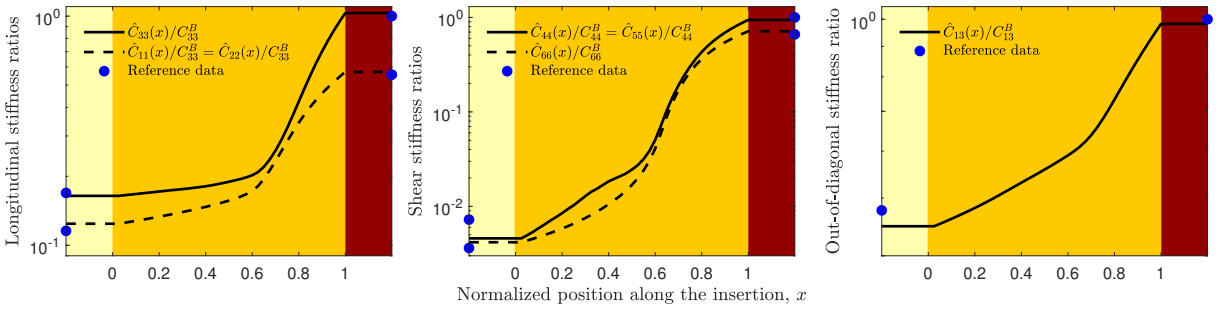

Figure 2.5 – Optimal matching between the modeled and measured effective stiffness tensors at the mesostructural scale. Results were normalized with respect to the stiffness coefficients of bone (Tab. 2.3).

2.5 Discussion

The tendon-to-bone insertion plays a crucial role in the musculoskeletal system, achieving an effective transfer of mechanical stresses across two tissues displaying a substantial gap in mechanical properties of nearly two orders of magnitude. An accurate modeling accounting for the mutiscale and composite nature of this interphase is essential to deepen our understanding of complex biological interphases and has potential applications both for clinical purposes and for the development of biomimetic strategies in engineering. In this study, we proposed a multiscale model spanning four different hierarchical levels, from the nano- to the mesoscale, connected based on homogeneization procedures. Starting from the mechanical properties of the elementary nanoscale components, this

multiscale modeling strategy allowed deriving the effective stiffness tensor of the enthesis at the mesoscale. Since an analytical formulation was used at every step, the computational cost of modeling was very low.

The main findings from this study were as follows: (1) the effective stiffness tensor across the interphase was found to be transversely isotropic at the mesostructural level (Fig. 2.3), thus retaining the symmetry class of the two surrounding tissues (*i.e.*, tendon and bone); (2) the mechanical properties of the elementary nanoscale components were shown to impact the stiffness coefficients of the interphase at the mesoscale (Fig. 2.4), and were subsequently optimized, by solving an inverse identification procedure, to match available ultrasonic data for the two surroundings tissues (Fig. 2.5); and (3) our modeling results for the interphase were in qualitative agreement with stochastic finite-element estimates [22, 23] and reported experimental values for the insertional zones of human meniscal attachments into underlying bone [49], thus supporting the hypothesis that the tendon-to-bone insertion can be seen as a continuous functionally graded material.

Indeed, in accordance with these earlier models, our results indicated that the competing gradients in mineral concentration (at the nanoscale) and collagen fibers organization (at the microscale) are important factors in determining the effective mechanical behavior of the tendon-to-bone insertion at the mesoscale. On the one hand, the linear increase in mineral content caused a stiffening of the interphase that became significant beyond a certain percolation threshold. On the other hand, the decreasing collagen fiber organization across the interphase led to a reduced tissue stiffness along the main fibers direction. The existence of a region that is more compliant than either tendon or bone (continuous line in Fig. 2.6) was the result of these competing gradients. Moreover, it can be shown that the dominant factors driving the width and depth of this compliant region are the onset of mineralization and the angular deviation from the main collagen fibers direction (dashed line in Fig. 2.6).

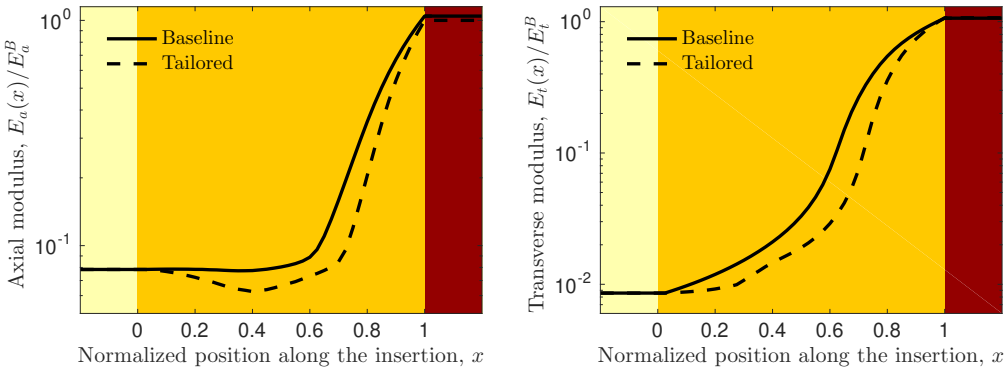

Figure 2.6 – Mesostructural level estimates of the longitudinal elastic moduli. The baseline (continuous line) displays the axial and transverse moduli obtained from the optimal stiffness coefficients depicted in Fig. 2.5, whereas the tailored case (dashed line) was obtained by delaying the onset of mineralization (to $x \approx 0.2$) and reducing the collagen fibers organization (angular deviation increased to 5°).

Despite these promising results, mismatch observed between the model predictions and experimental data (Fig. 2.5) could rise from simplifying hypotheses that were adopted at different stages of the modeling. First, the transition between different hierarchies from

the nanoscale to the mesoscale is continuous rather than discrete in real biological structures [33]. However, a limited number of length scales was accounted for in the modeling, by assuming the existence of a RVE at each scale and each normalized position across the interphase, in order to fulfill the separation-of-scales requirements (*i.e.*, features at a previous scale are much smaller than those at the next scale). This is not necessarily correct for the tendon-to-bone insertion because the features at a previous scale may not be strictly infinitesimal with respect to a larger scale. Although several continuum micromechanics approaches have been used to model partially mineralized tissues with a certain success [16–20, 29, 50], their use at the nanoscale has sparked important discussions among the homogenization community and is open to debate [51]. For instance, the nano-sized dimensions of mineralized tissue components as well as their spatial arrangements and interactions motivated alternative approaches based on discrete atomistic simulations, specifically molecular dynamics [52]. A second challenging issue was the selection of the mechanical properties of the nanoscale components, *i.e.*, Young's moduli and Poisson's ratios. In this study, all nanoscale components (*i.e.*, water-NCPs composite, collagen molecules and HA crystals) were assumed to have a linear elastic and isotropic behavior. Wide range of values for these nanoscale properties have been reported in the literature (recall Tab. 2.1) and different choices of such properties may lead to very different results. For instance, atomistic modeling approach of collagen molecules revealed that collagen may have a highly nonlinear viscoelastic behavior [53]. Likewise, the geometry and properties of HA crystals are still subject to debate. This includes the shape of the mineral particles, which have been considered both as needles [38, 54] or plates [5, 34]. Some evidences also shown that HA crystals may be oriented randomly around the mineralized collagen fibrils [55], that their size can change during the mineralization from the tendon to bone [56], or that their mechanical properties are anisotropic [57]. Third, only a few studies differentiated between intra- and extrafibrillar mineral volume fractions. Indeed, the mineralization of fibril arrays, in particular the ratio between extra- and intrafibrillar mineral content, has sparked important discussions. Some authors mentioned a high intrafibrillar mineral content [58, 59], whereas some others evidenced that the mineral content is mainly located in the extrafibrillar matrix [60, 61]. More recent contributions underlined that mineralization pathways in bone are neither exclusively intrafibrillar nor extrafibrillar [62], but rather form a continuous cross-fibrillar phase [38], but this feature remains largely unexplored for the tendon-to-bone insertion [23]. Fourth, the profiles of the competing gradients in mineral content and collagen fibers orientation were selected according to earlier modeling strategies [22, 23], themselves based on Raman spectroscopy [26] and polarized light microscopy [42]. Nevertheless, recent experimental developments for measuring these finely tuned gradients across the interphase are likely to provide different (nonlinear) profiles [63, 64], which could be used as well to feed our modeling approach. Fifth, based on the considered biological phases and their interactions at each scale [34, 56], different methods have been used to estimate the effective stiffness tensor at each homogenization step: The Mori-Tanaka method (steps 1, 3 and 4), the self-consistent method (step 2), and the "inverse Mori-Tanaka" scheme (steps 5 and 6). It is commonly ackowledged that the Mori-Tanaka method shows limited performance for problems involving high volume fraction of inclusions over around 35% [65], since the inclusions' distribution and interactions are not accounted for properly. Therefore, the attributions of matrix and inclusions roles in our modeling steps 3 and 4 are open to question, so that other homogenization methods could have been used. For instance, a

rigorous approach has been proposed for composites containing multiple classes of aligned ellipsoidal inclusions with a relatively high volume fraction [24], although this scheme can violate the Hashin-Shtrikman bounds at low volume fraction for certain anisotropy of the phases. Lastly, our modeling approach contains many steps, each of which should be validated experimentally in the future. To date, little information is available in the literature concerning the experimental multiscale evaluation of the mechanical properties at the tendon-to-bone attachment. Current imaging modalities have been used to map the local content of the main constituents across the interphase [10, 26, 63], but a direct link with the corresponding variations in mechanical properties is somehow still missing. Ongoing developments of experimental techniques for measuring the local mechanical properties of the interphase at different scales, such as nanoscale dynamic mechanical analysis [66] or scanning acoustic microscopy [67], are expected to provide means of comparing our numerically obtained predictions.

All these uncertainties along with some other model parameters ignored in this work, such as the gradient in protein content [68], the different collagen types across the interphase [4] or the unraveling of tendon fibers into smaller interphase fibrils [10], make the multiscale modeling of the tendon-to-bone insertion a challenging problem with much potential for future works. As such, the modeling process proposed here is straightforwardly extendable to account for damage characteristics as a footprint of clinical burden that occur at the tendon-to-bone insertion, which may include for instance the multiscale effects of unloading (*e.g.*, stiffening of the HA foam at the nanoscale or fibers misalignment at the microscale) [56]. Besides, such model paves the way to the design of bioinspired bi-materials [69] that display the functionally graded properties of the enthesis, and their characterization using quantitative ultrasound [70, 71].

2.6 Conclusion

We modeled the tendon-to-bone insertion as a hierarchical composite material and predicted its effective anisotropic stiffness tensor at the tissue scale. Our multiscale analysis involved a bottom-up approach, starting from the nanostructural level (partially mineralized collagen fibril) and then moving up the scales through the sub-microstructural level (partially mineralized fiber), the microstructural level (pattern of partially mineralized fibers), up to the mesostructural level (partially mineralized tissue level). Our modeling results supported the hypothesis that the tendon-to-bone insertion can be considered as a continuous functionally graded material with respect to its mineral concentration and collagen fibers organization, thus confirming earlier results obtained using phenomenological models (*i.e.*, stochastic finite element simulations) and experimentally reported trends.

Acknowledgement

This work was partially funded by the BEST-AMUS project (IIN program, CNRS-INSIS), the "Support for research for newly appointed Associate Professors" and the "Bonus Qualité Recherche" (Faculté des Sciences et Technologie, Université Paris-Est Créteil).

Appendices

A.1 Hill tensor $\mathbb{P}^0$

A.1.1 Hill tensor for a cylindrical inclusion in a transversely isotropic medium

The non-zero components of the Hill tensor $\mathbb{P}^0$ for a cylindrical inclusion embedded in a transversely isotropic matrix of stiffness $\mathbb{C}^0$ are given according to [72] using Voigt notation, x_3 being the axis of rotational symmetry,

$$P^0_{11} = \frac{1}{8}\frac{(C^0_{22}+C^0_{66})+2C^0_{66}}{C^0_{22}C^0_{66}}\,, \tag{A.1}$$

$$P^0_{22} = \frac{1}{8}\frac{(C^0_{22}+3C^0_{66})}{C^0_{22}C^0_{66}}\,, \tag{A.2}$$

$$P^0_{12} = \frac{1}{8}\frac{C^0_{66}-C^0_{22}}{C^0_{22}C^0_{66}}\,, \tag{A.3}$$

$$P^0_{66} = \frac{1}{2}\frac{C^0_{22}+C^0_{66}}{C^0_{22}C^0_{66}}\,, \tag{A.4}$$

$$P^0_{44} = \frac{1}{2C^0_{44}}\,, \tag{A.5}$$

$$P^0_{55} = P^0_{44}\,. \tag{A.6}$$

A.1.2 Hill tensors for a spherical inclusion in an isotropic medium

Considering the case of a spherical inclusion embedded in an isotropic matrix of stiffness $\mathbb{C}^0$ [72], the components of the Hill tensor $\mathbb{P}^0$ now read as

$$P^0_{11} = \frac{7C^0_{44}+2C^0_{12}}{15C^0_{44}(C^0_{12}+2C^0_{44})}\,, \tag{A.7}$$

$$P^0_{12} = \frac{C^0_{44}+C^0_{12}}{-15C^0_{44}(C^0_{12}+2C^0_{44})}\,, \tag{A.8}$$

$$P^0_{44} = \frac{2(3C^0_{12}+8C^0_{44})}{15C^0_{44}(C^0_{12}+2C^0_{44})}\,, \tag{A.9}$$

$$P^0_{22} = P^0_{33} = P^0_{11},\quad P^0_{55} = P^0_{66} = P^0_{44},\quad P^0_{13} = P^0_{23} = P^0_{12}\,. \tag{A.10}$$

B.1 Effective stiffness tensor of the hydroxyapatite foam $\mathbb{C}_{\mathbf{Hw}}(x)$

The self-consistent scheme for two interpenetrating (spherical) inclusion phases with a linear elastic and isotropic behavior can be solved according to [32]. In such a case,

the nonlinear system of equations (2.3) can be substituted by a system of two nonlinear equations (note that the spatial variable x was omitted here for sake of clarity),

$$\frac{f_{\mathrm{HA}}(K_{\mathrm{HA}} - K_{\mathrm{Hw}})}{1 + \alpha_{\mathrm{Hw}}(K_{\mathrm{HA}} - K_{\mathrm{Hw}})/K_{\mathrm{Hw}}} + \frac{(1 - f_{\mathrm{HA}})(K_{\mathrm{wp}} - K_{\mathrm{Hw}})}{1 + \alpha_{\mathrm{Hw}}(K_{\mathrm{wp}} - K_{\mathrm{Hw}})/K_{\mathrm{Hw}}} = 0\,, \tag{B.1}$$

$$\frac{f_{\mathrm{HA}}(G_{\mathrm{HA}} - G_{\mathrm{Hw}})}{1 + \beta_{\mathrm{Hw}}(G_{\mathrm{HA}} - G_{\mathrm{Hw}})/G_{\mathrm{Hw}}} + \frac{(1 - f_{\mathrm{HA}})(G_{\mathrm{wp}} - G_{\mathrm{Hw}})}{1 + \beta_{\mathrm{Hw}}(G_{\mathrm{wp}} - G_{\mathrm{Hw}})/G_{\mathrm{Hw}}} = 0\,, \tag{B.2}$$

where the two unknowns K_{Hw} and G_{Hw} denote the bulk and shear moduli of the HA foam, respectively. The parameters α_{Hw} and β_{Hw} are defined as

$$\alpha_{\mathrm{Hw}} = \frac{3K_{\mathrm{Hw}}}{3K_{\mathrm{Hw}} + 4G_{\mathrm{Hw}}}\,, \quad \beta_{\mathrm{Hw}} = \frac{6(K_{\mathrm{Hw}} + 2G_{\mathrm{Hw}})}{5(3K_{\mathrm{Hw}} + 4G_{\mathrm{Hw}})}\,. \tag{B.3}$$

Solving the aforementioned system yields the following components for the stiffness tensor of the hydroxyapatite foam,

$$C_{11}^{\mathrm{Hw}} = K_{\mathrm{Hw}} + \frac{4}{3}G_{\mathrm{Hw}}\,, \tag{B.4}$$

$$C_{12}^{\mathrm{Hw}} = K_{\mathrm{Hw}} - \frac{2}{3}G_{\mathrm{Hw}}\,, \tag{B.5}$$

$$C_{44}^{\mathrm{Hw}} = G_{\mathrm{Hw}}\,, \tag{B.6}$$

$$C_{22}^{\mathrm{Hw}} = C_{33}^{\mathrm{Hw}} = C_{11}^{\mathrm{Hw}}\,, \quad C_{13}^{\mathrm{Hw}} = C_{23}^{\mathrm{Hw}} = C_{12}^{\mathrm{Hw}}, \quad C_{55}^{\mathrm{Hw}} = C_{66}^{\mathrm{Hw}} = C_{44}^{\mathrm{Hw}}\,. \tag{B.7}$$

Bibliography

[1] M Benjamin, T Kumai, S Milz, BM Boszczyk, AA Boszczyk, and JR Ralphs. The skeletal attachment of tendons–tendon 'entheses'. *Comp Biochem Physiol A Mol Integr Physiol*, 133(4):931–945, 2002.

[2] J Buschmann and GM Bürgisser. *Biomechanics of tendons and ligaments: tissue reconstruction and regeneration*. Woodhead Publishing, 2017.

[3] J Apostolakos, TJS Durant, CR Dwyer, RP Russell, JH Weinreb, F Alaee, K Beitzel, MB McCarthy, MP Cote, and AD Mazzocca. The enthesis: a review of the tendon-to-bone insertion. *Muscles Ligaments Tendons J*, 4(3):333, 2014.

[4] AD Waggett, JR Ralphs, APL Kwan, D Woodnutt, and M Benjamin. Characterization of collagens and proteoglycans at the insertion of the human Achilles tendon. *Matrix Biol*, 16(8):457–470, 1998.

[5] S Weiner and HD Wagner. The material bone: structure-mechanical function relations. *Annu Rev Mater Sci*, 28(1):271–298, 1998.

[6] HH Lu and S Thomopoulos. Functional attachment of soft tissues to bone: development, healing, and tissue engineering. *Annu Rev Biomed Eng*, 15:201–226, 2013.

[7] Y Liu, V Birman, C Chen, S Thomopoulos, and GM Genin. Mechanisms of bimaterial attachment at the interface of tendon to bone. *J Eng Mater Technol*, 133(1):011006, 2011.

[8] Y Hu, V Birman, A Deymier-Black, AG Schwartz, S Thomopoulos, and GM Genin. Stochastic interdigitation as a toughening mechanism at the interface between tendon and bone. *Biophys J*, 108(2):431–437, 2015.

[9] SF Tellado, ER Balmayor, and M Van Griensven. Strategies to engineer tendon/ligament-to-bone interface: Biomaterials, cells and growth factors. *Adv Drug Deliv Rev*, 94:126–140, 2015.

[10] L Rossetti, LA Kuntz, E Kunold, J Schock, KW Müller, H Grabmayr, J Stolberg-Stolberg, F Pfeiffer, SA Sieber, R Burgkart, and AR Bausch. The microstructure and micromechanics of the tendon–bone insertion. *Nat Mater*, 16(6):664, 2017.

[11] GM Genin and S Thomopoulos. The tendon-to-bone attachment: Unification through disarray. *Nat Mater*, 16(6):607, 2017.

[12] N Felsenthal and E Zelzer. Mechanical regulation of musculoskeletal system development. *Development*, 144(23):4271–4283, 2017.

[13] AG Schwartz, JH Lipner, JD Pasteris, GM Genin, and S Thomopoulos. Muscle loading is necessary for the formation of a functional tendon enthesis. *Bone*, 55(1):44–51, 2013.

[14] F Saadat, AC Deymier, V Birman, S Thomopoulos, and GM Genin. The concentration of stress at the rotator cuff tendon-to-bone attachment site is conserved across species. *J Mech Behav Biomed Mater*, 62:24–32, 2016.

[15] GS Jung and MJ Buehler. Multiscale modeling of muscular-skeletal systems. *Annu Rev Biomed Eng*, 19:435–457, 2017.

[16] A Fritsch and C Hellmich. 'Universal' microstructural patterns in cortical and trabecular, extracellular and extravascular bone materials: micromechanics-based prediction of anisotropic elasticity. *J Theor Biol*, 244(4):597–620, 2007.

[17] S Nikolov and D Raabe. Hierarchical modeling of the elastic properties of bone at submicron scales: the role of extrafibrillar mineralization. *Biophys J*, 94(11):4220–4232, 2008.

[18] YJ Yoon and SC Cowin. The estimated elastic constants for a single bone osteonal lamella. *Biomech Model Mechanobiol*, 7(1):1–11, 2008.

[19] E Hamed, I Jasiuk, A Yoo, Y Lee, and T Liszka. Multi-scale modelling of elastic moduli of trabecular bone. *J R Soc Interface*, 9(72):1654–1673, 2012.

[20] S Tiburtius, S Schrof, F Molnár, P Varga, F Peyrin, Q Grimal, K Raum, and A Gerisch. On the elastic properties of mineralized turkey leg tendon tissue: multiscale model and experiment. *Biomech Model Mechanobiol*, 13(5):1003–1023, 2014.

[21] EM Spiesz and PK Zysset. Structure–mechanics relationships in mineralized tendons. *J Mech Behav Biomed Mater*, 52:72–84, 2015.

[22] GM Genin, A Kent, V Birman, B Wopenka, JD Pasteris, PJ Marquez, and S Thomopoulos. Functional grading of mineral and collagen in the attachment of tendon to bone. *Biophys J*, 97(4):976–985, 2009.

[23] Y Liu, S Thomopoulos, C Chen, V Birman, MJ Buehler, and GM Genin. Modelling the mechanics of partially mineralized collagen fibrils, fibres and tissue. *J R Soc Interface*, 11(92):20130835, 2014.

[24] F Saadat, V Birman, S Thomopoulos, and GM Genin. Effective elastic properties of a composite containing multiple types of anisotropic ellipsoidal inclusions, with application to the attachment of tendon to bone. *J Mech Phys Solids*, 82:367–377, 2015.

[25] AC Deymier, Y An, JJ Boyle, AG Schwartz, V Birman, GM Genin, S Thomopoulos, and AH Barber. Micro-mechanical properties of the tendon-to-bone attachment. *Acta Biomater*, 56:25–35, 2017.

[26] B Wopenka, A Kent, JD Pasteris, Y Yoon, and S Thomopoulos. The tendon-to-bone transition of the rotator cuff: a preliminary raman spectroscopic study documenting the gradual mineralization across the insertion in rat tissue samples. *Appl Spectrosc*, 62(12):1285–1294, 2008.

[27] A Zaoui. Continuum micromechanics: survey. *J Eng Mech*, 128(8):808–816, 2002.

[28] JD Eshelby. The determination of the elastic field of an ellipsoidal inclusion, and related problems. *Proc R Soc Lond A*, 241(1226):376–396, 1957.

[29] D Gagliardi, V Sansalone, C Desceliers, and S Naili. Estimation of the effective bone-elasticity tensor based on μCT imaging by a stochastic model. a multi-method validation. *Eur J Mech A-Solid*, 69:147–167, 2018.

[30] T Mori and K Tanaka. Average stress in matrix and average elastic energy of materials with misfitting inclusions. *Acta Metall*, 21(5):571–574, 1973.

[31] R Hill. A self-consistent mechanics of composite materials. *J Mech Phys Solids*, 13(4):213–222, 1965.

[32] C Hellmich, J-F Barthélémy, and L Dormieux. Mineral–collagen interactions in elasticity of bone ultrastructure–a continuum micromechanics approach. *Eur J Mech A Solids*, 23(5):783–810, 2004.

[33] E Hamed, Y Lee, and I Jasiuk. Multiscale modeling of elastic properties of cortical bone. *Acta Mech*, 213(1-2):131–154, 2010.

[34] B Alexander, TL Daulton, GM Genin, J Lipner, JD Pasteris, B Wopenka, and S Thomopoulos. The nanometre-scale physiology of bone: steric modelling and scanning transmission electron microscopy of collagen–mineral structure. *J R Soc Interface*, 9(73):1774–1786, 2012.

[35] J Orgel, TC Irving, A Miller, and TJ Wess. Microfibrillar structure of type I collagen in situ. *Proc Natl Acad Sci*, 103(24):9001–9005, 2006.

[36] P Fratzl, HS Gupta, EP Paschalis, and P Roschger. Structure and mechanical quality of the collagen–mineral nano-composite in bone. *J Mater Chem*, 14(14):2115–2123, 2004.

[37] A Fritsch, C Hellmich, and L Dormieux. Ductile sliding between mineral crystals followed by rupture of collagen crosslinks: experimentally supported micromechanical explanation of bone strength. *J Theor Biol*, 260(2):230–252, 2009.

[38] N Reznikov, M Bilton, L Lari, MM Stevens, and R Kröger. Fractal-like hierarchical organization of bone begins at the nanoscale. *Science*, 360(6388):eaao2189, 2018.

[39] P Kannus. Structure of the tendon connective tissue. *Scand J Med Sci Sports*, 10(6):312–320, 2000.

[40] E Hamed, E Novitskaya, J Li, P-Y Chen, I Jasiuk, and J McKittrick. Elastic moduli of untreated, demineralized and deproteinized cortical bone: validation of a theoretical model of bone as an interpenetrating composite material. *Acta Biomater*, 8(3):1080–1092, 2012.

[41] CT Thorpe, KJ Karunaseelan, J Ng Chieng Hin, GP Riley, HL Birch, PD Clegg, and HRC Screen. Distribution of proteins within different compartments of tendon varies according to tendon type. *J Anat*, 229(3):450–458, 2016.

[42] S Thomopoulos, JP Marquez, B Weinberger, V Birman, and GM Genin. Collagen fiber orientation at the tendon to bone insertion and its influence on stress concentrations. *J Biomech*, 39(10):1842–1851, 2006.

[43] J Qu and M Cherkaoui. *Fundamentals of micromechanics of solids*. Wiley Online Library, 2006.

[44] BK Hoffmeister, SM Handley, SA Wickline, and JG Miller. Ultrasonic determination of the anisotropy of Young's modulus of fixed tendon and fixed myocardium. *J Acoust Soc Am*, 100(6):3933–3940, 1996.

[45] J Brum, M Bernal, JL Gennisson, and M Tanter. In vivo evaluation of the elastic anisotropy of the human Achilles tendon using shear wave dispersion analysis. *Phys Med Biol*, 59(3):505, 2014.

[46] S Bernard, J Schneider, P Varga, P Laugier, K Raum, and Q Grimal. Elasticity–density and viscoelasticity–density relationships at the tibia mid-diaphysis assessed from resonant ultrasound spectroscopy measurements. *Biomech Model Mechan*, 15(1):97–109, 2016.

[47] X Cai, H Follet, L Peralta, M Gardegaront, D Farlay, R Gauthier, B Yu, E Gineyts, C Olivier, M Langer, A Gourrier, D Mitton, F Peyrin, Q Grimal, and P Laugier. Anisotropic elastic properties of human femoral cortical bone and relationships with composition and microstructure in elderly. *Acta Biomater*, 90:254–266, 2019.

[48] N Bochud, J Laurent, F Bruno, D Royer, and C Prada. Towards real-time assessment of anisotropic plate properties using elastic guided waves. *J Acoust Soc Am*, 143(2):1138–1147, 2018.

[49] KN Hauch, ML Oyen, GM Odegard, and TL Haut Donahue. Nanoindentation of the insertional zones of human meniscal attachments into underlying bone. *J Mech Behav Biomed Mater*, 2(4):339–347, 2009.

[50] D Gagliardi, S Naili, C Desceliers, and V Sansalone. Tissue mineral density measured at the sub-millimetre scale can provide reliable statistics of elastic properties of bone matrix. *Biomech Model Mechan*, 16(6):1885–1910, 2017.

[51] E Hamed and I Jasiuk. Elastic modeling of bone at nanostructural level. *Mater Sci Eng R Rep*, 73(3-4):27–49, 2012.

[52] MJ Buehler. Molecular nanomechanics of nascent bone: fibrillar toughening by mineralization. *Nanotechnology*, 18(29):295102, 2007.

[53] A Gautieri, S Vesentini, A Redaelli, and MJ Buehler. Viscoelastic properties of model segments of collagen molecules. *Matrix Biol*, 31(2):141–149, 2012.

[54] S Von Euw, T-H-C Chan-Chang, C Paquis, G Haye, Band Pehau-Arnaudet, F Babonneau, T Azaïs, and N Nassif. Organization of bone mineral: The role of mineral–water interactions. *Geosciences*, 8(12):466, 2018.

[55] MA Rubin, I Jasiuk, J Taylor, J Rubin, T Ganey, and RP Apkarian. TEM analysis of the nanostructure of normal and osteoporotic human trabecular bone. *Bone*, 33(3):270–282, 2003.

[56] AC Deymier, AG Schwartz, Z Cai, TL Daulton, JD Pasteris, GM Genin, and S Thomopoulos. The multiscale structural and mechanical effects of mouse supraspinatus muscle unloading on the mature enthesis. *Acta Biomater*, 83:302–313, 2019.

[57] JL Katz and K Ukraincik. On the anisotropic elastic properties of hydroxyapatite. *J Biomech*, 4(3):221–227, 1971.

[58] S Weiner and W Traub. Organization of hydroxyapatite crystals within collagen fibrils. *FEBS letters*, 206(2):262–266, 1986.

[59] N Sasaki and Y Sudoh. X-ray pole figure analysis of apatite crystals and collagen molecules in bone. *Calcif Tissue Int*, 60(4):361–367, 1997.

[60] N Sasaki, A Tagami, T Goto, M Taniguchi, M Nakata, and K Hikichi. Atomic force microscopic studies on the structure of bovine femoral cortical bone at the collagen fibril-mineral level. *J Mater Sci: Mater*, 13(3):333–337, 2002.

[61] EA McNally, HP Schwarcz, GA Botton, and AL Arsenault. A model for the ultrastructure of bone based on electron microscopy of ion-milled sections. *PLOS one*, 7(1):e29258, 2012.

[62] M Georgiadis, R Müller, and P Schneider. Techniques to assess bone ultrastructure organization: orientation and arrangement of mineralized collagen fibrils. *J R Soc Interface*, 13(119):20160088, 2016.

[63] JP Spalazzi, AL Boskey, N Pleshko, and HH Lu. Quantitative mapping of matrix content and distribution across the ligament-to-bone insertion. *PLoS One*, 8(9):e74349, 2013.

[64] D Qu, SD Subramony, AL Boskey, N Pleshko, SB Doty, and HH Lu. Compositional mapping of the mature anterior cruciate ligament-to-bone insertion. *J Orthop Res*, 35(11):2513–2523, 2017.

[65] HM Yin, LZ Sun, and Glaucio H Paulino. Micromechanics-based elastic model for functionally graded materials with particle interactions. *Acta Mater*, 52(12):3535–3543, 2004.

[66] I Zlotnikov, E Zolotoyabko, and P Fratzl. Nano-scale modulus mapping of biological composite materials: Theory and practice. *Prog Mater Sci*, 87:292–320, 2017.

[67] S Leicht and K Raum. Acoustic impedance changes in cartilage and subchondral bone due to primary arthrosis. *Ultrasonics*, 48(6-7):613–620, 2008.

[68] S Thomopoulos, GR Williams, JA Gimbel, M Favata, and LJ Soslowsky. Variation of biomechanical, structural, and compositional properties along the tendon to bone insertion site. *J Orthop Res*, 21(3):413–419, 2003.

[69] MJ Mirzaali, AH de la Nava, D Gunashekar, M Nouri-Goushki, RPE Veeger, Q Grossman, L Angeloni, MK Ghatkesar, LE Fratila-Apachitei, D Ruffoni, EL Doubrovski, and AA Zadpoor. Mechanics of bioinspired functionally graded soft-hard composites made by multi-material 3D printing. *Compos Struct*, page 111867, 2020.

[70] N Bochud, Q Vallet, J-G Minonzio, and P Laugier. Predicting bone strength with ultrasonic guided waves. *Sci Rep*, 7:43628, 2017.

[71] G Rosi, L Placidi, V-H Nguyen, and S Naili. Wave propagation across a finite heterogeneous interphase modeled as an interface with material properties. *Mech Res Commun*, 84:43–48, 2017.

[72] AP Suvorov and GJ Dvorak. Rate form of the Eshelby and Hill tensors. *Int J Solids Struct*, 39(21-22):5659–5678, 2002.

Chapter 3. Wave propagation across a functionally graded interphase between soft and hard solids: Insight from a dynamic surface elasticity model

The work presented in this chapter is issued from the following publication:
A Aghaei, N Bochud, G Rosi, and S Naili, Wave propagation across a functionally graded interphase between soft and hard solids: Insight from a dynamic surface elasticity model, *J Mech Phys Solids*, 151: 104380, 2021.

Contents

Abstract

Joining soft to hard materials is a challenging problem in modern engineering applications. In order to alleviate stress concentrations at the interface between materials with such a mismatch in mechanical properties, the use of functionally graded interphases is becoming more widespread in the design of the new generation of engineered composite materials. However, current macroscale models that aim at mimicking the mechanical behavior of such complex systems generally fail in incorporating the impact of microstructural details across the interphase because of computational burden. In this paper we propose to replace the thin, but yet finite, functionally graded interphase by a zero-thickness interface. This is achieved by means of an original model developed in the framework of surface elasticity, which accounts for both the elastic and inertial behavior of the actual interphase. The performance of the proposed equivalent model is evaluated in the context of elastic wave propagation, by comparing the calculated reflection coefficient to that obtained using different baseline models. Numerical results show that our dynamic surface elasticity model provides an accurate approximation of the reference interphase model over a broad frequency range. We demonstrate application of this modeling approach for the characterization of the graded tissue system at the tendon-to-bone interphase, which fulfills the challenging task of integrating soft to hard tissues over a submillimeter-wide region.

Keyword: Functionally graded interphase, Equivalent interface model, Enriched surface elasticity, Tendon-to-bone attachment, Elastic waves

3.1 Introduction

From a mechanical viewpoint, when materials having a dissimilar mechanical nature (*e.g.*, soft and hard) are attached together, they typically display highly non-uniform deformations upon loading, eventually leading to stress concentration at their abrupt interface, which in turn increase the failure probability. An appealing solution to improve the integration between soft and hard materials consists in designing functionally graded interphases, which are typically conceived as multilayers whose composition, microstructure and material properties gradually vary in space, in order to reduce mechanical stresses [1]. Naturally present in the human body [2], graded materials represent a source of inspiration that offers technological solutions for general engineering purposes as well as for biomedical applications. This concerns for instance the skin, which is a complex multilayered system, where each layer has a specific and age-related biomechanical behavior [3], the cortex of long bones, which displays an increasing gradient of porosity from the periosteum to the endosteum that is, in turn, related to a gradual change in mechanical properties such as tensile strength and elasticity [4], and the so-called *entheses*, which are specialized interfacial regions of the musculoskeletal system that allow joining connective tissues, such as tendon, ligament or cartilage, to bone [5].

In particular, the tendon-to-bone interphase serves the challenging task of connecting two highly dissimilar tissues over a very small region, which is typically a few hundreds of micrometers wide (see Fig. 3.1a). This interphase has the remarkable ability to minimize stress concentration and related failure modes, with the possibility to withstand

forces higher than the body weight for millions of loading cycles [6, 7]. These outstanding features, achieved by means of finely tuned gradients in structure, composition and biomechanical properties at different length scales (see Fig. 3.1b) [7, 8], are currently playing a significant role in the design of bioinspired interphases [9–11]. To unlock those

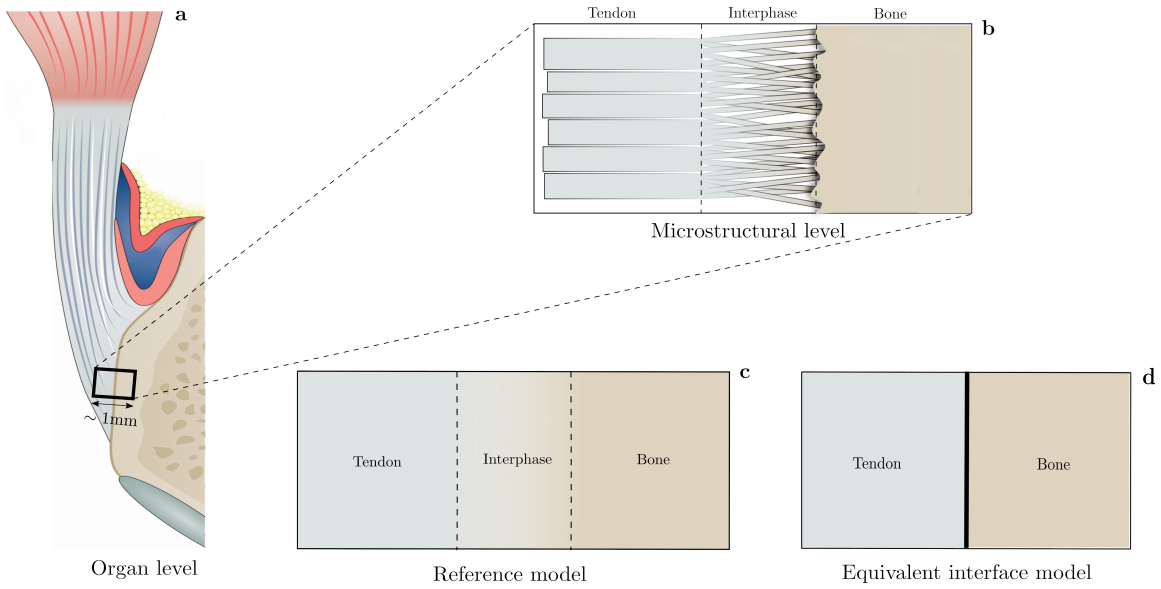

Figure 3.1 – (a) Organ level illustration of the tendon-to-bone attachment at the insertion site corresponding to the Achilles tendon (image adapted from Ref. [12]); (b) Schematic of the attachment at the microstructural level, highlighting the gradients in composition and biomechanical properties across the tendon-to-bone interphase (image adapted from Ref. [8]); (c) Finite thickness interphase model with varying mechanical properties across the interphase; and (d) Equivalent interface model with specific properties.

mechanisms, computational models were developed both to investigate fundamental anchoring strategies at the microstructural level [13–16] or to address applied orthopedic strategies at the organ level [17–19]. Notwithstanding, from a modeling viewpoint, it is highly challenging to bridge the gap between these two levels [20], and current models targeting reattachment procedures of the tendon-to-bone interphase should be enriched by including a more detailed description of the microstructure [21, 22]. Indeed, to adequately capture the mechanical behavior of a graded interphase layer, the optimal choice would be to consider its exact geometry and varying mechanical properties across the two surrounding tissues [23]. However, this choice can be prohibitive when dealing with complex heterogeneous interphases. In particular, the finite size of such interphase, which is very small compared to that of the surrounding tissues, may cause computational burden when mesh refinements are required for convergence purposes. In contrast, a too basic model that would simplify the interphase to a large extent, or even ignore it, would fail in capturing its mechanics. To face these limitations, a possible solution consists in replacing the finite heterogeneous interphase (see Fig. 3.1c) by an equivalent interface with specific properties (see Fig. 3.1d) that retains the mechanical behavior of the original medium over a certain range of validity.

It is commonly accepted that such modeling approach can be satisfactorily addressed by enriching the equivalent model with additional fields [24]. Initial attempts proposed

to tackle this problem by replacing the interphase by an interface with null thickness and purely elastic properties. A general framework for such general elastic interface model was comprehensively described in [25, 26], and was subsequently extended to account for the case where both the interphase and its surrounding media are anisotropic [27, 28] or the case of an elasto-plastic interphase [29, 30]. In the case of dynamic problems, however, and especially when dealing with wave propagation, a purely elastic surface model generally fails in accounting for the local interactions between the mechanical perturbation (*e.g.*, a wave) and the interphase, even if its dimensions are much smaller than the involved mechanical characteristic length (*e.g.*, the wavelength). Within this context, the inertial behavior of the interphase can have a considerable impact on its macroscopic dynamic response and should thus be included into the modeling strategy. This observation was also at the basis of the concept of a structural interface that possesses a finite thickness, which was introduced in [31] and further developed in [32], where the role of its inertial properties was highlighted. In the case of resonant meta-interfaces, an alternative approach was to obtain effective jump conditions by applying a suitable homogenization process [33, 34]. Moreover, some studies on elastic wave propagation showed that when the interphase is located between two surrounding media with microstructure, inertial properties also play a pivotal role in the modeling of the equivalent interface [35–37].

Following these recent findings, and in line with a former study by our group [38], we introduce here an enriched equivalent interface model, whose properties are defined by means of surface kinetic and potential energy densities. Furthermore, to account for the nonlinear gradients in mechanical properties across the interphase found at the tendon-to-bone attachement [39], we hypothesize that the displacement field can be approximated using a piece-wise affine profile, whose characteristics depend upon an additional degree-of-freedom within the interface. The performance of our modeling approach is evaluated by calculating the frequency-dependent reflection coefficient of a plane pressure wave under normal incidence. First, based on energetic concepts, the identification of the specific surface properties of the equivalent interface model is achieved by comparison with the reference interphase model. Second, an optimization procedure is conducted to investigate the impact of the additional degree-of-freedom. Third, the performance of the optimal equivalent model is compared to different models available in the literature, which typically serve as a baseline in finite element (FE) simulations at the organ scale. Our numerical results show that this enriched model with specific interface conditions provides a very accurate approximation of the reference model over a broad frequency range, thus outperforming more simplistic models that fail in capturing the complex dynamics of the interphase. As a by-product, the link between the position of the additional degree-of-freedom and the microstructural features of the interphase (*e.g.*, competing gradients in mineral content and collagen fibers organization) is also discussed, thus opening promising perspectives for characterizing the tendon-to-bone attachment status. Elastic waves indeed represent a relevant nondestructive means to probe the interphase quality, as they possess intrinsic sensitivity to the mechanical properties contributing to the tendon-to-bone attachment strength. Overall this modeling approach represents the first building block for developing more sophisticated models targeting reattachment procedures at the organ scale that incorporate a more detailed description of properties at lower length scales.

The paper is structured as follows: Sect. 3.2 introduces the theoretical fundamentals of our modeling approach. The numerical results are then presented in Sect. 3.3. Finally,

the strengths and limitations of the proposed model are discussed in Sect. 4.6.

3.2 Theory

Based on the variational principles [40–42], this section first presents the governing equations and boundary conditions for the two models depicted in Fig. 3.1c–d: (1) A reference model, which consists in a finite thickness interphase with a gradient in mechanical properties, surrounded by two homogeneous media (see Subsect. 3.2.1), and (2) an equivalent model in which the interphase is replaced by specific interface conditions between the two homogeneous media (see Subsect. 3.2.2). This general framework is then reduced to the specific case of a pressure plane wave propagating under normal incidence (see Subsect. 3.2.3). Finally, the strategy to identify the coefficients of the equivalent interface model is described in Subsect. 3.2.4.

3.2.1 Reference interphase model

Let us consider the Cartesian frame of reference with coordinates $\mathbf{R}(O;\mathbf{e}_1,\mathbf{e}_2,\mathbf{e}_3)$, where O is the origin and $(\mathbf{e}_1,\mathbf{e}_2,\mathbf{e}_3)$ is an orthonormal basis for the space. The coordinates of a point M in $\mathbf{R}$ are specified by (x_1,x_2,x_3) and the time is denoted by t. As depicted in Fig. 3.2, the reference model consists of two homogeneous half-spaces $\Omega^- = \{(x_1,x_2,x_3) \mid x_2,x_3 \in \mathbb{R} \text{ and } x_1 < -\frac{h}{2}\}$ and $\Omega^+ = \{(x_1,x_2,x_3) \mid x_2,x_3 \in \mathbb{R} \text{ and } x_1 > \frac{h}{2}\}$, separated by an heterogeneous interphase layer of thickness h, namely $\Omega^I = \{(x_1,x_2,x_3) \mid x_2,x_3 \in \mathbb{R} \text{ and } -\frac{h}{2} < x_1 < \frac{h}{2}\}$, where $\mathbb{R}$ is the set of real numbers. In

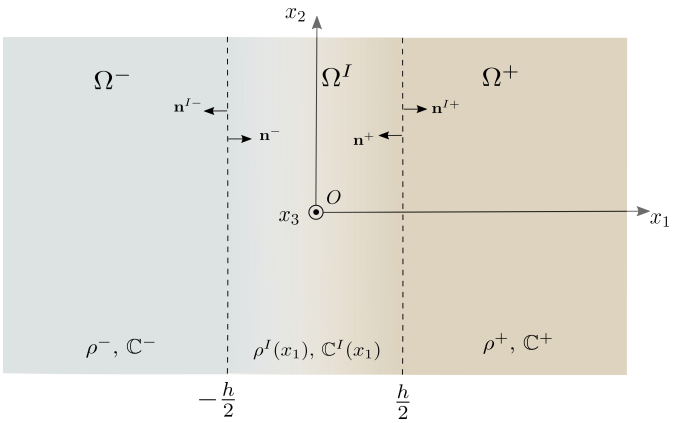

Figure 3.2 – Modeling configuration of the reference model: A finite thickness interphase Ω^I with varying mechanical properties along the x_1-direction is surrounded by two homogeneous half-spaces $\Omega^\pm$. Superscripts $+$, $-$ and I denote the variables associated with the domains Ω^+, Ω^-, and Ω^I, respectively.

what follows, the equations of motion are derived according to the least action principle. To this end, we introduce the action functional $\mathcal{A}^{\text{ref}}$ of the considered system as in [36],

$$\mathcal{A}^{\text{ref}} = \int_{\Omega\times(0,t_f)} \left[T^+ + T^- + T^I - U^+ - U^- - U^I\right] dA, \tag{3.1}$$

where $\Omega = \Omega^{\pm} \cup \Omega^I$ spans the complete domain of interest, $(0, t_f)$ is a time interval and dA represents the differential volume element. The kinetic and potential energy densities per unit volume, T and U, associated with each domain of interest are defined as,

$$T^{\pm} = \frac{1}{2}\rho^{\pm}\dot{\mathbf{u}}^{\pm}.\dot{\mathbf{u}}^{\pm} \quad \text{and} \quad U^{\pm} = \frac{1}{2}\boldsymbol{\sigma}^{\pm} : \boldsymbol{\epsilon}^{\pm}, \tag{3.2}$$

$$T^{I} = \frac{1}{2}\rho^{I}(x_1)\dot{\mathbf{u}}^{I}.\dot{\mathbf{u}}^{I} \quad \text{and} \quad U^{I} = \frac{1}{2}\boldsymbol{\sigma}^{I} : \boldsymbol{\epsilon}^{I}, \tag{3.3}$$

where $\rho^{\pm}$ are the mass densities of the domains $\Omega^{\pm}$, and $\rho^I(x_1)$ is the mass density of the interphase Ω^I, which varies along the x_1-direction. The displacement vector associated with each domain is denoted by $\mathbf{u}$, where the superimposed dot denotes the first derivative with respect to time. The stress and infinitesimal strain tensors associated with each domain are denoted by $\boldsymbol{\sigma}$ and $\boldsymbol{\epsilon}$, respectively, the latter being defined as $\boldsymbol{\epsilon} = (1/2)\left(\nabla\mathbf{u} + (\nabla\mathbf{u})^T\right)$, whereby ∇ and the superscript T denote the gradient and transpose operators, respectively. The operators dot (.) and colon (:) denote the scalar product of two vectors and the double contracted product of two tensors, respectively.

The least action principle implies that the variation of the action defined by Eq. (3.1) should verify that $\delta\mathcal{A}^{\text{ref}} = 0$. This condition, along with the consideration of kinematic constraints on the boundaries, *i.e.*, the continuity of displacements between the domains $\Omega^{\pm}$ and Ω^I, leads to the following boundary value problem for the reference model,

$$\left\{\begin{array}{ll} \nabla.\boldsymbol{\sigma}^{\pm} - \rho^{\pm}\ddot{\mathbf{u}}^{\pm} = \mathbf{0} & \forall M \in \Omega^{\pm} \\ \nabla.\boldsymbol{\sigma}^{I} - \rho^{I}(x_1)\ddot{\mathbf{u}}^{I} = \mathbf{0} & \forall M \in \Omega^{I} \\ \left.\begin{array}{l} \boldsymbol{\sigma}^{-}\mathbf{n}^{-} + \boldsymbol{\sigma}^{I}\mathbf{n}^{I-} = \mathbf{0} \\ \mathbf{u}^{-} - \mathbf{u}^{I} = \mathbf{0} \end{array}\right\} & \text{for} \quad x_1 = -\dfrac{h}{2} \\ \left.\begin{array}{l} \boldsymbol{\sigma}^{I}\mathbf{n}^{I+} + \boldsymbol{\sigma}^{+}\mathbf{n}^{+} = \mathbf{0} \\ \mathbf{u}^{I} - \mathbf{u}^{+} = \mathbf{0} \end{array}\right\} & \text{for} \quad x_1 = \dfrac{h}{2} \end{array}\right. , \tag{3.4}$$

where $\nabla.$ denote the divergence operator. The constitutive relation associated with each domain is defined in the frame of the linear elasticity, *i.e.*, $\boldsymbol{\sigma}^{\pm} = \mathbb{C}^{\pm}\boldsymbol{\epsilon}^{\pm}$ and $\boldsymbol{\sigma}^I = \mathbb{C}^I(x_1)\boldsymbol{\epsilon}^I$, whereby $\mathbb{C}^{\pm}$ is the fourth-order elasticity tensor of the domains $\Omega^{\pm}$, and $\mathbb{C}^I(x_1)$ is the fourth-order elasticity tensor of the interphase Ω^I, which varies with respect to the x_1-direction.

3.2.2 Equivalent interface model

This section introduces the equivalent model based on surface elasticity, in which the finite thickness heterogeneous interphase is replaced by specific interface conditions. To this end, kinetic and potential energy densities of the interphase, T^I and U^I from Eq. (3.3), are now substituted by surface energy densities. The action functional $\mathcal{A}$ for the equivalent system can thus be defined in a similar manner as in Sect. 3.2.1,

$$\mathcal{A} = \int_{\Omega\times(0,t_f)} \left[T^{+} + T^{-} - U^{+} - U^{-}\right] dA + \int_{\partial\Omega\times(0,t_f)} \left[T^{S} - U^{S}\right] dS, \tag{3.5}$$

where $\partial\Omega$ is the mid-surface of the domain Ω^I and dS represents the differential surface element, so that

$$T^S = \int_{-\frac{h}{2}}^{x_l} T^I dx_1 + \int_{x_l}^{\frac{h}{2}} T^I dx_1 \quad \text{and} \quad U^S = \int_{-\frac{h}{2}}^{x_l} U^I dx_1 + \int_{x_l}^{\frac{h}{2}} U^I dx_1, \tag{3.6}$$

where $-\frac{h}{2} < x_l < \frac{h}{2}$. Owing to the continuity of displacements at the boundaries, we can state that $\mathbf{u}^I(-\frac{h}{2}) = \mathbf{u}^-(-\frac{h}{2})$ and $\mathbf{u}^I(\frac{h}{2}) = \mathbf{u}^+(\frac{h}{2})$, where, for the sake of conciseness, the dependence of the fields on the spatial coordinates x_2 and x_3, as well as on time t, is dropped. We furthermore assume that the integrals in Eq. (3.6) are quadratic forms of the displacement and velocity fields evaluated on the x_2x_3-plane for x_1 equal to $-\frac{h}{2}$, x_l or $\frac{h}{2}$. Altogether, these hypotheses allow deriving a general form for the surface energy densities as,

$$T^S = \frac{1}{2}\left[\boldsymbol{m}^+\dot{\mathbf{u}}^+.\dot{\mathbf{u}}^+ + \boldsymbol{m}_l\dot{\mathbf{u}}_l.\dot{\mathbf{u}}_l + \boldsymbol{m}^-\dot{\mathbf{u}}^-.\dot{\mathbf{u}}^- + 2\boldsymbol{\gamma}_1\dot{\mathbf{u}}^-.\dot{\mathbf{u}}_l + 2\boldsymbol{\gamma}_2\dot{\mathbf{u}}_l.\dot{\mathbf{u}}^+\right], \tag{3.7}$$

$$U^S = \frac{1}{2}\boldsymbol{K}_1\left[\mathbf{u}_l - \mathbf{u}^-\right].\left[\mathbf{u}_l - \mathbf{u}^-\right] + \frac{1}{2}\boldsymbol{K}_2\left[\mathbf{u}^+ - \mathbf{u}_l\right].\left[\mathbf{u}^+ - \mathbf{u}_l\right], \tag{3.8}$$

where $\mathbf{u}_l = \mathbf{u}^I(x_l)$. Note that, by abuse of notation, we dropped the dependence on space for all displacements. These surface energy densities, which are concentrated in the mid-surface $\partial\Omega$ between the domains Ω^+ and Ω^-, can be interpreted by means of the generalized spring-mass system depicted in Fig. 3.3. Within this frame, the second-order tensors $\boldsymbol{m}^\pm$ and $\boldsymbol{m}_l$ represent masses concentrated at both sides of the interface and at position x_l, respectively; the second-order tensors $\boldsymbol{K}_1$ and $\boldsymbol{K}_2$ represent surface stiffnesses; and finally the second-order tensors $\boldsymbol{\gamma}_1$ and $\boldsymbol{\gamma}_2$ account for the kinetic interactions between the displacement fields.

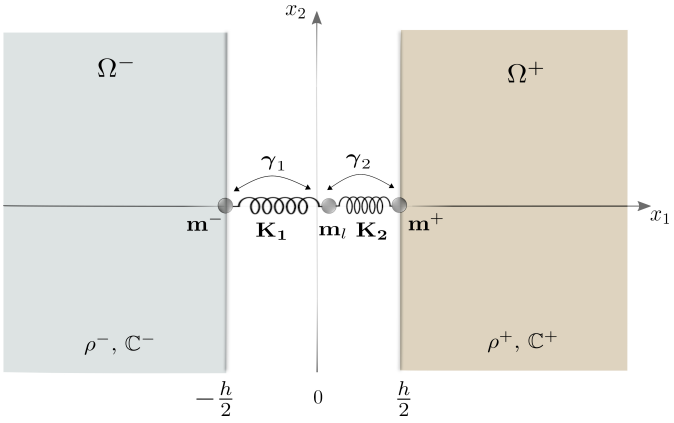

Figure 3.3 – Modeling configuration of the equivalent model with specific interface conditions. The generalized spring-mass system illustrates the role played by the additional degree-of-freedom l to account for the dynamic interactions across the interphase.

It is worth pointing out that, in the most general case, all these constitutive tensors are function of space and time (or frequency in the harmonic regime). Nevertheless, for the model to be exploitable, *i.e.*, to link these tensors to the physical characteristics of the interface rather than to its dynamic properties, a possibility is to turn them into constants. Here the calculation of these tensors will be achieved by selecting specific profiles for the

displacement and velocity fields across the interphase, $\mathbf{u}^I(x_1)$ and $\dot{\mathbf{u}}^I(x_1)$, which fulfill the aforementioned constraints at the location x_1 given by the values $-\frac{h}{2}$, x_l or $\frac{h}{2}$. The natural consequence of this choice is that all surface energy terms will be considered as approximations only.

Again, the variation of the action $\delta\mathcal{A}$ should verify that $\delta\mathcal{A} = 0$, thus leading to the following boundary value problem,

$$\begin{cases} \nabla.\boldsymbol{\sigma}^{\pm} - \rho^{\pm}\ddot{\mathbf{u}}^{\pm} = \mathbf{0}, \quad \forall M \in \Omega^{\pm} \\ \boldsymbol{\sigma}^{-}\mathbf{n}^{-} - \boldsymbol{K}_1(\mathbf{u}_l - \mathbf{u}^{-}) + \boldsymbol{m}^{-}\ddot{\mathbf{u}}^{-} + \boldsymbol{\gamma}_1\ddot{\mathbf{u}}_l = \mathbf{0} \\ \boldsymbol{\sigma}^{+}\mathbf{n}^{+} + \boldsymbol{K}_2(\mathbf{u}^{+} - \mathbf{u}_l) + \boldsymbol{m}^{+}\ddot{\mathbf{u}}^{+} + \boldsymbol{\gamma}_2\ddot{\mathbf{u}}_l = \mathbf{0} \\ \boldsymbol{K}_1(\mathbf{u}_l - \mathbf{u}^{-}) - \boldsymbol{K}_2(\mathbf{u}^{+} - \mathbf{u}_l) + \boldsymbol{m}_l\ddot{\mathbf{u}}_l + \boldsymbol{\gamma}_1\ddot{\mathbf{u}}^{-} + \boldsymbol{\gamma}_2\ddot{\mathbf{u}}^{+} = \mathbf{0} \end{cases} \tag{3.9}$$

where the first equation retains the same form than that of Eq. (3.4), whereas the other three now account for the specific interface conditions, in which, by abuse of notation, the stress tensors are now stated as $\boldsymbol{\sigma}^{-} = \boldsymbol{\sigma}^I\left(-\frac{h}{2}\right)$ and $\boldsymbol{\sigma}^{+} = \boldsymbol{\sigma}^I\left(\frac{h}{2}\right)$. It should be noted that this boundary value problem could be easily implemented in a standard FE code, as it only involves a modification of the boundary conditions.

3.2.3 Pressure plane wave propagation under normal incidence

We now consider the problem of a plane elastic wave propagating under normal incidence across the considered functionally graded interphase. In this way, our modeling approach is reduced to an incident and a reflected longitudinal bulk wave in the domain Ω^{-} and a transmitted longitudinal bulk wave in the domain Ω^{+}. By assuming a general harmonic solution for the interphase Ω^I, the general solution for a plane wave propagating along the x_1-direction reads as

$$\begin{array}{rcl} u^{-}(x_1,t) & = & \left(A_i \exp\left(jk_p^{-}x_1\right) + A_r \exp\left(-jk_p^{-}x_1\right)\right)\exp\left(-j\omega t\right) \\ u^{+}(x_1,t) & = & A_t \exp\left(j(k_p^{+}x_1 - \omega t)\right) \\ u^{I}(x_1,t) & = & g(x_1)\exp(-j\omega t) \end{array} , \tag{3.10}$$

where ω represents the angular frequency and j is the unit imaginary number. The variable $k_p^{\pm} = \omega/c_p^{\pm}$ denotes the wave number, which depends upon the longitudinal bulk wave velocity $c_p^{\pm}$ in the domain $\Omega^{\pm}$. The variables A_i, A_r and A_t denote the amplitudes of the incident, reflected and transmitted plane waves, respectively. The function $g(x_1)$ represents the unknown amplitude of the harmonic solution in the interphase, which accounts for the material heterogeneity along the x_1-direction. Substituting the wave solutions from Eq. (3.10) into the boundary value problem from Eq. (3.4), and working through these analytical equations to remove the variables A_r and A_t, yield the following boundary value problem for the function $g(x_1)$ in strong form,

$$\begin{cases} \left(C_{11}^I(x_1)g_{,1}(x_1)\right)_{,1} + \omega^2\rho^I(x_1)g(x_1) = 0 \\ C_{11}^I\left(-\frac{h}{2}\right)g_{,1}\left(-\frac{h}{2}\right) + jk_p^{-}C_{11}^{-}g\left(-\frac{h}{2}\right) - 2jk_p^{-}C_{11}^{-}A_i\exp\left(-jk_p^{-}\frac{h}{2}\right) = 0 \\ C_{11}^I\left(\frac{h}{2}\right)g_{,1}\left(\frac{h}{2}\right) - jk_p^{+}C_{11}^{+}g\left(\frac{h}{2}\right) = 0 \end{cases} , \tag{3.11}$$

where the derivative with respect to x_1 is denoted by $(_{,1})$ and C_{11} is the stiffness coefficient along the x_1-direction (in Voigt notation) associated with each domain. The first relation of Eq. (3.11) is an ordinary differential equation with respect to the coordinate x_1, whereas the two last relations account for the boundary conditions at positions $x_1 = -\frac{h}{2}$ and $x_1 = \frac{h}{2}$, respectively. Note that such boundary value problem in strong form must be solved numerically.

In the same vein, the boundary value problem associated with the equivalent interface model (recall Eq. (3.9)) can be simplified as follows in the case of a pressure plane wave under normal incidence,

$$\begin{cases} C_{11}^{\pm} u_{,11}^{\pm} - \rho^{\pm} \ddot{u}^{\pm} = 0, \qquad \forall M \in \Omega^{\pm} \\ C_{11}^{-} u_{,1}^{-} - K_1 (u_l - u^-) + m^- \ddot{u}^- + \gamma_1 \ddot{u}_l = 0 \\ -C_{11}^{+} u_{,1}^{+} + K_2 (u^+ - u_l) + m^+ \ddot{u}^+ + \gamma_2 \ddot{u}_l = 0 \\ K_1 (u_l - u^-) - K_2 (u^+ - u_l) + m_l \ddot{u}_l + \gamma_1 \ddot{u}^- + \gamma_2 \ddot{u}^+ = 0 \end{cases}, \tag{3.12}$$

where it should be noted that the second-order tensors of the surface energy terms are now all reduced to scalar coefficients. Furthermore, we hypothesize that the general solution for the displacement in the interface can be stated as

$$u_l(t) = B \exp(-j\omega t), \tag{3.13}$$

where B represents the unknown amplitude of the harmonic solution in the interface. Substituting Eq. (3.13), along with the wave solutions associated with the surrounding domains $\Omega^{\pm}$ from Eq. (3.10), into the boundary value problem from Eq. (3.12) leads to the following linear equation system

$$\begin{pmatrix} -jk_p^- C_{11}^- + K_1 - \omega^2 m^- & -K_1 - \omega^2 \gamma_1 & 0 \\ 0 & -K_2 - \omega^2 \gamma_2 & -jk_p^+ C_{11}^+ + K_2 - \omega^2 m^+ \\ -K_1 - \omega^2 \gamma_1 & K_1 + K_2 - \omega^2 m_l & -K_2 - \omega^2 \gamma_2 \end{pmatrix} \begin{bmatrix} A_r \\ B \\ A_t \end{bmatrix} = \begin{pmatrix} -\left(jk_p^- C_{11}^- + K_1 - \omega^2 m^-\right) A_i \\ 0 \\ \left(K_1 + \omega^2 \gamma_1\right) A_i \end{pmatrix}, \tag{3.14}$$

whose solution allows determining the unknown amplitudes, A_r and A_t, of the reflected and transmitted waveforms. Note that, in contrast to the boundary value problem associated with the reference interphase model (recall Eq. (3.11)), the resulting system for the equivalent interface can be solved analytically.

3.2.4 Identification of the equivalent model coefficients

This section presents the adopted strategy for identifying the coefficients of the surface kinetic and internal energy densities, *i.e.*, m^-, m_l, m^+, γ_1, γ_2, K_1, and K_2. Towards this goal, we hypothesize that the displacement field is directed towards the surface normal, *i.e.*, $\mathbf{u}^I = u^I(x_1)\,\mathbf{e}_1$, and that it can be approximated using a piece-wise affine profile with respect to the coordinate x_1 (see Fig. 3.4).

In such a case, the kinetic and potential energy densities across the interphase (recall Eq. (3.3)) can be written as

$$T^I = \frac{1}{2} \int_{-\frac{h}{2}}^{\frac{h}{2}} \rho^I(x_1) \left(v^I(x_1)\right)^2 dx_1 \quad \text{and} \quad U^I = \frac{1}{2} \int_{-\frac{h}{2}}^{\frac{h}{2}} C_{11}^I(x_1) \left(u_{,1}^I(x_1)\right)^2 dx_1, \tag{3.15}$$

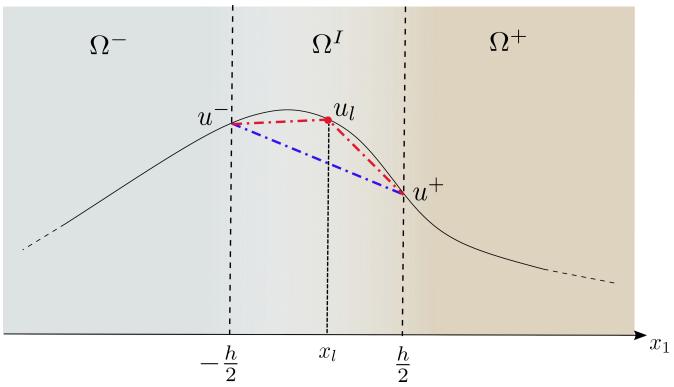

Figure 3.4 – Illustration of the displacement field across the interphase for an arbitrarily selected frequency: Comparison between the exact profile (continuous black line) used in the reference model and the piece-wise affine profile (dashed red line) used in the equivalent interface model. The affine profile (dashed blue line) proposed in [38] is shown for comparison.

where

$$u^I(x_1) = \begin{cases} \left(\dfrac{2\,(u_l - u^-)}{h + 2x_l}\right) x_1 + \left(\dfrac{u_l h + 2u^- x_l}{h + 2x_l}\right) & \text{for} \quad -\frac{h}{2} < x_1 < x_l \\ \left(\dfrac{2\,(u^+ - u_l)}{h - 2x_l}\right) x_1 - \left(\dfrac{2u^+ x_l - u_l h}{h - 2x_l}\right) & \text{for} \quad x_l < x_1 < \frac{h}{2} \end{cases}, \tag{3.16}$$

in which u^-, u_l and u^+ are the values of the displacement field $u^I(x_1)$ at the location x_1 given by the values $-\frac{h}{2}$, x_l or $\frac{h}{2}$. Note that, since we assumed a general harmonic solution for the displacement field in the interphase, the velocity field $v^I(x_1)$ will have the same piece-wise form, modulo the constant complex factor $j\omega$, than that of Eq. (3.16), with v^-, v_l and v^+ being the values of the velocity field at the location x_1 given by the values $-\frac{h}{2}$, x_l or $\frac{h}{2}$. According to the pressure plane wave assumption, the kinetic and potential energies per unit surface, T^S and U^S, can now be written as

$$\begin{aligned} T^S &= \frac{1}{2}\left[m^+(v^+)^2 + m_l(v_l)^2 + m^-(v^-)^2 + 2\gamma_1 v^- v_l + 2\gamma_2 v_l v^+\right], \\ U^S &= \frac{1}{2}K_1\,(u_l - u^-)^2 + \frac{1}{2}K_2\,(u^+ - u_l)^2, \end{aligned} \tag{3.17}$$

where the necessary conditions for the kinetic energy density, T^S, to be a positive definite quadratic form are that $m^\pm > 0$, $\gamma_2^2 < \frac{1}{2}m^+ m_l$, and $\gamma_1^2 < \frac{1}{2}m^- m_l$. By inserting the displacement and velocity fields, $u^I(x_1)$ and $v^I(x_1)$, into Eq. (3.15), the outcome can then be compared to Eq. (3.17) by making use of the relations defined in Eq. (3.6), thus allowing for the identification of the coefficients belonging to the surface kinetic and

potential energy densities T^S and U^S as

$$\begin{aligned}
m^- &= 4\int_{-\frac{h}{2}}^{x_l} \rho_I(x_1)\left(\frac{x_1-x_l}{h+2x_l}\right)^2 dx_1 \\
m^+ &= 4\int_{x_l}^{\frac{h}{2}} \rho_I(x_1)\left(\frac{x_1-x_l}{h-2x_l}\right)^2 dx_1 \\
m_l &= \int_{-\frac{h}{2}}^{x_l} \rho_I(x_1)\left(\frac{h+2x_1}{h+2x_l}\right)^2 dx_1 + \int_{x_l}^{\frac{h}{2}} \rho_I(x_1)\left(\frac{h-2x_1}{h-2x_l}\right)^2 dx_1 \\
\gamma_1 &= 2\int_{-\frac{h}{2}}^{x_l} \rho_I(x_1)\frac{(h+2x_1)(-x_1+x_l)}{(h+2x_l)^2} dx_1 \\
\gamma_2 &= 2\int_{x_l}^{\frac{h}{2}} \rho_I(x_1)\frac{(h-2x_1)(x_1-x_l)}{(h-2x_l)^2} dx_1 \\
K_1 &= \frac{1}{x_l^2}\int_{-\frac{h}{2}}^{x_l} C_{11}^I(x_1) dx_1 \\
K_2 &= \frac{1}{(h-x_l)^2}\int_{x_l}^{\frac{h}{2}} C_{11}^I(x_1) dx_1.
\end{aligned} \tag{3.18}$$

In our earlier study [38], the equivalent interface model was associated with an affine displacement field (dashed blue line in Fig. 3.4). To serve as a comparison with Eqs. (3.17)-(3.18), the related expressions for the kinetic and potential energy densities per unit surface, along with the identified coefficients, are briefly recalled in A.1.

3.3 Numerical results

The performance of the proposed enriched model is assessed by evaluating the frequency-dependent reflection coefficient in a reflection/transmission problem between two homogeneous solid half-spaces, which are separated by a finite thickness and heterogeneous interphase. First, we identify the specific surface properties of the equivalent interface by comparison with the reference interphase. Second, we perform an optimization procedure to investigate the impact of the position x_l of the additional degree-of-freedom on the modeling performance. The optimal equivalent model is subsequently compared to different baselines.

Towards these goals, we consider here an interphase whose stiffness and density vary along the x_1-direction. This configuration is inspired by our recent multiscale modeling results [39], which showed that the tendon-to-bone interphase can be seen as a continuous functionally graded material. The selected model parameters for the two surroundings tissues, *i.e.*, tendon Ω^- and bone Ω^+, together with the finite thickness h of the interphase, are summarized in Tab. 3.1.

Mass density (g.cm^{-3})		Stiffness coefficient (GPa)		Thickness (μm)
ρ^-	ρ^+	C_{11}^-	C_{11}^+	h
1.22	1.88	4.37	27.48	300

Table 3.1 – Model parameters for the two surroundings tissues $\Omega^\pm$ and the interphase Ω^I.

The gradients in mechanical properties across the interphase Ω^I, which are used as further input in the reference model, are depicted in Fig. 4.2. The effective stiffness variation at the mesoscale is the result of competing gradients in mineral content and collagen fibers organization at lower length scales. Indeed, it has been shown that the linear increase in mineral content caused a stiffening of the interphase that became significant beyond a certain percolation threshold (approximately located between $0 - 50$ μm in Fig. 4.2a), whereas the decreasing collagen fiber organization across the interphase led to a reduced tissue stiffness along the main fibers direction [14, 39]. In contrast, the effective mass density evolves linearly between the two surrounding tissues (see Fig. 4.2b).

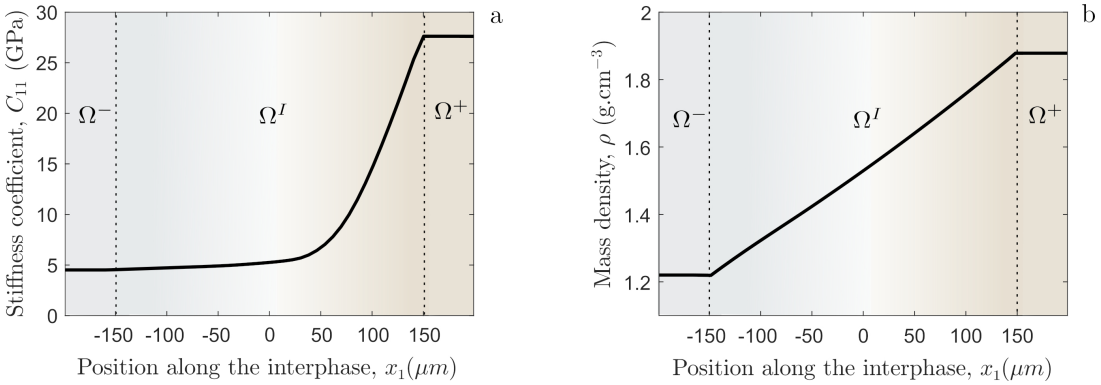

Figure 3.5 – Graded mechanical properties across the tendon-to-bone interphase: (a) effective stiffness coefficient C_{11} and (b) effective mass density ρ. These trends are based upon the multiscale model reported in [39].

3.3.1 Evaluation of the equivalent interface model

To validate the proposed equivalent interface model, we first evaluate the reflection coefficient $R = |A_r/A_i|^2$ as a function of frequency, in which the amplitude A_i of the incident plane wave was set to unity. For a better interpretation, the reflection coefficient R was calculated as well as a function of the ratio between the average wavelength $\bar{\lambda}$ and the thickness h of the interphase. The average wavelength $\bar{\lambda}$ was defined as

$$\bar{\lambda} = \frac{\bar{c}_p^I}{f}, \quad \text{with } \bar{c}_p^I = \sqrt{\frac{\bar{C}_{11}^I}{\bar{\rho}^I}}, \tag{3.19}$$

where $\bar{c}_p^I$, $\bar{C}_{11}^I$ and $\bar{\rho}^I$ are the average phase velocity, the average stiffness and the average mass density, respectively.

The reference model from Eq. (3.11) is solved using a standard FE code such as Comsol Multiphysics®, from which the reflection coefficient, R^{ref} can be derived as

$$R^{\text{ref}} = \left|\frac{A_r}{A_i}\right|^2 = \left|\frac{g\left(-\frac{h}{2}\right) - A_i \exp\left(-jk_p^- \frac{h}{2}\right)}{A_i \exp\left(jk_p^- \frac{h}{2}\right)}\right|^2. \tag{3.20}$$

In contrast, the reflection coefficient associated with the equivalent interface model can be calculated analytically using Eq. (3.14). Note, however, that this enriched modeling

approach now depends upon the position of the additional degree-of-freedom x_l, whose optimal location is *a priori* not known. To serve as an example, the coefficients of the kinetic and potential energy densities were first calculated for two arbitrarily selected values of x_l using Eq. (3.18). The numerical results are depicted in Fig. 3.6, in which the proposed model (dashed red line) with different values of x_l is compared to the reference interphase model (continuous black line), to a homogeneous interphase Ω^I with averaged mechanical properties (dashed gray line), and to an abrupt transition (continuous gray line) corresponding to the case where the surroundings tissues $\Omega^{\pm}$ are placed directly in contact. As can be observed in the enlargement of Fig. 3.6, for a low frequency regime

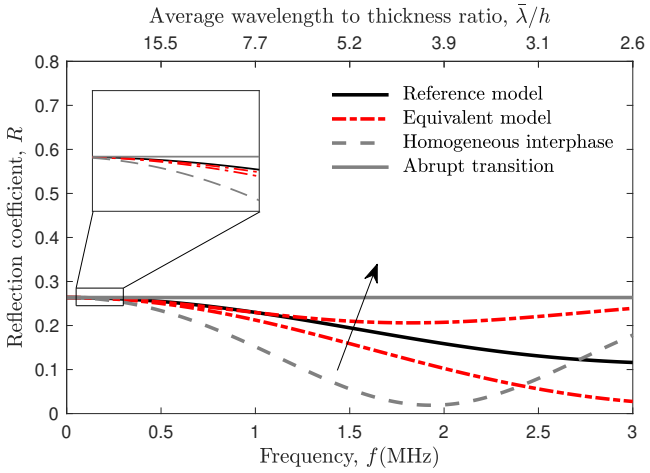

Figure 3.6 – Frequency-dependent reflection coefficient R obtained using: (1) the reference model (continuous black line); (2) a homogeneous interphase (dashed gray line); (3) an abrupt transition (continuous gray line); and (4) the equivalent interface model (dashed red lines) for two arbitrarily selected values of x_l equal to -50 and 50 μm. The black arrow indicates the resulting trend with respect to increasing values of x_l.

below 0.3 MHz (*i.e.*, high ratio $\bar{\lambda}/h$), the equivalent interface model satisfactorily captures the dynamics of the reference model, independently of the position of the additional degree-of-freedom x_l. At an intermediate frequency regime around 0.3–2.5 MHz, the choice of x_l has a significant impact on the ability of our model to match the reference one, and thus account for the gradient in mechanical properties, which in turn reflect microstructural features at lower length scales. As expected, when the ratio of the average wavelength to the interphase thickness decreases towards values below 3, the deviation from the reference model increases, and our approximated model fails in capturing the complex dynamics of the interphase, which is associated with stronger wave-interphase interactions. Nonetheless, it is worth mentioning that, overall, the deviation of this model from the reference ones is much lower than that obtained using a simple abrupt transition or a homogeneous interphase with averaged mechanical properties, which represent the commonly used baselines in FE simulations at the organ scale [43–45].

3.3.2 Optimization of the equivalent interface model

Second, an optimization procedure was conducted to further investigate the impact of the additional degree-of-freedom position x_l on the performance of the proposed model.

To this end, the relative cumulative error on the reflection coefficient (denoted by err) between the one of the reference model (denoted by R^{ref}) and the one of the equivalent interface model (denoted by R) was calculated by sweeping the frequency and the position of x_l across the interphase as

$$\text{err}(x_l, f) \quad = \quad \frac{1}{N_{\text{max}}} \sum_{n=1}^{N_{\text{max}}} \left(\frac{R^{\text{ref}}(f_n) - R(x_l, f_n)}{R^{\text{ref}}(f_n)} \right)^2, \tag{3.21}$$

where N_{max} is an integer value corresponding to the maximal frequency position. Figure 3.7a represents the dynamics of the error as a function of the position of x_l and the frequency f. As can be observed, at a low frequency regime below 0.3 MHz, the equivalent

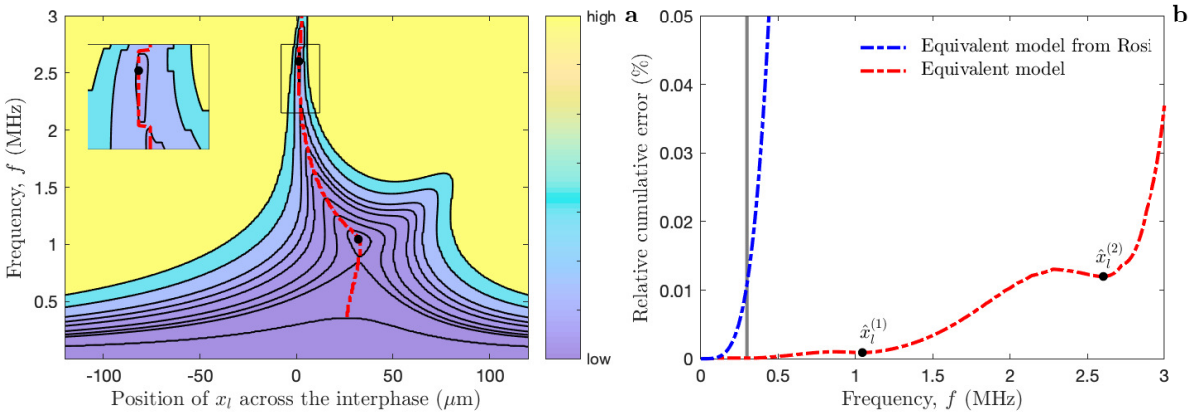

Figure 3.7 – (a) Relative cumulative error on the reflection coefficient (Eq. (3.21)) between the one of the reference model and the one of the equivalent interface model as a function of the frequency and the position of the additional degree-of-freedom x_l across the interphase. The dashed red line represents the optimal x_l-path as a function of the frequency, whereas the black dots depict the local minima $x_l^{(1)}$ and $x_l^{(2)}$. The region around the second local minima is displayed in the insert. (b) Relative cumulative error along the optimal x_l-path as a function of the frequency (dashed red line). The error between the reference model and the model presented in [38] is shown for comparison (dashed blue line). The gray line represents the frequency threshold (0.3 MHz) below which the error is independent of the position x_l.

interface model provides an accurate approximation of the reference model independently of the position of the additional degree-of-freedom x_l. Towards higher frequencies, the performance of the equivalent model slightly decreases, but there is a specific path along x_l (displayed as a dashed red line) for which the error remains reasonably low. Interestingly, there are two local minima located at around 1 and 2.6 MHz along this path (black dots), for which the optimal values of $\hat{x}_l$ are equal to 32 and 1.2 μm, respectively (*i.e.*, thicknesses that fall within the range corresponding to the percolation threshold in Fig. 4.2a). A more advanced insight is provided in Fig. 3.7b, which depicts the relative cumulative error along the optimal x_l-path as a function of the frequency, thus clearly highlighting the presence of two local minima, *i.e.*, $x_l^{(1)}$ and $x_l^{(2)}$. It is worth mentioning that the error associated with $x_l^{(2)}$ at 2.6 MHz is of the same order than that obtained using the model from [38] at 0.3 MHz (low frequency regime represented as a continuous gray line). Therefore, fine-tuning the position of the additional degree-of-freedom x_l in

our modeling approach allows enlarging nearly 8 times the validity range with respect to that model.

To further assess the performance of our enriched model, Fig. 3.8 now depicts the obtained frequency-dependent reflection coefficient R for the optimal position $x_l^{(2)}$ (dashed red line), which is compared to the reference model (continuous black line), an abrupt transition (continuous gray line), the equivalent model from [38] (dashed blue line) and an equivalent model possessing only elastic properties (dotted red line), that is to say non-inertial interface conditions (*i.e.*, $m^+ = m^- = m_l = 0$ kg.m^{-2} and $\gamma_1 = \gamma_2 = 0$ kg.m^{-2}). As expected from the optimization, our equivalent model with specific interface

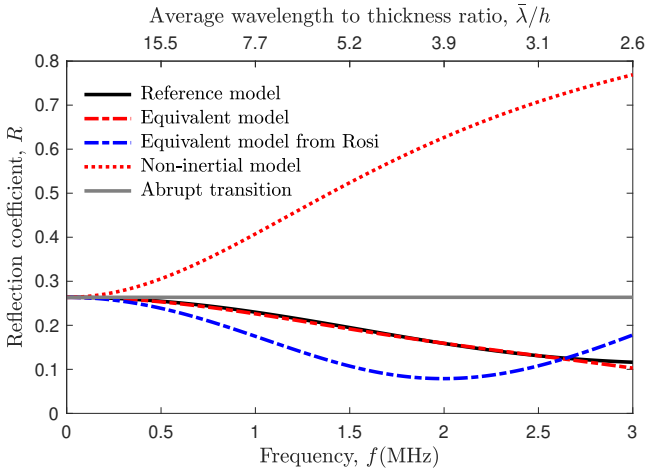

Figure 3.8 – Frequency-dependent reflection coefficient R obtained using: (1) the reference model (continuous black line); (2) an abrupt transition (continuous gray line); (3) a non-inertial equivalent interface model (dotted red line); (4) the model (dashed blue line) associated with a displacement field with an affine profile (Ref. [38]); and (5) the equivalent interface model (dashed red lines) for an optimal value of x_l equal to 1.2 μm.

conditions provides a very accurate approximation of the reference model over a broad frequency range up to around 2.6 MHz. It thus outperforms the results obtained with the equivalent model from [38], which still remains valid but for a much narrower frequency regime. In contrast, an equivalent model that only accounts for elastic interface conditions totally fails in capturing the complex dynamics of the interphase.

3.4 Discussion

Computational modeling of functionally graded intephases between soft and hard materials has provided important insights on underlying anchoring mechanisms at the microscale and on surgical repair strategies at the macroscale. To unravel additional mechanical characteristics related to the functioning of such complex interphases, as well as to enhance the characterization of bioinspired attachment procedures or tissue engineered implants, current models should include a precise description of the graded mechanical behavior of the interphase across several length scales. However, such modeling strategy raises several challenges from a computational viewpoint, especially in the case of dynamic loading.

In this study, we proposed an equivalent model based on surface elasticity, in which the finite thickness, continuous functionally graded interphase between the tendon and bone can be substituted by a zero-thickness interface. This was achieved by replacing the kinetic and potential energies of the interphase by specific surface energy density terms, whose coefficients could be identified in a straightforward manner using known profiles for the effective stiffness and density across the interphase. With respect to previously reported models, this novel formulation introduces an additional degree-of-freedom, which allows for a more refined description of the mechanical fields (*e.g.*, displacements and velocities) across the interphase. The performance of the model was evaluated in the context of wave propagation.

The main findings from this numerical study were as follows: (1) as the performance of enriched models generally depends upon a proper selection of the kinematics across the interphase, our numerical results showed that the displacement field could be adequately modeled as a two-piece profile associated with an additional degree-of-freedom; (2) the assessment of the frequency-dependent reflection coefficient showed that our optimized enriched model can provide a very accurate approximation of the reference model over a broad frequency range up to around 2.6 MHz, thus outperforming the results obtained with more simplistic models; and (3) this model has a much lower computational cost than the reference one, as the interphase must not be incorporated (*i.e.*, meshed) explicitly. Overall, our numerical results showed that the proposed approach is well-suited for the solution of a complete elastodynamics problem in the frequency-domain, as it captures the complex mechanical behavior of the tendon-to-bone interphase over a broad frequency range. Interestingly, all these significant outcomes are reached based on the optimal position of the additional degree-of-freedom, whose choice may depend on several parameters, among which the underlying behavior of the gradient in mechanical properties across the interphase is thought to be a determinant factor.

To test this hypothesis, we also investigated the impact of microstructural *damage* at the tendon-bone interphase on the optimal position of the additional degree-of-freedom (see Fig. 3.9). Clinical burden related to physical overloading, disuse or systemic diseases

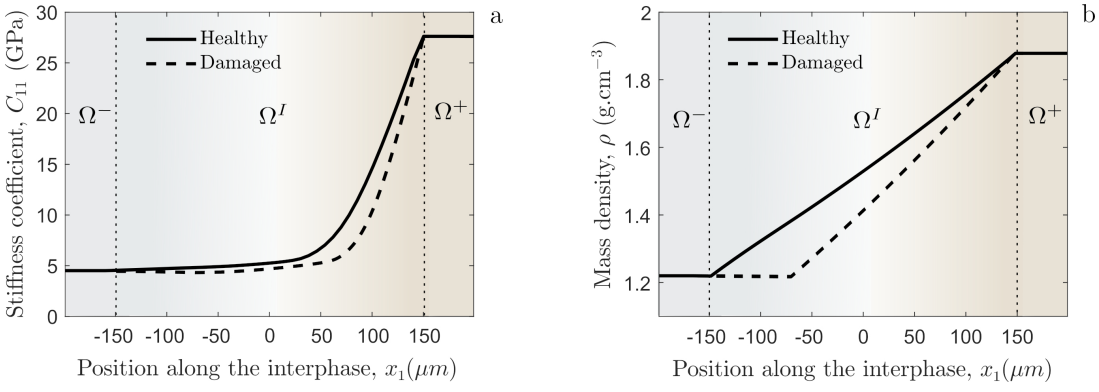

Figure 3.9 – Graded mechanical properties across the tendon-to-bone interphase representative of a damaged configuration (dashed lines): (a) effective stiffness coefficient C_{11} and (b) effective mass density ρ. The nominal case from Fig. 4.2 is shown for comparison (continuous lines).

may manifest as a delayed onset of mineralization and an increasing angular deviation from the main collagen fibers direction across the tendon-to-bone insertion [46–48], which

in turn lead to modified graded mechanical properties at the macroscale [14, 39]. A can be observed, for such a damaged configuration the gradient in stiffness displays a slightly shifted percolation threshold with respect to the nominal case (see Fig. 3.9a), whereas the gradient in mass density now has a piece-wise profile (see Fig. 3.9b).

Using these modified graded profiles as input of our enriched model and applying the optimization procedure described in Subsect. 3.3.2 yield different values for the optimal position $\hat{x}_l$ and for the identified coefficients associated with the surface energy density terms (see Tab. 3.2). Interestingly, the optimal position $\hat{x}_l$ has now raised to around 9 μm with respect to its nominal value, and this shift is of the same order than that related to the percolation threshold observed in the stiffness profile (see Fig. 3.9a). Beside the shift of $\hat{x}_l$, the identified coefficients are also impacted, but their interpretation is not straightforward and we postpone this analysis to future works. Nevertheless, our model

Case	Position $\hat{x}_l$ μm	Surface mass densities m^-	m^+ kg.m^{-2}	m_l	Kinetic interactions γ_1	γ_2 kg.m^{-2}	Surface stiffnesses K_1	K_2 kg.(s.m)$^{-2}$ $\times 10^{13}$
Healthy	1.2	0.0653	0.0881	0.1525	0.0346	0.0418	3.08	8.05
Damaged	10.3	0.0658	0.0818	0.1427	0.0339	0.0384	2.72	7.57

Table 3.2 – Comparison between the optimal positions of the additional degree-of-freedom and the coefficients of the enriched model for the healthy and damaged cases.

proves to be sensitive to slight changes of the graded properties across the interphase (see Fig. 3.10) and could potentially be used for characterization purposes.

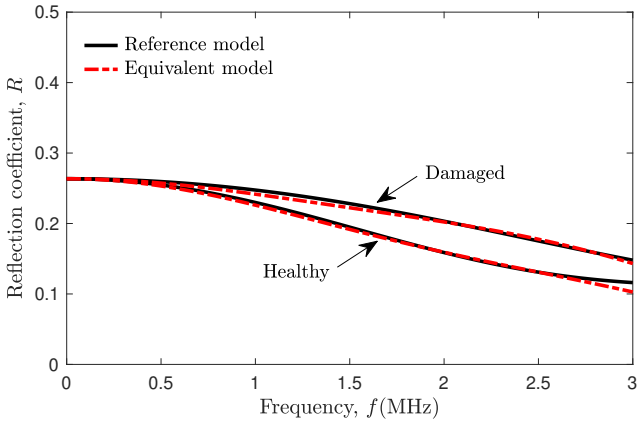

Figure 3.10 – Comparison between the reference model (continuous black lines) and the optimal equivalent interface model (dashed red lines) for two different gradients in mechanical properties across the tendon-to-bone interphase (recall Fig. 3.9).

Although the proposed enriched framework was established to account for a general 3-D formulation, the investigated configuration was subsequently reduced to the rather simple case of a plane elastic wave propagating under normal incidence across a functionally graded interphase, whose mechanical properties vary with respect to a single direction only. In a such case, the reflection/transmission problem is limited to the analysis of longitudinal bulk waves. Therefore, to further tackle the complexity of the tendon-to-bone

attachment, whose geometry, for instance at the Achilles tendon, is characterized by a shallow attachment angle and an optimized shape of the outward splay, as well as by interdigitation mechanisms (recall Fig. 3.1a–b) [49, 50], future modeling efforts should consider 2-D geometries using plane wave propagating under oblique incidence (*i.e.*, both longitudinal and shear waves) or surface waves [51]. As a further drawback, the performance of the enriched model was here only assessed based on the analysis of the frequency-dependent reflection coefficient, thus only displaying information on the amplitude spectrum of the propagating waves. However, the phase of the waves plays a crucial role as well, especially for the analysis of time-domain signals traveling across thin interphases. Further studies are warranted to precisely address the impact of the equivalent modeling approach on the phase spectrum. Overall this modeling approach represents the first critical step towards the development of more sophisticated models targeting mechanical strategies for improving diagnostic and reattachment procedures, which will not only be valuable for evaluating the tendon-to-bone insertion, but also other multiscale and graded biological attachments such as the bone-implant interphase [52, 53] and new generations of engineered composite materials [54].

3.5 Conclusion

The original equivalent interface model presented in this study aimed at mimicking the elastodynamic behavior of a finite heterogeneous interphase, while reducing the overall computational burden related to the consideration of its complete geometry. It has been shown that, in the case of a dynamic experiment, *i.e.*, plane pressure waves under normal incidence, the proposed enriched model remains valid over a broad frequency range and outperforms more simplistic models that typically serve as a baseline in FE simulations at the organ scale. The key feature of the model was the introduction of an additional degree of freedom in the interface, which allowed for a finer description of the kinematic fields within the interphase that accounted for both its inertial behavior and the kinetic interactions with the surrounding media. Furthermore, it has been shown that the model was sensitive to slight variations of the graded mechanical properties across the interphase, thus opening potential applications in the field of nondestructive testing and characterization. Finally, it should be noted that such modeling approach is straightforwardly extendable to account for more complex interphase geometries.

Acknowledgements

This work was partially funded by the BEST-AMUS project (IIN program, CNRS-INSIS), the “Support for research for newly appointed Associate Professors” and the “Bonus Qualité Recherche” (Faculté des Sciences et Technologie, Université Paris-Est Créteil).

Appendix

A.1 Equivalent interface model used for comparison

Here we briefly recall the underlying equations of the equivalent interface model introduced in [38]. In that study, the displacement field was associated with an affine profile. As such, the general forms for the kinetic and potential energies per unit surface were stated as

$$T^S = \frac{1}{2}\left[m^+(v^+)^2 + m^-(v^-)^2 + 2\gamma v^+ v^-\right], \tag{A.1}$$

$$U^S = \frac{1}{2}K\left(v^+ - v^-\right).\left(v^+ - v^-\right), \tag{A.2}$$

where the coefficients to be identified are

$$m^\pm = \frac{M_0}{4} \pm \frac{M_1}{h} + \frac{M_2}{h^2}, \quad \gamma = \frac{M_0}{4} - \frac{M_2}{h^2}, \tag{A.3}$$

in which M_α represents the α-th order moment of the density profile of the interphase

$$M_\alpha = \int_0^h x_1^\alpha \rho^I(x_1) dx_1, \quad \text{for} \quad \alpha = 0, 1, 2. \tag{A.4}$$

Bibliography

[1] S Thomopoulos, V Birman, and GM Genin. The challenge of attaching dissimilar materials. In *Structural Interfaces and Attachments in Biology*, pages 3–17. Springer, 2013.

[2] A Sola, D Bellucci, and V Cannillo. Functionally graded materials for orthopedic applications–an update on design and manufacturing. *Biotechnol Adv*, 34(5):504–531, 2016.

[3] JWY Jor, MD Parker, AJ Taberner, MP Nash, and PMF Nielsen. Computational and experimental characterization of skin mechanics: identifying current challenges and future directions. *WIRES Syst Biol Med*, 5(5):539–556, 2013.

[4] V Bousson, A Meunier, C Bergot, É Vicaut, MA Rocha, MH Morais, A-M Laval-Jeantet, and J-D Laredo. Distribution of intracortical porosity in human midfemoral cortex by age and gender. *J Bone Miner Res*, 16(7):1308–1317, 2001.

[5] J Apostolakos, TJS Durant, CR Dwyer, RP Russell, JH Weinreb, F Alaee, K Beitzel, MB McCarthy, MP Cote, and AD Mazzocca. The enthesis: a review of the tendon-to-bone insertion. *Muscles Ligaments Tendons J*, 4(3):333, 2014.

[6] MJ Mirzaali, AH de la Nava, D Gunashekar, M Nouri-Goushki, RPE Veeger, Q Grossman, L Angeloni, MK Ghatkesar, LE Fratila-Apachitei, D Ruffoni, EL Doubrovski, and AA Zadpoor. Mechanics of bioinspired functionally graded soft-hard composites made by multi-material 3D printing. *Compos Struct*, page 111867, 2020.

[7] A Tits and D Ruffoni. Joining soft tissues to bone: insights from modeling and simulations. *Bone Rep*, page 100742, 2020.

[8] L Rossetti, LA Kuntz, E Kunold, J Schock, KW Müller, H Grabmayr, J Stolberg-Stolberg, F Pfeiffer, SA Sieber, R Burgkart, and AR Bausch. The microstructure and micromechanics of the tendon–bone insertion. *Nat Mater*, 16(6):664, 2017.

[9] JWC Dunlop, R Weinkamer, and P Fratzl. Artful interfaces within biological materials. *Mater Today*, 14(3):70–78, 2011.

[10] A Seidi, M Ramalingam, I Elloumi-Hannachi, S Ostrovidov, and A Khademhosseini. Gradient biomaterials for soft-to-hard interface tissue engineering. *Acta Biomater.*, 7(4):1441–1451, 2011.

[11] Z Liu, MA Meyers, Z Zhang, and RO Ritchie. Functional gradients and heterogeneities in biological materials: Design principles, functions, and bioinspired applications. *Prog Mater Sci*, 88:467–498, 2017.

[12] E Gracey, A Burssens, I Cambré, G Schett, R Lories, IB McInnes, H Asahara, and D Elewaut. Tendon and ligament mechanical loading in the pathogenesis of inflammatory arthritis. *Nat Rev Rheumatol*, pages 1–15, 2020.

[13] GM Genin, A Kent, V Birman, B Wopenka, JD Pasteris, PJ Marquez, and S Thomopoulos. Functional grading of mineral and collagen in the attachment of tendon to bone. *Biophys J*, 97(4):976–985, 2009.

[14] Y Liu, S Thomopoulos, C Chen, V Birman, MJ Buehler, and GM Genin. Modelling the mechanics of partially mineralized collagen fibrils, fibres and tissue. *J. R Soc Interface*, 11(92):20130835, 2014.

[15] F Saadat, V Birman, S Thomopoulos, and GM Genin. Effective elastic properties of a composite containing multiple types of anisotropic ellipsoidal inclusions, with application to the attachment of tendon to bone. *J Mech Phys Solids*, 82:367–377, 2015.

[16] Y Hu, V Birman, A Deymier-Black, AG Schwartz, S Thomopoulos, and GM Genin. Stochastic interdigitation as a toughening mechanism at the interface between tendon and bone. *Biophys J*, 108(2):431–437, 2015.

[17] YX Liu, S Thomopoulos, V Birman, J-S. Li, and GM Genin. Bi-material attachment through a compliant interfacial system at the tendon-to-bone insertion site. *Mech Mater*, 44:83–92, 2012.

[18] C Quental, J Folgado, J Monteiro, and M Sarmento. Full-thickness tears of the supraspinatus tendon: A three-dimensional finite element analysis. *J Biomech*, 49(16):3962–3970, 2016.

[19] M Mantovani, A Pellegrini, P Garofalo, and P Baudi. A 3D finite element model for geometrical and mechanical comparison of different supraspinatus repair techniques. *J Shoulder Elbow Surg*, 25(4):557–563, 2016.

[20] A Shafiei, JW Pro, R Martini, and F Barthelat. The very hard and the very soft: Modeling bio-inspired scaled skins using the discrete element method. *J Mech Phys Solids*, 146:104176, 2021.

[21] EI Avgoulas, MPF Sutcliffe, SW Linderman, V Birman, S Thomopoulos, and GM Genin. Adhesive-based tendon-to-bone repair: failure modelling and materials selection. *J R Soc Interface*, 16(153):20180838, 2019.

[22] S Kuznetsov, M Pankow, K Peters, and H-Y. S Huang. A structural-based computational model of tendon–bone insertion tissues. *Math Biosci*, 327:108411, 2020.

[23] R Vayron, V-H Nguyen, R Bosc, S Naili, and G Haïat. Finite element simulation of ultrasonic wave propagation in a dental implant for biomechanical stability assessment. *Biomech Model Mechanobiol*, 14(5):1021–1032, 2015.

[24] ME Gurtin and AI Murdoch. A continuum theory of elastic material surfaces. *Arch Ration Mech Anal*, 57(4):291–323, 1975.

[25] P Bövik. On the modelling of thin interface layers in elastic and acoustic scattering problems. *Q J Mech Appl Math*, 47(1):17–42, 1994.

[26] Z Hashin. Thin interphase/imperfect interface in elasticity with application to coated fiber composites. *J Mech Phys Solids*, 50(12):2509–2537, 2002.

[27] Y Benveniste. A general interface model for a three-dimensional curved thin anisotropic interphase between two anisotropic media. *J Mech Phys Solids*, 54(4):708–734, 2006.

[28] ST Gu and Q-C He. Interfacial discontinuity relations for coupled multifield phenomena and their application to the modeling of thin interphases as imperfect interfaces. *J Mech Phys Solids*, 59(7):1413–1426, 2011.

[29] G Mishuris. Imperfect transmission conditions for a thin weakly compressible interface. 2d problems. *Arch Mech*, 56(2):103–115, 2004.

[30] M Sonato, A Piccolroaz, W Miszuris, and G Mishuris. General transmission conditions for thin elasto-plastic pressure-dependent interphase between dissimilar materials. *Int J Solids Struct*, 64:9–21, 2015.

[31] D Bigoni and AB Movchan. Statics and dynamics of structural interfaces in elasticity. *Int J Solids Struct*, 39(19):4843–4865, 2002.

[32] M Brun, S Guenneau, AB Movchan, and D Bigoni. Dynamics of structural interfaces: filtering and focussing effects for elastic waves. *J Mech Phys Solids*, 58(9):1212–1224, 2010.

[33] M Touboul, B Lombard, and C Bellis. Time-domain simulation of wave propagation across resonant meta-interfaces. *J Comput Phys*, 414:109474, 2020.

[34] M Touboul, K Pham, A Maurel, J-J Marigo, B Lombard, and C Bellis. Effective resonant model and simulations in the time-domain of wave scattering from a periodic row of highly-contrasted inclusions. *J Elast*, 142(1):53–82, 2020.

[35] F dell'Isola, A Madeo, and L Placidi. Linear plane wave propagation and normal transmission and reflection at discontinuity surfaces in second gradient 3D continua. *ZAMM-Journal of Applied Mathematics and Mechanics/Zeitschrift für Angewandte Mathematik und Mechanik*, 92(1):52–71, 2012.

[36] L Placidi, G Rosi, I Giorgio, and A Madeo. Reflection and transmission of plane waves at surfaces carrying material properties and embedded in second-gradient materials. *Math Mech Solids*, 19(5):555–578, 2014.

[37] I Scala, G Rosi, L Placidi, V-H Nguyen, and S Naili. Effects of the microstructure and density profiles on wave propagation across an interface with material properties. *Continuum Mech Therm*, 31(4):1165–1180, 2019.

[38] G Rosi, L Placidi, V-H Nguyen, and S Naili. Wave propagation across a finite heterogeneous interphase modeled as an interface with material properties. *Mech Res Commun*, 84:43–48, 2017.

[39] A Aghaei, N Bochud, G Rosi, and S Naili. Assessing the effective elastic properties of the tendon-to-bone insertion: a multiscale modeling approach. *Biomech Model Mechanobiol*, pages 1–16, 2020.

[40] F dell'Isola and A Romano. On the derivation of thermomechanical balance equations for continuous systems with a nonmaterial interface. *Int J Eng Sci*, 25(11-12):1459–1468, 1987.

[41] F dell'Isola and A Romano. A phenomenological approach to phase transition in classical field theory. *Int J Eng Sci*, 25(11-12):1469–1475, 1987.

[42] F dell'Isola and L Placidi. Variational principles are a powerful tool also for formulating field theories. In *Variational models and methods in solid and fluid mechanics*, pages 1–15. Springer, 2011.

[43] I Wakabayashi, E Itoi, H Sano, Y Shibuya, R Sashi, H Minagawa, and M Kobayashi. Mechanical environment of the supraspinatus tendon: a two-dimensional finite element model analysis. *J Shoulder Elbow Surg*, 12(6):612–617, 2003.

[44] RE Debski, JA Weiss, WJ Newman, SM Moore, and PJ McMahon. Stress and strain in the anterior band of the inferior glenohumeral ligament during a simulated clinical examination. *J Shoulder Elbow Surg*, 14(1):S24–S31, 2005.

[45] E Pena, B Calvo, MA Martinez, and M Doblare. A three-dimensional finite element analysis of the combined behavior of ligaments and menisci in the healthy human knee joint. *J Biomech*, 39(9):1686–1701, 2006.

[46] S Thomopoulos, GR Williams, and LJ Soslowsky. Tendon to bone healing: differences in biomechanical, structural, and compositional properties due to a range of activity levels. *J Biomech Eng*, 125(1):106–113, 2003.

[47] M Benjamin, H Toumi, JR Ralphs, G Bydder, TM Best, and S Milz. Where tendons and ligaments meet bone: attachment sites ('entheses') in relation to exercise and/or mechanical load. *J Anat*, 208(4):471–490, 2006.

[48] AC Deymier, AG Schwartz, Z Cai, TL Daulton, JD Pasteris, GM Genin, and S Thomopoulos. The multiscale structural and mechanical effects of mouse supraspinatus muscle unloading on the mature enthesis. *Acta Biomater*, 83:302–313, 2019.

[49] Y Liu, V Birman, C Chen, S Thomopoulos, and GM Genin. Mechanisms of bimaterial attachment at the interface of tendon to bone. *J Eng Mater Technol*, 133(1):011006, 2011.

[50] AC Abraham and TLH Donahue. From meniscus to bone: a quantitative evaluation of structure and function of the human meniscal attachments. *Acta Biomater*, 9(5):6322–6329, 2013.

[51] VA Eremeyev, G Rosi, and S Naili. Transverse surface waves on a cylindrical surface with coating. *Int J Eng Sci*, 147:103188, 2020.

[52] Y Hériveaux, V-H Nguyen, and G Haïat. Reflection of an ultrasonic wave on the bone-implant interface: A numerical study of the effect of the multiscale roughness. *J Acoust Soc Am*, 144(1):488–499, 2018.

[53] S Le Cann, E Törnquist, I Silva Barreto, M Fraulob, HA Lomami, M Verezhak, M Guizar-Sicairos, H Isaksson, and G Haiat. Spatio-temporal evolution of hydroxyapatite crystal thickness at the bone-implant interface. *Acta Biomater*, 116:391–399, 2020.

[54] F Xu, X Zhang, and H Zhang. A review on functionally graded structures and materials for energy absorption. *Eng Struct*, 171:309–325, 2018.

Chapter 4. Ultrasound characterization of bioinspired functionally graded soft-to-hard composites: Experiment and modeling

The work presented in this chapter is issued from the following publication:
A Aghaei, N Bochud, G Rosi, Q Grossman, D Ruffoni and S Naili, Ultrasound characterization of bioinspired functionally graded soft-to-hard composites: Experiment and modeling, *J Acoust Soc Am*, 151(3): 1490 – 1501, 2022.

Contents

Abstract

Functional grading is a distinctive feature adopted by nature to improve the transition between tissues that present a strong mismatch in mechanical properties, a relevant example being the tendon-to-bone attachment. Recent progress in multi-material additive manufacturing now allows for the design and fabrication of bioinspired functionally graded soft-to-hard composites. Nevertheless, this emerging technology depends on several design variables, including both material and mechanistic ingredients, that are likely to affect the mechanical performance of such composites. In this paper, a model-based approach is developed to describe the interaction of ultrasound waves with homogeneous and heterogeneous additively manufactured samples, which respectively display a variation either of the material ingredients (e.g., ratio of the elementary constituents) or of their spatial arrangement (e.g., functional gradients, damage). Measurements are performed using longitudinal bulk waves, which are launched and detected using a linear transducer array. The model is first calibrated by exploiting the signals measured on the homogeneous samples, which allow identifying relationships between the model parameters and the material composition. Second, the model is validated by comparing the signals measured on the heterogeneous samples with those predicted numerically. Overall, the reported results pave the way for characterizing and optimizing multi-material systems that display complex bioinspired features.

4.1 Introduction

Joining soft-to-hard materials is a frequent requirement in modern engineering applications (e.g., aerospace, tissue engineering) that rises several challenges. Such attachment generally needs to effectively transfer mechanical stresses and sustain large forces for several millions of loading cycles without being damaged. To this end, different strategies can be found in nature to alleviate stress concentrations at the interface between materials with highly dissimilar properties, one of them being the use of functionally graded interphases [1].

In this context, the development of bioinspired composite materials has been limited for many years by the ability of traditional manufacturing methods to synthesize and assemble materials with different properties. However, recent progress in additive manufacturing [also known as three-dimensional (3D) printing] allowed unlocking this technical burden and opened new ways to design and fabricate materials with dissimilar properties [2]. In particular, material jetting is considered as a powerful process for multi-material additive manufacturing. Similar to biological systems engineered by nature through a bottom-up approach, this technique arranges dissimilar building blocks at several length scales to build a final component with enhanced and adaptable mechanical performance [3, 4]. Thanks to its high resolution (i.e., voxels with side lengths around 40 μm) and the possibility to locally tailor the material composition, numerous studies used this strategy to prototype bioinspired heterogeneous structures [5–7], in particular functionally graded soft-to-hard composites [8–10]. The latter are typically designed as multilayers whose material properties smoothly evolve along one or two dimensions, overall resulting in materials with superior behavior and manifold functionalities.

However, to fully exploit the potential of these emerging composites, there is an un-

met need in developing methods for characterizing the quality of the printing process and the mechanics of the manufactured samples. Indeed, multi-material jetting typically depends upon several characteristics, such as the properties of the elementary constituents, their spatial arrangement, as well as the printing orientation and resolution, but their impact on the overall mechanical performance is still elusive. Several characterization techniques have been applied recently, including tensile testing [9, 11], dynamic mechanical analysis [12, 13], and ultrasonic testing [14], altogether providing guidelines for process modifications and subsequent design optimization. Among these, quantitative ultrasound is thought as a particularly relevant nondestructive means to probe the quality of functionally graded soft-to-hard composites, because it relies on the use of mechanical waves and thus possesses intrinsic sensitivity to their mechanical properties. Moreover, ultrasound requires limited sample preparation and offers a very fast inspection capability.

Although several researchers proposed the use of ultrasound-based methods either for the characterization of monolithic and graded materials [16–18] or for the detection of defects such as pores, cracks and microstructural anomalies [19], most attention has been given to metal-based additively manufactured products so far. Notwithstanding, a few studies have explored its use for assessing the acoustic and mechanical properties of multi-material inkjet-based products, which are becoming more widespread for the rapid production of models for preoperative planning (e.g., medical implants, tissue-mimicking phantoms) and of passive components for medical devices [20]. For instance, an ultrasound through-transmission method was proposed to quantify the level of anisotropy induced by the printing process, although the polymeric constituent was initially isotropic [21]. The phase velocity and attenuation characteristics could be determined along different directions, thereby providing a basis for flaw detection. Using a pulse-echo ultrasound technique, Jacquet *et al.* [22] measured the phase velocity and attenuation of two different materials (i.e., a wax-like support material and a rigid glassy polymer), which were subsequently exploited to design, print, and image multi-material phantoms including heterogeneities with arbitrary geometries. In another related study, Fariñas *et al.* [23] printed multi-material samples by varying the ratio between the two deposited constituents (i.e., a rigid glassy polymer and an elastomeric polymer) and subsequently measured their acoustic impedances as a function of the mass density using a non-contact ultrasound technique. These earlier studies provided a valuable insight on the acoustic properties of additively manufactured samples. However, to the authors' best knowledge, these were limited to the study of macroscopically homogeneous samples lacking mechanistic ingredients, such as the spatial arrangement of the elementary constituents.

This study therefore aims at understanding the interactions of ultrasound waves with additively manufactured multi-material samples, featuring functional grading and programmed damage. Towards this goal, two sets of samples are fabricated using a polyjet 3D printing technology. The first set consists of macroscopically homogeneous samples obtained by varying the ratio of the two elementary constituents, whereas the second set consists of functionally graded soft-to-hard samples. The adopted biomimetic strategy to design heterogeneous structures is based on the graded tissue system at the tendon-to-bone interphase, which fulfills the challenging task of integrating soft-to-hard tissues over a submillimeter-wide region [24]. A pulse-echo technique using a multielement probe in the MHz-regime is employed to characterize the samples. From the measurements performed on the homogeneous samples, we first identify relationships between the mechanical properties and the material composition by solving a model-based inverse problem. In a second

part, these relationships are used to feed a wave propagation model that accounts for the structural and material complexity of the functionally graded samples. Overall, our modeling results show an excellent agreement with the measured signals for cases where the transition region is on the order of magnitude of the bulk wavelength, thereby providing a nondestructive means for characterizing and optimizing bioinspired multi-material composites.

The remainder of the paper is organized as follows: Sec. 4.2 presents the methods used to additively manufactured the samples and to perform the ultrasound measurements. Section 4.3 introduces the theoretical fundamentals of our modeling approach, which relies on the Szabo wave equation and the transfer matrix formalism. The model calibration and validation results are then exposed in Secs. 4.4–4.5. Finally, the strengths and limitations of the proposed approach are discussed in Sec. 4.6.

4.2 Samples and ultrasound measurements

Multi-material additive manufacturing of the samples was achieved using a commercial polyjet 3D printer (Objet 260, Stratasys), which applies a layer-by-layer method where multiple streams of UV-curable photopolymers are jetted through printing nozzles onto a building tray [13]. At the microscale (voxel level), custom-made patterns can be obtained by spreading two photopolymers with highly dissimilar properties, i.e., a rigid glassy polymer (commercial name VeroWhitePlus, VW^+) and an elastomeric polymer (commercial name TangoBlackPlus, TB^+), on a chessboard-like volume as depicted in Fig. 4.1. From a macroscopic viewpoint, this process allows printing both homogeneous samples with any intermediate volume fraction [see Fig. 4.1(a)] and heterogeneous samples with a functional grading between the soft and hard photopolymers [see Fig. 4.1(b)].

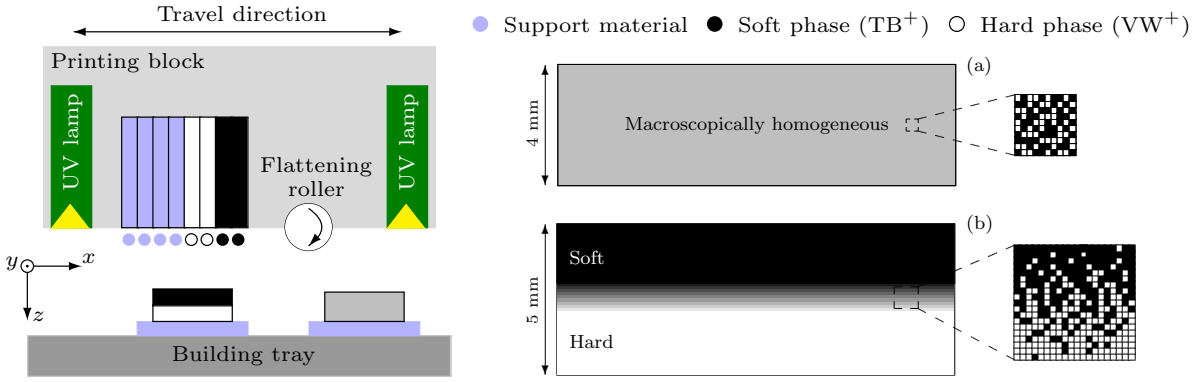

Figure 4.1 – Schematic representation of the polyjet 3D printing process, which allows for the additive manufacturing of both (a) homogeneous samples (e.g., $V_f = 50\%$) and (b) heterogeneous samples with functional grading, obtained by locally spreading two photopolymers with highly dissimilar properties.

Two sets of 3D-printed samples were investigated here. The first set consisted of 11 homogeneous plate-like samples displaying different volume fractions of the compliant photopolymer (TB^+), denoted by V_f of TB^+, which ranged from 0 to 100% with a step of 10%. Their overall dimensions were $20 \times 16 \times 4$ mm^3, printed using random dithering

patterns along the x, y, and z directions, respectively. The second set consisted of six heterogeneous samples, which were all compound of a soft layer (i.e., TB^+), a hard layer (i.e., VW^+), and an interphase in-between, which was inspired by the tendon-to-bone attachment. For the latter, different profiles have been selected for the interphase layer by adjusting the relative proportions of the two photopolymers along the z-direction [see Fig. 4.2]. This printing direction was chosen to minimize photopolymer diffusion and mixing between different layers [13]. The first sample was a bilayer that displays a sharp transition between the soft and hard layers, whose thickness amounts to 2.2 mm and 2.8 mm, respectively [Fig. 4.2(a)]. Likewise, the second sample was a trilayer with a 2 mm-thick soft layer, a 2.232 mm-thick hard layer, and a 768 μm-thick homogeneous interphase in-between [Fig. 4.2(b)]. Apart from these two profiles that served us as a reference, two further profiles highlighting functional grading have been printed, one with a linearly varying interphase layer [see Fig. 4.2(c)], the other with a smoothly varying interphase layer [see Fig. 4.2(d)]. It should be noted that these bioinspired profiles were designed based on recent multiscale modeling results [25, 26], which showed that the native tendon-to-bone attachment can be seen as a continuous functionally graded material. Moreover, to mimic local damage characteristics such as tears and fissures, which are acknowledged to be footprint of clinical burden related to physical overloading or pathology [27, 28], slightly modified versions of these two functionally graded profiles were designed too [see Fig. 4.2(e)–(f)]. Programmed damage was achieved by assigning a sudden and local variation of the volume fraction to a finite-width layer, i.e., 64 μm wide, across the interphase. The overall dimensions of the six heterogeneous samples were $20 \times 16 \times 5$ mm^3, printed with a voxel size of $120 \times 120 \times 32$ μm^3 along the x, y, and z directions, respectively. The thickness of the interphase (i.e., 768 μm) was chosen according to physiological observations found in the literature [29], which showed that the size of the tendon-to-bone attachment typically ranges from a few hundred micrometers to some millimeters depending on the insertion site. Besides, the dimensions of the two surrounding layers were chosen based on a trade-off between temporal resolution and attenuation of the recorded signals, according to the ultrasound characteristics of the probe. Tables summarizing the dimensions and specificities of the two sets of 3D-printed samples are included as supplementary material.[1]

A pulse-echo configuration was considered in this work, where longitudinal bulk waves were launched normally through the samples along the z-direction (see Fig. 4.3). The employed device consisted of a multielement probe (Imasonic, SAS, France), which was driven by a programmable multi-channel electronics (Advanced OEM Solutions, West Chester, USA). This type of device, initially dedicated to medical imaging, has recently also been used for the mechanical characterization of materials, particularly for monitoring the health status of aeronautical structures [30] or for reconstructing the anisotropic elastic tensor of plate-like samples [31].

The measurements were carried out in a water tank by using a linear transducer array that consisted of 32 elements. Each element had a width of 0.5 mm and a height of 12 mm, resulting in a total emission surface of 16×12 mm^2. The transducer array operated at a central frequency $f_c = 2.25$ MHz (-6 dB power spectrum spanning a frequency range from 1.5 to 3 MHz) and the array pitch was 0.5 mm. This probe was used to transmit a

[1] See supplementary material for tables summarizing the dimensions and specificities of the two sets of 3D-printed samples.

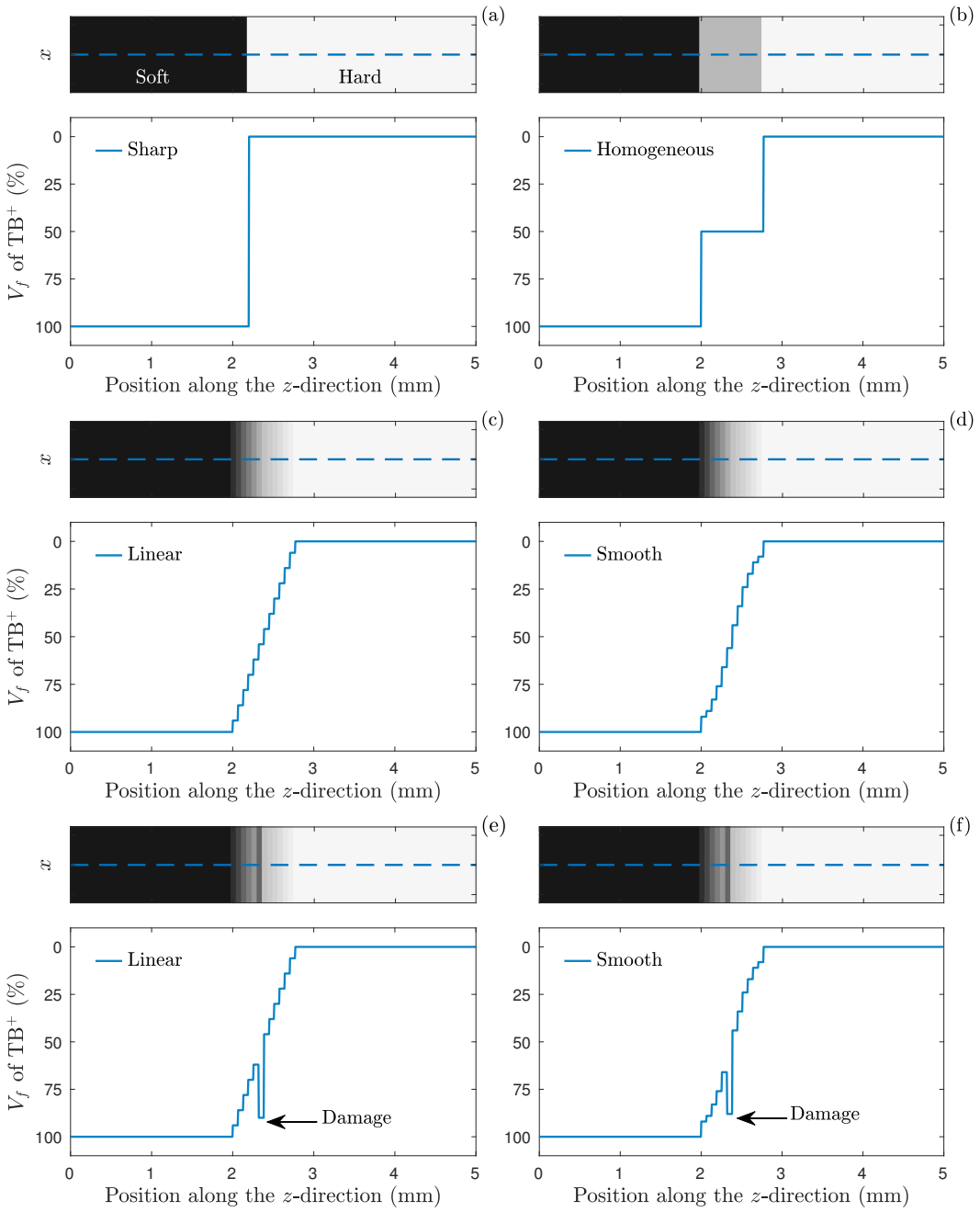

Figure 4.2 – Overview of the spatial arrangement of the volume fractions for the six heterogeneous samples: (a) Bilayer sample with a sharp transition, (b) Trilayer sample with a homogeneous interphase, (c) Sample with a linearly varying interphase, (d) Sample with a smoothly varying interphase, (e) Sample with a localized damage across the linearly varying interphase, and (f) Sample with a localized damage across the smoothly varying interphase. For each subplot, the upper panel represents a view of the sample in the $x-z$ plane, where the dashed blue line makes reference to the spatial arrangement of the volume fraction V_f of TB$^+$ along the z-direction depicted in the lower panel (continuous blue line).

wideband plane wave by concurrently firing a pulse on all emitters. The received signals, which were digitized at a sampling rate of 100 MHz and quantized with a 12-bit resolution, were recorded during 20 μs. The advantage of using a linear transducer array in plane wave mode was twofold. First, because the bulk wavelength was small compared to the total width of the transducer array, beam diffraction effects were negligible and could be neglected in the subsequent processing and modeling of the received signals. Second, it allowed averaging the received signals across all the elements of the probe to enhance the signal-to-noise ratio of the measurement. All measurements were performed under controlled water temperature (20 °C). For the measurement of the heterogeneous samples, it should be noted that the soft layer was always directed towards the transducer array (as in Fig. 4.3).

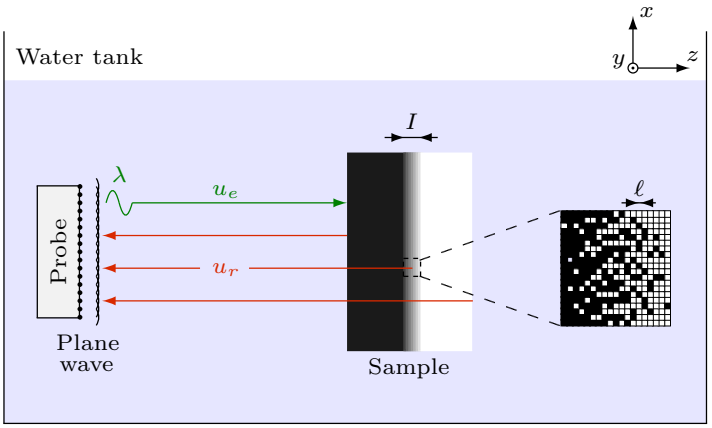

Figure 4.3 – Schematic representation of the pulse-echo configuration used to record the ultrasound measurements. The emitted signal, u_e (in green), is a plane longitudinal wave, whereas the recorded signal, u_r (in red), is compound of the reflections from the front and back faces of the sample, plus that interacting with the interphase. The bulk wavelength λ is of the order of magnitude of the interphase thickness I and much larger than the typical size ℓ of the heterogeneities, i.e., $\lambda \sim I \gg \ell$.

4.3 Mechanical modeling

The wave interactions with the functionally graded samples (recall Fig. 4.2) can be approximated by a model based on the transfer matrix formalism [32]. This formalism was here adapted to describe the wave propagation in a finite multilayered viscoelastic medium exhibiting a power-law attenuation. Several observations guided the choice of this model. First, in the frequency bandwidth of interest, the wavelengths of the longitudinal bulk wave, ranging from around 500 μm to 2.5 mm, were much larger than the typical size of the heterogeneities (i.e., voxel size of 32 μm along the z-direction). The functionally graded samples can thus be considered as successive piecewise homogeneous media. Second, since the viscous behavior of the photopolymers exhibited dispersive losses that cannot be accurately described by a rheological Voigt model (whose attenuation is proportional to the square of the angular frequency ω^2), we sought for a model that allowed describing more complex attenuation mechanisms (e.g., relaxation phenomena). This can be achieved

by means of the Szabo wave equation [35], which approximates power-law media with an attenuation in the form:

$$\alpha(\omega) = \alpha_0 \omega^r \ , \tag{4.1}$$

where α_0 is a constant and the dimensionless exponent r typically ranges between 1 and 2 for materials belonging to the class of polymers and to some biomaterials [33, 34].

4.3.1 Szabo wave equation

Formally, the model introduced by Szabo and Wu [35] allowed such modeling approach to be generalized to cases for which $r \neq 2$, by introducing a fractional derivative in the wave equation as

$$\frac{\partial^2 u(z,t)}{\partial z^2} - \frac{1}{v_0^2}\frac{\partial^2 u(z,t)}{\partial t^2} - \frac{2\alpha_0}{v_0 \cos\left(\frac{\pi}{2}r\right)}\frac{\partial^{r+1} u(z,t)}{\partial t^{r+1}} = 0 \ , \tag{4.2}$$

where t is the time, v_0 is a constant, and the third term accounts for dispersive losses. By assuming a general harmonic solution for the displacement in the z-direction, $u(z,t) = \exp\left(j(\omega t - kz)\right)$, which satisfies the power-law Eq. (4.2), it can be shown that the dispersion relation between the complex wavenumber $k(\omega)$ and the angular frequency ω can be written as

$$k(\omega) = \sqrt{\frac{\omega^2}{v_0^2} - (j\omega)^{r+1}\frac{2\alpha_0}{v_0 \cos\left(\frac{\pi}{2}r\right)}} \ , \tag{4.3}$$

where j is the unit imaginary number. Note that Eq. (4.3) is valid for all $r \neq 1$. Under the hypothesis of small wavelength $\lambda = 2\pi/k(\omega)$ and low attenuation α_0, i.e., $\lambda\alpha_0 \ll 1$, the dispersion relation [Eq. (4.3)] can be simplified according to Kelly *et al.* [36]:

$$k(\omega) = \frac{\omega}{v_0} - j\frac{\alpha_0 (j\omega)^r}{\cos\left(\frac{\pi}{2}r\right)} \ . \tag{4.4}$$

By invoking the de Moivre's identity for $\pi/2$, i.e., $j^r = \cos(\pi r/2) + j\sin(\pi r/2)$, the imaginary part of Eq. (4.4) leads to the power-law attenuation given by Eq. (4.1), whereas the real part allows expressing the phase velocity as

$$v(\omega) = \frac{\omega}{\Re(k(\omega))} = \left(\frac{1}{v_0} + \alpha_0 \tan\left(\frac{\pi}{2}r\right)\omega^{r-1}\right)^{-1} \ , \tag{4.5}$$

where $\Re(\cdot)$ designates the real part of the quantity. Alternatively, Eq. (4.5) can be written as

$$v(\omega) = \left(\frac{1}{v_1} + \alpha_0 \tan\left(\frac{\pi}{2}r\right)\left(\omega^{r-1} - 1\right)\right)^{-1} \ , \tag{4.6}$$

where v_1 is the phase velocity at a reference frequency $\omega_0 = 1$ Hz. Since Eq. (4.6) presents a singularity when r is an odd integer number (e.g., $r = 1$), another expression for the phase velocity can be derived in this particular case [35, 36],

$$v(\omega) = \left(\frac{1}{v_1} - \frac{2\alpha_0}{\pi}\omega^{r-1}\ln(\omega)\right)^{-1} \ , \tag{4.7}$$

where $\ln(\cdot)$ designates the natural logarithm of the quantity. Combining Eqs. (4.1) and (4.7) yields a dispersion relationship for $r = 1$ as

$$k(\omega) = -j\alpha_0\omega + \frac{\omega}{v_1} - \frac{2\alpha_0}{\pi}\omega\ln(\omega) \ . \tag{4.8}$$

4.3.2 Transfer matrix formalism for a power-law medium

Let us consider a finite multilayered system consisting of $M+1$ homogeneous layers with the same cross-sections, as shown in Fig. 4.4.

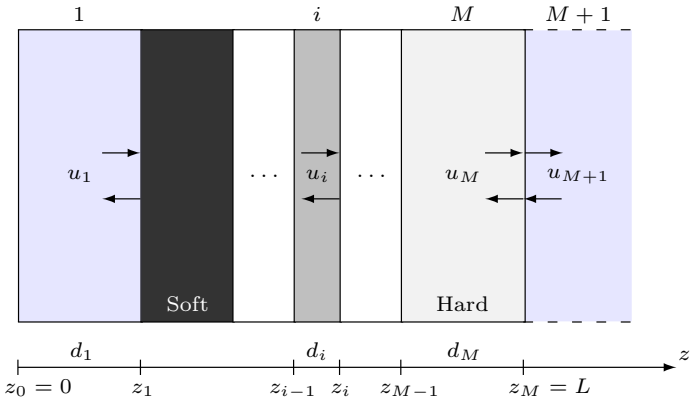

Figure 4.4 – Schematic of the finite multilayered system used to model the wave interactions with the functionally graded soft-to-hard samples immersed in a water tank (in blue).

Note that in this system, layer 1 represents the water path between the probe and the investigated sample, whereas layer $M+1$ is considered as a semi-infinite water layer. A general harmonic solution to the Szabo wave Eq. (4.2) can be stated in the frequency-domain for each layer i, with $i = 1, \ldots, M$, as

$$\begin{aligned} u_i(z,\omega) &= u_i^f(z,\omega) + u_i^b(z,\omega) \\ &= A_i \exp\left(-jk_i(\omega)z\right) + B_i \exp\left(jk_i(\omega)z\right) \ , \end{aligned} \tag{4.9}$$

where $u_i^f(z,\omega)$ and $u_i^b(z,\omega)$ stand for the forward- and backward-propagating components of the displacement in each layer i, respectively. The complex wavenumber $k_i(\omega)$ of layer i is defined according to Eq. (4.4) for $r \neq 1$ and Eq. (4.8) for $r = 1$. In the case of a perfectly bonded interface between two layers, the transmission conditions imply the continuity of displacement and stress across this interface. Expressing these conditions at an arbitrary interface position $z = z_i$ allows characterizing the transition from layer i to layer $i+1$ as in Cretu and Nita [37],

$$\boldsymbol{u}_{i+1}(z_i,\omega) = \boldsymbol{D}_i(\omega)\boldsymbol{u}_i(z_i,\omega) \qquad (i = 1, \ldots, M) \ , \tag{4.10}$$

where $\boldsymbol{u}_i(z,\omega) = \left[u_i^f(z,\omega)\ u_i^b(z,\omega)\right]^T$ is the state vector of layer i, with T being the transpose operator, and $\boldsymbol{D}_i(\omega)$ is the discontinuity matrix, which is defined as

$$\boldsymbol{D}_i(\omega) = \frac{1}{2}\begin{pmatrix} 1 + \dfrac{Z_i(\omega)}{Z_{i+1}(\omega)} & 1 - \dfrac{Z_i(\omega)}{Z_{i+1}(\omega)} \\ 1 - \dfrac{Z_i(\omega)}{Z_{i+1}(\omega)} & 1 + \dfrac{Z_i(\omega)}{Z_{i+1}(\omega)} \end{pmatrix} \ . \tag{4.11}$$

It should be noted that this matrix only depends on the complex acoustic impedance of the two layers being in contact, which is defined by $Z_i(\omega) = \rho_i \omega / k_i(\omega)$, where ρ_i is the mass density of layer i. In the same way, by considering a harmonic wave propagating in the same homogeneous layer i from position $z = z_{i-1}$ to position $z = z_i$, its transformed displacement can be expressed by means of the propagation matrix $\boldsymbol{P}_i(\omega)$ as

$$\boldsymbol{u}_i(z_i, \omega) = \boldsymbol{P}_i(\omega)\boldsymbol{u}_i(z_{i-1}, \omega) \qquad (i = 1, \ldots, M) \ , \tag{4.12}$$

with

$$\boldsymbol{P}_i(\omega) = \begin{pmatrix} \exp\left(-jk_i(\omega)d_i\right) & 0 \\ 0 & \exp\left(jk_i(\omega)d_i\right) \end{pmatrix} \ , \tag{4.13}$$

where $d_i = z_i - z_{i-1}$ is the thickness of layer i. The relation between the input and output state vectors for layer i can therefore be expressed as

$$\boldsymbol{u}_{i+1}(z_i, \omega) = \boldsymbol{T}_i(\omega)\boldsymbol{u}_i(z_{i-1}, \omega) \qquad (i = 1, \ldots, M) \ , \tag{4.14}$$

where $\boldsymbol{T}_i(\omega) = \boldsymbol{D}_i(\omega)\boldsymbol{P}_i(\omega)$ is the transfer matrix of layer i. The total transfer matrix $\boldsymbol{T}(\omega)$, which describes the overall reflections, transmissions, and losses of the wave propagating across the graded structure from Fig. 4.4, can then be obtained as the product of transfer matrices from successive layers,

$$\boldsymbol{T}(\omega) = \prod_{i=0}^{M-1} \boldsymbol{T}_{M-i}(\omega) \ , \tag{4.15}$$

which leads to a relation between the input and output state vectors as,

$$\boldsymbol{u}_{M+1}(L, \omega) = \boldsymbol{T}(\omega)\boldsymbol{u}_1(0, \omega) \ . \tag{4.16}$$

Applying the radiation energy condition at position $z = L$, i.e., $u^b_{M+1}(L, \omega) = 0$, allows solving Eq. (4.16) for a pulse-echo configuration and thus determining the backward propagating displacement as a function of the imposed displacement at the transmitter location as

$$u^b_1(0, \omega) = -\frac{T_{21}(\omega)}{T_{22}(\omega)} u^f_1(0, \omega) \ , \tag{4.17}$$

where $T_{2m}(\omega)$, with $m = 1, 2$, denotes the components of the second row of the total transfer matrix $\boldsymbol{T}(\omega)$. It should be noted that $u^f_1(0, \omega)$ is the Fourier transform of the emitted signal $u_e(t)$, which can in practice be measured by taking a delayed version of the signal reflected by a perfect reflector. In the same way, the reflected signal $u_r(t)$ can be retrieved in the time-domain by calculating the inverse Fourier transform of $u^b_1(0, \omega)$. To solve Eq. (4.17) for the functionally graded samples (recall Fig. 4.2), it is therefore necessary to have a precise knowledge of the mechanical properties associated with each layer i, namely, ρ, v_1, α_0, and r (if $r \neq 1$). Towards this goal, a model calibration strategy is proposed in Sec. 4.4.

4.4 Model calibration

The set of homogeneous samples was first characterized to derive volume fraction-dependent mechanical properties, which will in turn be used to feed the mechanical model developed to predict the measurements obtained on the heterogeneous samples.

4.4.1 Ultrasound characterization of homogeneous samples

To extract ultrasound characteristics, e.g., the phase velocity $v(\omega)$ and attenuation $\alpha(\omega)$, from the measurements performed on the homogeneous samples, a dedicated signal processing approach has been developed. To serve as an example, Figure 4.5(a) depicts the raw spatiotemporal signals measured on the stiffest homogeneous sample (i.e., volume fraction V_f of TB^+ equal to 0%), which contain plane wavefronts along with spurious signals due to edge effects. A first step therefore consisted in filtering these edge effects

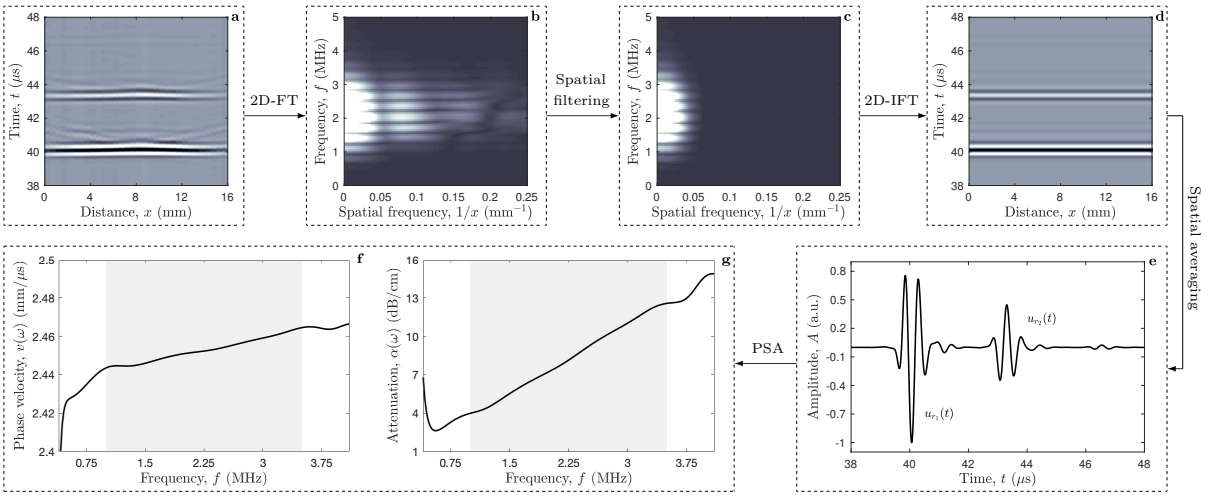

Figure 4.5 – Flowchart of the dedicated signal processing steps, which are illustrated on the measurement performed on the stiffest homogeneous sample (i.e., $V_f = 0\%$): (a) Raw spatiotemporal signals; (b) 2D Fourier transform (2D-FT) of the recorded signals; (c) Resulting spectrum in the Fourier plane after applying a spatial low-pass filtering; (d) Retrieved spatiotemporal signals after applying a 2D inverse Fourier transform (2D-IFT); (e) Processed measurement after spatial averaging; and (f)–(g) Frequency-dependent phase velocity and attenuation obtained after applying a phase spectrum approach (PSA).

that could cause aliasing, in order to retain only the plane wavefronts for the posterior determination of the amplitude and phase spectra. This was achieved by applying a two-dimensional Fourier transform (2D-FT) to the recorded spatiotemporal signals [see Fig. 4.5(b)]. Then, at each frequency f, a low-pass finite impulse response filter was applied to the resulting signals in the Fourier plane [see Fig. 4.5(c)]. Finally, the plane wavefronts were recovered in the time-domain by applying a 2D inverse Fourier transform (IFT) to the filtered spectra [see Fig. 4.5(d)]. The signals obtained on each element were then averaged [see Fig. 4.5(e)]. As can be observed, the resulting reflected signal $u_r(t)$ is generally compound of at least two echoes corresponding to reflections from the front and back faces of the sample, denoted by $u_{r_1}(t)$ and $u_{r_2}(t)$. A second step consisted in applying a phase spectrum approach (PSA) to these two reflected echoes, in order to retrieve the frequency-dependent phase velocity and attenuation of the sample. The frequency-dependent phase velocity $v(\omega)$ was derived as in He and Zheng [38] and Raišutis *et al.* [33],

$$v(\omega) = \frac{2D}{\Delta t + \Delta\phi/\omega} \,, \tag{4.18}$$

where D is the sample thickness, $\Delta\phi$ is the phase spectra difference between the two reflected echoes, and $\Delta t = t_2 - t_1$ is the time delay between the two reflected echoes, which was determined using the cross-correlation of $u_{r_1}(t)$ and $-u_{r_2}(t)$ [recall Fig. 4.5(e)].

In the same way, the frequency-dependent attenuation $\alpha(\omega)$ was calculated as

$$\alpha(\omega) = \frac{1}{2D} \ln\left(\left|\frac{A_1(\omega)T(\omega)}{A_2(\omega)}\right|\right) , \tag{4.19}$$

where $A_1(\omega)$ and $A_2(\omega)$ are the amplitude spectra of the two reflected echoes, and $T(\omega)$ is the power transmission coefficient, which is defined as

$$T(\omega) = \frac{4Z_w Z_s(\omega)}{(Z_w + Z_s(\omega))^2} , \tag{4.20}$$

where $Z_w = \rho_w c_w$ and $Z_s(\omega) = \rho_s v(\omega)$ are the acoustic impedances of water and of the sample, respectively, with ρ_w and ρ_s being their respective mass densities. The latter was determined based on a simple mixing rule,

$$\rho_s(V_f) = \rho_{\mathrm{TB}^+} \cdot V_f + \rho_{\mathrm{VW}^+} \cdot (1 - V_f) , \tag{4.21}$$

where $\rho_{\mathrm{TB}^+} = 1.143$ g.cm^{-3} and $\rho_{\mathrm{VW}^+} = 1.177$ g.cm^{-3} were measured using a micrometer for the volume and a high accuracy balance for the mass. The sound speed in water, c_w, was set according to the water tank temperature [39].

Figures 4.5(f)–(g) depict the retrieved phase velocity $v(\omega)$ and attenuation $\alpha(\omega)$ for this sample. As can be observed, within the useful bandwidth (indicated as a gray area), the phase velocity $v(\omega)$ increases with frequency, thus indicating that the sample is slightly dispersive, whereas the attenuation $\alpha(\omega)$ increases nearly linearly as a function of the frequency.

These signal processing steps were applied to all homogeneous samples and the resulting evolution of the ultrasound characteristics as a function of the volume fraction V_f of TB^+ is depicted in Fig. 4.6 for three different frequencies. As expected, the phase velocity

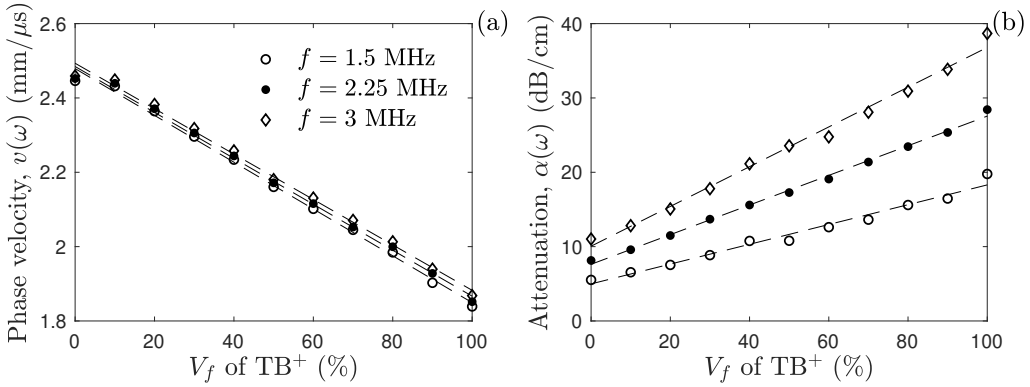

Figure 4.6 – Evolution of the (a) phase velocity $v(\omega)$ and (b) attenuation $\alpha(\omega)$ as a function of the volume fraction V_f of TB^+ for three different frequencies f. Linear fits are plotted in dashed lines for comparison.

decreases with increasing V_f of TB^+, whereas the attenuation increases with increasing V_f of TB^+. It should be noted that both ultrasound characteristics can be remarkably explained by a linear approximation. These trends remain valid within the considered useful frequency bandwidth (data not shown).

4.4.2 Inverse problem

Altogether, our observations suggested that the experimental dispersion relation should yield a frequency-dependent phase velocity and a power-law attenuation, which *a posteriori* justified the model approximation presented in Sec. 4.3.1. To further investigate the ability of this model to predict experimentally observed data, we proposed an optimization procedure to identify the model parameters $\boldsymbol{\theta} = [v_1 \ \alpha_0 \ r]$ that minimize the following objective function $F(\boldsymbol{\theta})$ in a least squares sense as

$$F(\boldsymbol{\theta}) = \sqrt{\frac{1}{N}\sum_{n=1}^{N}\left|\frac{k(\omega_n) - k(\omega_n;\boldsymbol{\theta})}{k(\omega_n)}\right|^2} \ , \tag{4.22}$$

where $k(\omega_n)$ and $k(\omega_n;\boldsymbol{\theta})$ denote the measured and modeled complex wavenumbers at the n-th frequency, respectively, while N is the length of the useful frequency bandwidth on which the optimization is performed [recall the gray area in Fig. 4.5(f)–(g)]. As the measurement of the attenuation $\alpha(\omega)$ evidenced that most samples follow a power-law with an exponent r close to 1, we hypothesized that its value was constant for all homogeneous samples. Therefore, the minimization was performed by sweeping r from 1 to 1.5 with a step of 0.01. For each r, the minimization of $[v_1 \ \alpha_0]$ was achieved with a gradient-based method using the built-in sequential quadratic programming algorithm for constrained nonlinear optimization from Matlab (The MathWorks Inc., Natick, MA). Formally, the optimal model parameters result from

$$\hat{\boldsymbol{\theta}} = \arg\min_{r}\left(\frac{1}{N_r}\sum_{i=1}^{N_r}\left(\arg\min_{v_1,\alpha_0,r_i} F_i(\boldsymbol{\theta})\right)\right) \ , \tag{4.23}$$

where N_r is the number of tested values for the power-law exponent r.

To serve as an example, Figure 4.7 depicts the optimal matching between the measured and modeled phase velocity and attenuation for the homogeneous samples with a volume fraction V_f of TB^+ equal to 30%, 50%, and 70%, which shows an excellent agreement on the useful frequency bandwidth. For these cases, the identified model parameters were $v_1 = [2.13 \ 1.97 \ 1.84]$ mm/μs, $\alpha_0 = [0.59 \ 0.76 \ 0.94]$ dB/cm/(rad.MHz)^r, and $r = 1.17$.

This minimization procedure was then applied to all homogeneous samples, in order to assess the relationship between the volume fraction and the optimal model parameters. Figure 4.8 depicts the evolution of the optimal mechanical characteristics v_1 and α_0 as a function of the volume fraction V_f of TB^+.

As can be observed, both mechanical characteristics are remarkably approximated by a linear regression analysis ($R^2 = 0.99$, $p < 0.05$), with root mean square errors for v_1 and α_0 that are equal to 0.01 mm/μs and 0.02 dB/cm/(rad.MHz)^r, respectively. The resulting linear relationships are

$$\begin{array}{rcl} v_1(V_f) & = & -0.725 \cdot V_f + 2.343 \\ \alpha_0(V_f) & = & \ \ 0.899 \cdot V_f + 0.333 \end{array} \ , \tag{4.24}$$

for a constant exponent $r = 1.17$.

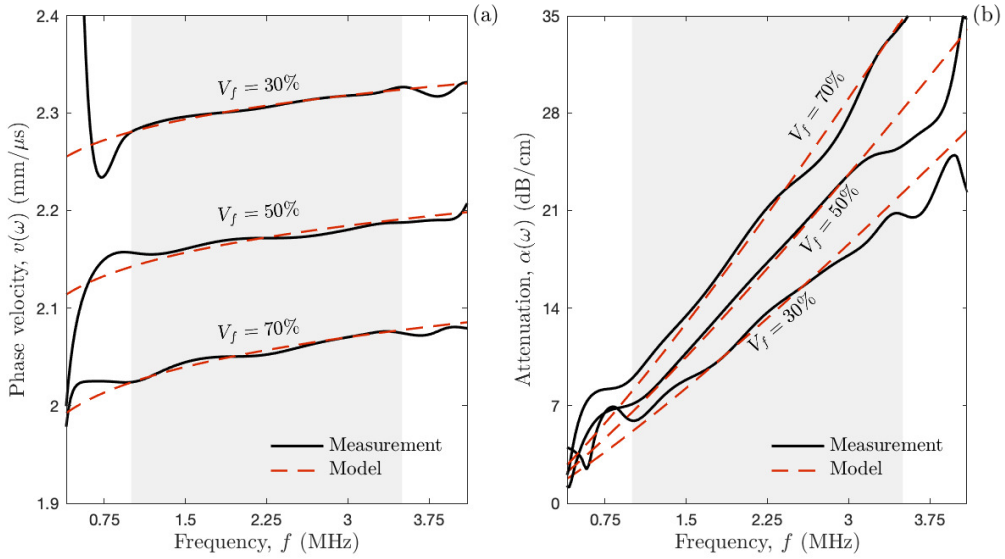

Figure 4.7 – Optimal matching between the measured and modeled (a) phase velocity and (b) attenuation, for the homogeneous samples with a volume fraction V_f of TB$^+$ equal to 30%, 50%, and 70%. The gray area shows the useful frequency bandwidth on which the inversion process was performed.

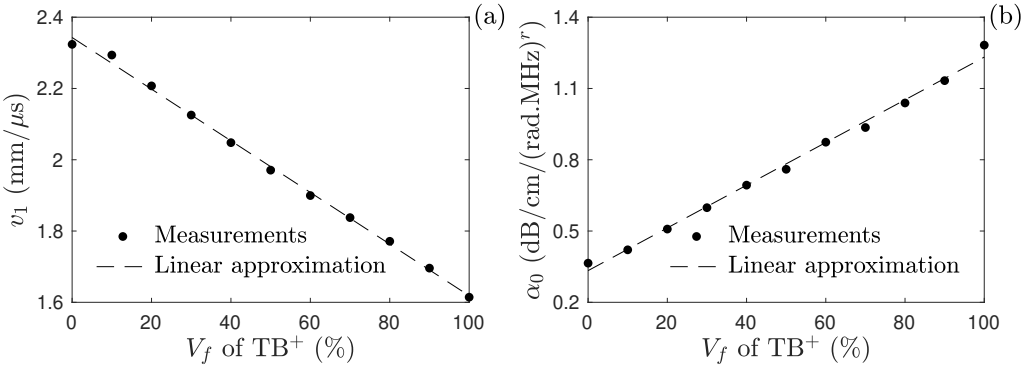

Figure 4.8 – Evolution of the optimal model parameters $\boldsymbol{\theta}$, i.e., (a) v_1 and (b) α_0 ($r = 1.17$), as a function of the volume fraction V_f of TB$^+$.

4.5 Model validation

The goal of this section was to compare the measurements performed on the heterogeneous samples with those predicted by the mechanical model presented in Sec. 4.3.2. Towards this goal, the signals were directly compared in the time-domain. Therefore, the signal processing steps (a)–(e) were applied to the measured signals (recall Fig. 4.5). On the other hand, for each configuration depicted in Fig. 4.2, the relationships [Eqs. (4.21) and (4.24)] were used to feed the model and subsequently solve Eq. (4.17).

Figure 4.9 depicts the measured (continuous black line) and modeled (dashed red line) signals for the six heterogeneous samples with different graded profiles. As can be observed, these signals consist of two main invariant echoes, which correspond to reflections from the front and back faces of the samples (depicted by green arrows), respectively. The

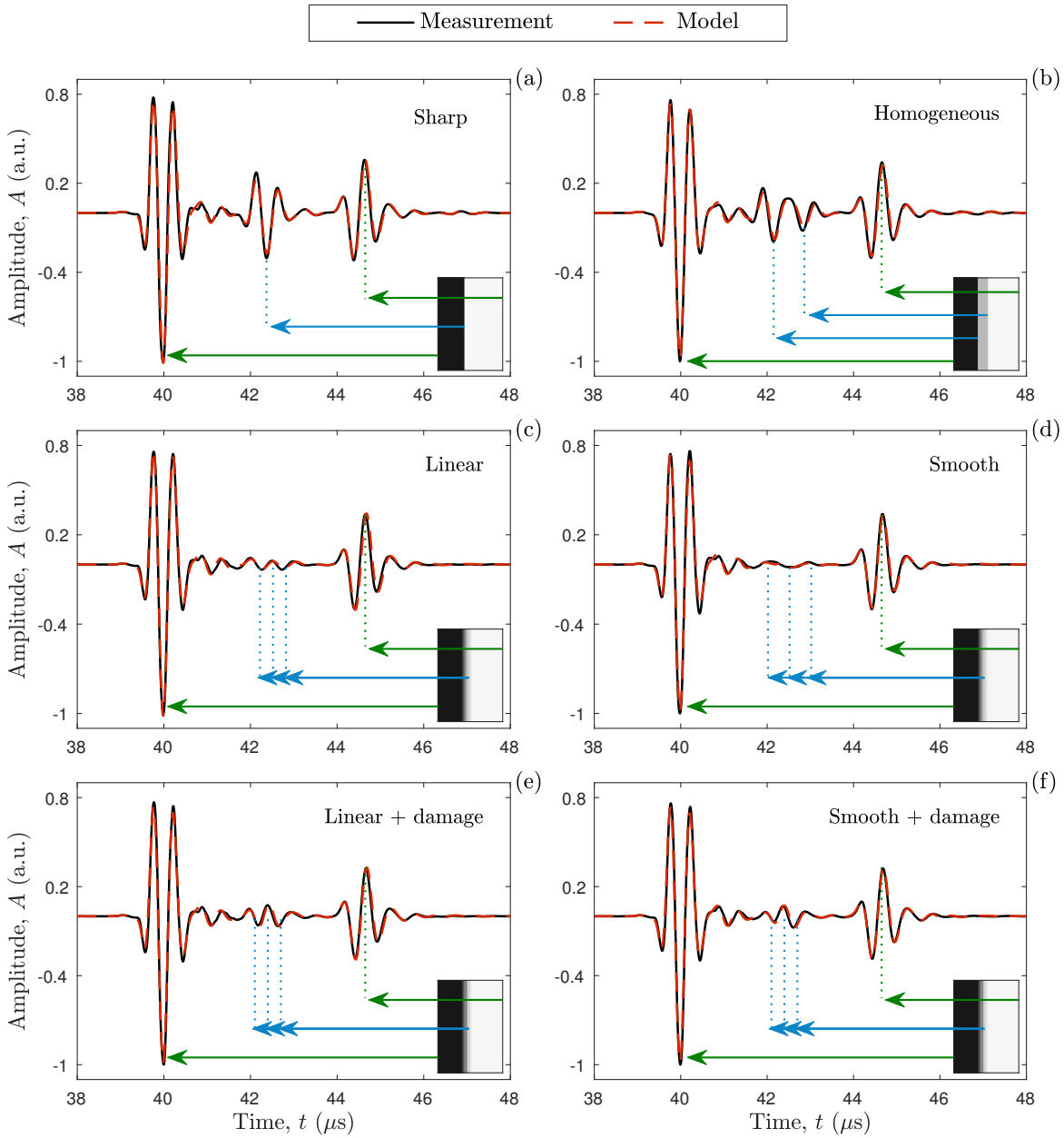

Figure 4.9 – Comparison between the measurement and the model for the six heterogeneous samples (recall Fig. 4.2): (a) Bilayer sample with a sharp transition, (b) Trilayer sample with a homogeneous interphase, (c) Sample with a linearly varying interphase, (d) Sample with a smoothly varying interphase, (e) Sample with a localized damage across the linearly varying interphase, and (f) Sample with a localized damage across the smoothly varying interphase. The inserts schematize the different arrivals of the signal components reflected from the front and back faces of the immersed sample, as well as from the interphase.

signal fluctuations in-between represent a signature of the reflections from the interphase (depicted by blue arrows), which differ in time of arrival and amplitude across the different samples, thus indicating that the proposed measurement technique is sensitive to different functionally graded profiles. As expected, the two reference profiles highlighting

a discontinuous transition [see Fig. 4.9(a)–(b)] present stronger reflections in the form of a single echo and two superimposed echoes, which are due to the presence of a sharp interface and a homogeneous interphase, respectively. In contrast, for the two profiles displaying a continuous transition [see Fig. 4.9(c)–(d)], the reflections are nearly completely filtered out. It can be noted that for the smoothly varying profile, the remaining signal consists of lower frequency components than for the linearly varying one (evidenced by the space between the multiple headed arrow). Interestingly, for the two damaged profiles [see Fig. 4.9(e)–(f)], the local and sudden drop in volume fraction induces a local decrease in the mechanical characteristics as well, which lead to the presence of higher amplitude fluctuations than for their undamaged counterparts.

Overall, there is an excellent agreement between the model and the measurements, thus confirming the choice of a modeling approach that incorporates a frequency-dependent phase velocity and a power-law attenuation. Although the measurements alone could allow discriminating different graded profiles to some extent [e.g., Fig. 4.9(a)–(d)], our model-based approach allows quantifying finely-tuned differences in the manufacturing process [e.g., Fig. 4.9(e)–(f)]. Therefore, such a model could be further used as a guide towards the design of specific configurations.

4.6 Discussion

In this study, we proposed a nondestructive method for the characterization of bioinspired functionally graded soft-to-hard composites by ultrasound. These were designed and additively manufactured using a voxel-by-voxel multi-material 3D printing technique, which allowed for a local and accurate control of the spatial arrangement of two phases with highly dissimilar properties (i.e., a rigid glassy polymer and an elastomeric polymer). Both homogeneous and heterogeneous samples with functional grading were obtained by adjusting the relative proportions of these two photopolymers. All samples were then measured in the MHz-regime using a multielement probe driven by a multichannel electronics. In a first part, the signals retrieved from the homogeneous samples were processed using a spectral method to extract information about the phase velocity and attenuation dispersion. From these acoustic characteristics, relationships between the model parameters and the material composition were identified by solving a model-based inverse problem. In a second part, these relationships were used to feed a multilayered model based on the transfer matrix formalism, which could be validated by systematically comparing the predicted signals to those measured on the heterogeneous samples with functional grading.

The main findings were as follows: First, for the considered photopolymers, the measurements performed on the macroscopically homogeneous samples evidenced that the dispersion relation exhibited a frequency-dependent phase velocity and a power-law attenuation. Such behavior could be adequately modeled using the Szabo wave equation. Second, the derived relationships between the mechanical characteristics (i.e., v_1 and α_0) and the composition (i.e, volume fraction of the compliant polymer) were shown to be linear. It should be noted that this is not necessarily the case for the elastic modulus and strength, which were shown to follow a nonlinear trend with the volume fraction [11, 13]. Third, although the 3D printing process, which delivers complex patterns at the microscale, yields a rather continuous functional grading at the macroscale, the heterogeneous samples could be satisfactorily modeled as successive piecewise homogeneous

layers. Fourth, the proposed model allowed discriminating different profiles displaying slight variations of the material and mechanistic ingredients.

For the homogeneous samples, a direct quantitative comparison with earlier reported acoustic characteristics is difficult. Indeed, the applied ultrasonic measurement technique, in particular the explored frequency regime, along with the investigated samples generally differ from one study to another. For instance, by performing through-transmission measurements on a 3 mm-thick sample using contact longitudinal transducers at 1 MHz, Livings *et al.* [21] reported a value of 2.46 mm/μs for the phase velocity of VW^+. By carrying out pulse-echo measurements on a water-immersed 0.5 mm-thick sample using a focused single-element transducer in the frequency range of 15–30 MHz, Jacquet *et al.* [22] reported values of 2.63 mm/μs and 110 dB/cm for the frequency-dependent phase velocity and attenuation of VW^+ evaluated at 20 MHz, respectively. In another related study, by performing through-transmission measurements on 16 μm-thick samples using air-coupled transducers in the frequency range of 0.15–0.35 MHz, Fariñas *et al.* [23] reported values of 1.9 and 2.8 MRayl for the acoustic impedances of TB^+ and VW^+, respectively. In a recent study closely related to ours, by carrying out transmission measurements on a water-immersed 4 mm-thick sample using a focused single-element transducer in the frequency range of 1–3.5 MHz, Bakaric *et al.* [15] reported values of around 2.50 mm/μs and 9 dB/cm for the frequency-dependent phase velocity and attenuation of VW+, respectively. Extrapolating our modeling results to these frequencies yield (1) values of 2.43, 2.45 and 2.52 mm/μs for the phase velocity of VW^+ at 1, 2.25, and 20 MHz, respectively; (2) values of 8.1 and 104 dB/cm for the attenuation of VW^+ at 2.25 and 20 MHz, respectively; and (3) values of 2.02 and 2.84 MRayl for the acoustic impedances of TB^+ and VW^+ at 0.25 MHz, respectively. These are all in excellent agreement with the reported literature values, thus indicating that our modeling assumptions are reasonable for a wide frequency band. No comparison could be performed for the heterogeneous samples with functional grading and programmed damage as, to the authors' best knowledge, there are no studies in the open literature reporting such measurements. Nevertheless, the excellent agreement between the measured and modeled signals reported in Fig. 4.9 allow us to be confident in the proposed formalism.

Despite these promising results, several simplifications were adopted at different stages of the proposed methods: First, the dispersive loss was modeled here by introducing a fractional derivative into the wave equation. Although such a phenomenological approach allowed modeling the observed frequency-dependent phase velocity and power-law attenuation in a suitable way, it prevents a proper identification of the underlying loss mechanisms. To this end, other routes could have been explored, such as the combination of hard and soft modeling [40], the incorporation of a continuum of relaxation mechanisms [41], or the formulation of a constitutive equation within the strain-gradient framework [42]. Second, it should be noted that we only solved the forward problem for the heterogeneous samples by modeling the wave-interphase interactions based on the knowledge of the mechanical properties of the individual constituents. A challenging but necessary step towards the evaluation of such composites would be to solve the inverse problem [43], i.e., reconstructing the shape of the graded profile or identifying the damage location from the measured signals. Third, both sets of samples were characterized in normal incidence, thus delivering mechanical characteristics that are related to compression waves only. However, it is expected that shear waves may carry valuable information as well both for (i) recovering the engineering moduli (e.g., Young's modulus and Poisson's

ratio) of the homogeneous samples under the assumption of mechanical isotropy, and (ii) studying the impact of damage mechanisms across the interphase on the reflected signals. A last concern is related to the replicated bioinspired feature, which was limited to a functional grading of properties along the z-direction. The latter is not the only feature that contribute to the mechanical effectiveness of the tendon-to-bone attachment. Indeed, the interdigitation at the interphase between tendon and bone, described as a wavelike structure, was shown to allow a gain in toughness, as well as a better distribution of the mechanical stresses on the fraction of tissue implied in this mechanism [44].

Altogether, these limitations make the ultrasound characterization of bioinspired functionally graded soft-to-hard composites a challenging problem with much potential for future works. As a next step, we will adapt our experimental setup to the double through-transmission method in oblique incidence [45], which allows for measurement of the phase velocity and attenuation of both longitudinal and shear waves. Future studies are also warranted to incorporate more complex mechanisms (e.g., porosity, anisotropy, and interphase roughness) in the 3D-printing and modeling processes. Overall, this research will not only be valuable for manufacturing and characterizing graded soft-to-hard composites inspired by the tendon-to-bone attachment, but also multi-material lattices and brick-and-mortar arrangements [46], which can be found for instance at the bone-implant interphase [47] or the dentine-enamel connection in teeth [48]. Given that 3D printing is experiencing a wide dissemination, our approach should be considered as a rapid, accurate and inexpensive quality inspection technique.

Acknowledgments

The authors are in debt to Max Gattin for the fruitful discussions regarding the processing of the ultrasound signals and the Szabo wave equation. This work was partially supported by the BEST-AMUS project (IIN program, CNRS-INSIS, France).

Bibliography

[1] JWC Dunlop, R Weinkamer, and P Fratzl (**2011**). "Artful interfaces within biological materials," Mater Today **14**(3), 70–78.

[2] A Velasco-Hogan, J Xu, and MA Meyers (**2018**). "Additive manufacturing as a method to design and optimize bioinspired structures," Adv Mater **30**(52), 1800940.

[3] M Rafiee, RD Farahani, and D Therriault (**2020**). "Multi-material 3D and 4D printing: A survey," Adv Sci **7**(12), 1902307.

[4] AR Studart (**2016**). "Additive manufacturing of biologically-inspired materials," Chem. Soc Rev **45**(2), 359–376.

[5] Z Jia, Y Yu, S Hou, and L Wang (**2019**). "Biomimetic architected materials with improved dynamic performance," J Mech Phys Solids **125**, 178–197.

[6] F Libonati, GX Gu, Z Qin, L Vergani, and MJ Buehler (**2016**). "Bone-inspired materials by design: toughness amplification observed using 3D printing and testing," Adv Eng Mater **18**(8), 1354–1363.

[7] L Zorzetto, and D Ruffoni (**2019**). "Wood-inspired 3D-printed helical composites with tunable and enhanced mechanical performance," Adv Funct Mater **29**(1), 1805888.

[8] Z Liu, MA Meyers, Z Zhang, and RO Ritchie (**2017**). "Functional gradients and heterogeneities in biological materials: Design principles, functions, and bioinspired applications," Prog Mater Sci **88**, 467–498.

[9] M Mirzaali, AH de la Nava, D Gunashekar, M Nouri-Goushki, R Veeger, Q Grossman, L Angeloni, M Ghatkesar, L Fratila-Apachitei, D Ruffoni *et al.* (**2020**). "Mechanics of bioinspired functionally graded soft-hard composites made by multi-material 3D printing," Compos Struct **237**, 111867.

[10] SKM, Perikamana, J Lee, T Ahmad, EM Kim, H Byun, S Lee, and H Shin (**2018**). "Harnessing biochemical and structural cues for tenogenic differentiation of adipose derived stem cells (ADSCs) and development of an in vitro tissue interface mimicking tendon-bone insertion graft," Biomaterials **165**, 79–93.

[11] V Slesarenko, and S Rudykh (**2018**). "Towards mechanical characterization of soft digital materials for multimaterial 3D-printing," Int J Eng Sci **123**, 62–72.

[12] NA Meisel, DA Dillard, and CB Williams (**2018**). "Impact of material concentration and distribution on composite parts manufactured via multi-material jetting," Rapid Prototyp J **24**(5), 872–879.

[13] L Zorzetto, L Andena, F Briatico-Vangosa, L De Noni, J-M Thomassin, C Jérôme, Q Grossman, A Mertens, R Weinkamer, M Rink *et al.* (**2020**). "Properties and role of interfaces in multimaterial 3D printed composites," Sci Rep **10**(1), 1–17.

[14] F Honarvar, and A Varvani-Farahani (**2020**). "A review of ultrasonic testing applications in additive manufacturing: Defect evaluation, material characterization, and process control," Ultrasonics 106227.

[15] Bakaric, M., Miloro, P., Javaherian, A., Cox, B. T., Treeby, B. E., and Brown, M. D. (**2007**). "Measurement of the ultrasound attenuation and dispersion in 3D-printed photopolymer materials from 1 to 3.5 MHz," J. Acoust. Soc. Am. **150**(4), 2798–2805.

[16] D Foster, M Dapino, and S Babu (**2013**). "Elastic constants of ultrasonic additive manufactured al 3003-h18," Ultrasonics **53**(1), 211–218.

[17] H Javidrad, and S Salemi (**2020**). "Determination of elastic constants of additive manufactured inconel 625 specimens using an ultrasonic technique," Int J Adv Manuf Technol **107**(11), 4597–4607.

[18] WM Rubio, GH Paulino, and ECN Silva (**2012**). "Analysis, manufacture and characterization of ni/cu functionally graded structures," Mater Des **41**, 255–265.

[19] JA Slotwinski, EJ Garboczi, and KM Hebenstreit (**2014**). "Porosity measurements and analysis for metal additive manufacturing process control," J Res Nat Inst Stand Technol **119**, 494.

[20] J Giannatsis, and V Dedoussis (**2009**). "Additive fabrication technologies applied to medicine and health care: a review," Int J Adv Manuf Syst **40**(1-2), 116–127.

[21] R Livings, V Dayal, and F Barnard (**2015**). "Characterization of 3D rapid prototyped polymeric material by ultrasonic methods," in *AIP Conf Proc*, American Institute of Physics, Vol. 1650, pp. 807–816.

[22] J-R Jacquet, F Levassort, F Ossant, and J-M Grégoire (**2015**). "3D printed phantom for high frequency ultrasound imaging," in *IEEE Int Ultrason Symp*, IEEE, pp. 1–4.

[23] MD Fariñas, T Álvarez-Arenas, G Cummins, MPY Desmulliez, V Seetohul, and S Cochran (**2016**). "Assessment of the ultrasonic properties of additive manufactured materials for passive components of piezoelectric transducers," in *IEEE Int Ultrason Symp*, IEEE, pp. 1–4.

[24] A Tits, and D Ruffoni (**2020**). "Joining soft tissues to bone: insights from modeling and simulations," Bone Rep 100742.

[25] A Aghaei, N Bochud, G Rosi, and S Naili (**2021**). "Assessing the effective elastic properties of the tendon-to-bone insertion: a multiscale modeling approach," Biomech Model Mechanobiol **20**(2), 433–448.

[26] Y Liu, S Thomopoulos, C Chen, V Birman, MJ Buehler, and GM Genin (**2014**). "Modelling the mechanics of partially mineralized collagen fibrils, fibres and tissue," J R Soc Interface **11**(92), 20130835.

[27] AC Deymier, AG Schwartz, Z Cai, TL Daulton, JD Pasteris, GM Genin, and S Thomopoulos (**2019**). "The multiscale structural and mechanical effects of mouse supraspinatus muscle unloading on the mature enthesis," Acta Biomater **83**, 302–313.

[28] M Benjamin, H Toumi, D Suzuki, S Redman, P Emery, and D McGonagle (**2007**). "Microdamage and altered vascularity at the enthesis–bone interface provides an anatomic explanation for bone involvement in the Hla–B27–associated spondylarthritides and allied disorders," Arthritis Rheum **56**(1), 224–233.

[29] F Saadat, A Deymier, V Birman, S Thomopoulos, and G Genin (**2016**). "The concentration of stress at the rotator cuff tendon-to-bone attachment site is conserved across species," J Mech Behav Biomed Mater. **62**, 24–32.

[30] A Leleux, P Micheau, and M Castaings (**2013**). "Long range detection of defects in composite plates using lamb waves generated and detected by ultrasonic phased array probes," J Nondestruct Eval **32**(2), 200–214.

[31] N Bochud, J Laurent, F Bruno, D Royer, and C Prada (**2018**). "Towards real-time assessment of anisotropic plate properties using elastic guided waves," J Acoust Soc Am **143**(2), 1138–1147.

[32] N Bochud, A Gomez, G Rus, and A Peinado (**2015**). "A sparse digital signal model for ultrasonic nondestructive evaluation of layered materials," Ultrasonics **62**, 160–173.

[33] R Raišutis, R Kažys, and L Mažeika (**2007**). "Application of the ultrasonic characterization methods for highly attenuating plastic materials," NDT & E Int **40**(4), 324–332.

[34] M Sasso, G Haïat, Y Yamato, S Naili, and M Matsukawa (**2007**). "Frequency dependence of ultrasonic attenuation in bovine cortical bone: an in vitro study," Ultrasound Med Biol **33**(12), 1933–1942.

[35] TL Szabo, and J Wu (**2000**). "A model for longitudinal and shear wave propagation in viscoelastic media," J Acoust Soc Am **107**(5), 2437–2446.

[36] JF Kelly, RJ McGough, and MM Meerschaert (**2008**). "Analytical time-domain Green's functions for power-law media," J Acoust Soc Am **124**(5), 2861–2872.

[37] N Cretu, and G Nita (**2004**). "Pulse propagation in finite elastic inhomogeneous media," Comput Mater Sci **31**(3-4), 329–336.

[38] P He, and J Zheng (**2001**). "Acoustic dispersion and attenuation measurement using both transmitted and reflected pulses," Ultrasonics **39**(1), 27–32.

[39] W Marczak (**1997**). "Water as a standard in the measurements of speed of sound in liquids," J Acoust Soc Am **102**(5), 2776–2779.

[40] J Martinsson, F Hägglund, and JE Carlson (**2008**). "Complete post-separation of overlapping ultrasonic signals by combining hard and soft modeling," Ultrasonics **48**(5), 427–443.

[41] SP Näsholm, and S Holm (**2011**). "Linking multiple relaxation, power-law attenuation, and fractional wave equations," J Acoust Soc Am **130**(5), 3038–3045.

[42] G Rosi, L Placidi, and N Auffray (**2018**). "On the validity range of strain-gradient elasticity: a mixed static-dynamic identification procedure," Eur J Mech A Solids **69**, 179–191.

[43] N Bochud, Q Vallet, J-G Minonzio, and P Laugier (**2017**). "Predicting bone strength with ultrasonic guided waves," Sci Rep **7**, 43628.

[44] Hu Y, V, Birman, A Deymier-Black, AG Schwartz, S Thomopoulos, and GM Genin (**2015**). "Stochastic interdigitation as a toughening mechanism at the interface between tendon and bone," Biophys J **108**(2), 431–437.

[45] Rokhlin SI, and Wang W (**1992**). "Double through-transmission bulk wave method for ultrasonic phase velocity measurement and determination of elastic constants of composite materials," J Acoust Soc Am **91**(6), 3303–3312.

[46] MJ Mirzaali, M Cruz Saldívar, A Herranz de la Nava, D Gunashekar, M Nouri-Goushki, EL Doubrovski, and AA Zadpoor (**2020**). "Multi-material 3D printing of functionally graded hierarchical soft–hard composites," Adv Eng Mater **22**(7), 1901142.

[47] Y Hériveaux, V-H Nguyen, and G Haïat (**2018**). "Reflection of an ultrasonic wave on the bone-implant interface: A numerical study of the effect of the multiscale roughness," J Acoust Soc Am **144**(1), 488–499.

[48] MG Messineo, GL Frontini, GE Eliçabe, and L Gaete-Garretón (**2013**). "Equivalent ultrasonic impedance in multilayer media. a parameter estimation problem," Inverse Probl Sci Eng **21**(8), 1268–1287.

Conclusion

In this dissertation, a multidisciplinary work has been carried out to better understand the mechanics of the enthesis and investigate the interaction of ultrasound waves with such functionally graded soft-to-hard interphase. A first chapter provided an overview on the structure-function relationships of the tendon-to-bone attachement, as well as on the mechanisms related to the injuries and healing phases at this transition tissue. Based on these considerations, this chapter also reviewed the different modeling strategies applied at different length scales, along with the current interface tissue engineering approaches that aim at replicating this complex interphase. In a second chapter, a multiscale model has been developed to describe how the tendon-to-bone insertion derives its overall mechanical behavior at the tissue scale. In this way, the effective anisotropic stiffness tensor of the interphase was predicted by modeling its elastic response at different scales spanning from the nanostructural to the mesostructural levels, using continuum micromechanics methods. The obtained results showed that the tendon-to-bone attachment can be considered as a continuous functionally graded medium at the tissue-scale, and the proposed model consistently predicted features observed experimentally, such as the anisotropic constitutive behavior, stiffening mechanisms, and the presence of a compliant region. In a second chapter, we proposed a modeling strategy to bridge the gap between the tissue scale and the organ scale. This was achieved by substituting the heterogeneous interphase by a an equivalent model with specific interface conditions, which retains information of the microstructural features of the orginal medium. The obtained results showed that our enriched model provided an accurate approximation of the reference interphase, thus opening promising perspectives for developing more sophisticated dynamic models targeting characterization or reattachment procedures at the organ scale. In a final chapter, the effective properties delivered by our multiscale model were used as a source of inspiration for designing and fabricating multi-material functionally graded soft-to-hard samples using additive manufacturing. The characterization of these samples was carried out using ultrasound measurements and mechanical modeling of the wave-interphase interactions. The results showed that the proposed approach may be valuable to discriminate bioinspired interphases with different profiles, as well as to retrieve their mechanical properties, altogether opening new ways for characterizing and optimizing multi-material systems that display complex bioinspired features.

The work achieved during this thesis paves the way for further applications and extensions. This field of research is indeed essential both for clinical purposes and for the

development of biomimetic strategies in engineering. Based on the results obtained during this thesis, some envisaged perspectives are listed below:

- **Multiscale modeling**: We aim to refine the multiscale model by taking into account several features that have been neglected or simplified so far, such as the viscoelastic nature of the interphase (relaxation phenomenon due to the stretching and sliding of collagen fibrils within the extracellular matrix) [1, 2], the protein gradient [3], the different types of collagen across the interphase [4] or even the interpenetration of fibers into bone, *i.e.*, the so-called interdigitation mechanism [5, 6], which all are believed to improve the fundamental anchoring mechanisms at the tendon-to-bone interphase.

- **Equivalent interface model**: To further improve the link between the meso- and macroscopic scales from a modeling viewpoint and to satisfactorily capture the rich dynamic behavior of such complex interphase at the organ level, our actual equivalent interface model should be extented to 2D. This will allow considering more realistic interphase geometries [7], as well as studying the wave-tissue interactions using both compression and shear waves.

- **Ultrasound characterization of bioinspired samples**: The methodology developed so far for characterizing the macroscopically homogeneous 3D-printed samples was limited to the study of longitudinal plane waves. The extension of the experimental setup to a double-transmission under oblique incidence is expected to deliver a full characterization of the samples [8, 9], *i.e.*, phase velocity and attenuation of both compression and shear waves, thus allowing the estimation of the engineering moduli as a function of varying volume fractions. Such procedure will in turn allow the design and fabrication of more complex heterogeneous samples by incorporating damage characteristics, porosity or anisotropic features at the insertion site, which are aknowledged to be a footprint of clinical burden, such as inflammation, fibers misalignment or detachment.

Bibliography

[1] S Kuznetsov, M Pankow, K Peters, and H-YS Huang. Strain state dependent anisotropic viscoelasticity of tendon-to-bone insertion. *Math Biosci*, 308:1–7, 2019.

[2] R Oftadeh, BK Connizzo, H Tavakoli Nia, C Ortiz, and AJ Grodzinsky. Biological connective tissues exhibit viscoelastic and poroelastic behavior at different frequency regimes: application to tendon and skin biophysics. *Acta Biomater*, 70:249–259, 2018.

[3] AD Waggett, JR Ralphs, APL Kwan, D Woodnutt, and M Benjamin. Characterization of collagens and proteoglycans at the insertion of the human Achilles tendon. *Matrix Biol*, 16(8):457–470, 1998.

[4] S Thomopoulos, GR Williams, JA Gimbel, M Favata, and LJ Soslowsky. Variation of biomechanical, structural, and compositional properties along the tendon to bone insertion site. *J Orthop Res*, 21(3):413–419, 2003.

[5] Y Hu, V Birman, A Deymier-Black, AG Schwartz, S Thomopoulos, and GM Genin. Stochastic interdigitation as a toughening mechanism at the interface between tendon and bone. *Biophys J*, 108(2):431–437, 2015.

[6] L Rossetti, LA Kuntz, E Kunold, J Schock, KW Müller, H Grabmayr, J Stolberg-Stolberg, F Pfeiffer, SA Sieber, R Burgkart, and AR Bausch. The microstructure and micromechanics of the tendon–bone insertion. *Nat Mater*, 16(6):664, 2017.

[7] J Sartori, S Köhring, S Bruns, J Moosmann, and JU Hammel. Gaining insight into the deformation of achilles tendon entheses in mice. *bioRxiv*, 2021.

[8] YC Chu and SI Rokhlin. Comparative analysis of through-transmission ultrasonic bulk wave methods for phase velocity measurements in anisotropic materials. *J Acoust Soc*, 95(6):3204–3212, 1994.

[9] SI Rokhlin and W Wang. Double through-transmission bulk wave method for ultrasonic phase velocity measurement and determination of elastic constants of composite materials. *J Acoust Soc*, 91(6):3303–3312, 1992.

Résumé

Titre: Caractérisation ultrasonore de l'interphase tissu mou-os : modélisation, étude numérique et validation expérimentale.

La liaison entre les tissus mous et les tissus durs est essentielle afin d'assurer une bonne mobilité au système musculo-squelettique. En particulier, la liaison entre le tendon et l'os a lieu par le biais d'une interphase tissulaire appelée *enthèse*. Cette interphase a pour rôle de connecter ces deux tissus présentant des propriétés mécaniques fortement dissimilaires sur une très petite région, et ce grâce à des caractéristiques spécifiques de structure, de composition et de propriétés biomécaniques à différentes échelles. Cependant, suite à une blessure en raison d'une surcharge physique, de maladies systémiques ou de dégénérescence tissulaire chez les personnes âgées, cette interphase ne peut pas correctement se régénérer. Le taux d'échecs des interventions chirurgicales pour réparer ces lésions musculo-squelettiques reste particulièrement élevé, notamment en raison du manque de solutions intégratives pour la réparation de cette interphase. Une meilleure compréhension des mécanismes responsables de l'efficacité mécanique de cette région interfaciale est donc essentielle tant pour des objectifs cliniques que pour l'élaboration de stratégies biomimétiques en ingénierie tissulaire.

Dans ce contexte, le présent travail vise à caractériser mécaniquement les interphases biologiques, à l'image de l'enthèse tendon-os. Pour atteindre cet objectif, le chapitre 1 donne un aperçu des relations entre la structure et la composition de l'insertion tendon-os. Sur la base de ces considérations, ce chapitre fournit également un aperçu des stratégies de modélisation développées à différentes échelles. Le chapitre 2 développe un modèle d'homogénéisation par champs moyens, à partir du célèbre problème d'Eshelby d'une inclusion dans une matrice, basé sur la connaissance des caractéristiques de composition de cette interphase aux petites échelles, permettant ainsi de prédire son comportement mécanique effectif à l'échelle mésoscopique. Les résultats de ce modèle sont ensuite utilisés comme données d'entrée dans les approches développées aux chapitres 3 et 4. Ainsi, le chapitre 3 vise à combler le fossé entre l'échelle du tissu et l'échelle de l'organe à des fins de modélisation en développant un modèle équivalent d'interface avec des propriétés spécifiques qui préservent les informations sur les caractéristiques microstructurelles de l'interphase. Ceci est réalisé au moyen d'un modèle original développé dans le cadre de l'élasticité de surface, qui rend compte à la fois du comportement élastique et inertiel de l'interphase réelle. Les performances de ce modèle enrichi sont évaluées dans le cadre de la propagation des ondes élastiques. Enfin, dans le chapitre 4, le modèle multi-échelle est exploité pour reproduire certaines caractéristiques mésoscopiques adoptées par cette interphase biologique pour le développement de stratégies biomimétiques en ingénierie. Ceci est réalisé par fabrication additive d'échantillons présentant une interphase possédant des propriétés bio-inspirées. Ces échantillons sont ensuite caractérisés mécaniquement à l'aide de mesures ultrasonores et de modélisation mécanique.

En résumé, ce travail combine modélisation multi-échelle, simulations numériques et validation expérimentale pour permettre une meilleure compréhension de la mécanique des interphases biologiques et propose des stratégies de modélisation et caractérisation innovantes ouvrant la voie à des applications en ingénierie tissulaire, en particulier, pour l'orthopédie.

Mots-clés : Biomécanique, Interphase biologique, Enthèse, Modélisation multi-échelle, Ondes élastiques, Simulations numériques, Mesures ultrasonores.

Abstract

Title: Ultrasonic characterization of soft tissue-to-bone interphase: modeling, numerical study and experimental validation.

The interaction between soft and hard tissues is essential to ensure good mobility to the musculoskeletal system. In particular, the integration between tendon and bone occurs through a specific functionally graded interphase called *enthesis*. This transitional tissue serves the challenging task of connecting these two highly dissimilar tissues with a mismatch in mechanical properties of nearly two orders of magnitude over a submillimeter wide region, by means of finely tuned gradients in structure, composition, and biomechanical properties at different length scales. Nevertheless, this interphase is a frequent site of injuries because of physical overloading, systemic diseases, or tissue degeneration in the elderly. The failure rate of surgical procedures for the repair of musculoskeletal injuries involving multiple tissues remains particularly high, especially because of the lack of integrative solutions for restoring such kind of interphases. In this regard, understanding the mechanisms behind the mechanical effectiveness of interfacial regions is essential for many different purposes including diagnosis, repair, and regeneration, as well as to develop biomimetic strategies in tissue engineering.

Within this context, the present thesis aims at mechanically characterizing biological multi-tissue interphases, like the tendon-to-bone insertion. To tackle this objective, chapter 1 provides an overview on the relationships between the structure and the composition of the transitional tissues at the tendon-to-bone attachment. Based on these considerations, this chapter also gives an overview of the modeling strategies that have been developed at different length scales. Chapter 2 develops a mean-field homogenization model relying on Eshelby's solution of a single-inclusion problem that, based on the knowledge of the compositional features of the tendon-to-bone interphase at lower length scales, allows predicting its overall mechanical behavior at the mesoscopic scale. The results from this model are then further used as an input to address the two subsequent approaches developed in chapters 3 and 4. Thereby, chapter 3 aims at bridging the gap between the tissue-scale and the organ scale for modeling purposes, by developing an equivalent interface model with specific properties, which retains information of the microstructural features of the interphase. This is achieved by means of an original model developed in the framework of surface elasticity, which accounts for both the elastic and inertial behavior of the real interphase. The performance of this enriched model is evaluated in the context of elastic wave propagation. Lastly, in chapter 4, the multiscale modeling is exploited for replicating some mesoscopic features adopted by this biological interphase towards the development of biomimetic strategies in engineering. This is achieved by fabricating additively manufactured samples that possess an interphase with bioinspired properties. These samples are then mechanically characterized using ultrasound measurements and mechanical modeling.

Overall, this multidisciplinary work, which combines multiscale modeling, numerical simulations, and experimental validation, allows for a better understanding of the mechanics of biological soft-to-hard interphases and proposes innovative modeling and characterization strategies towards tissue engineering applications, in particular for orthopedics.

Keywords: Biomechanics, Biological interphase, Enthesis, Multiscale modeling, Elastic waves, Numerical simulations, Ultrasound measurements.